博士論文

題目

(和文) 半導体装置製造用の電子サイクロトロン共鳴を用いたエッチング処理室におけるマイクロ波伝搬と均一プラズマ生成に関する研究

(英文) Study on microwave propagation and uniform plasma generation in an electron cyclotron etching reactor for semiconductor manufacturing

東京農工大学大学院工学府 博士後期課程

機械システム工学 専攻 平成 29 年度入学

学籍番号 17833702

氏名 田村 仁

指導教員氏名 西田 浩之

Study on microwave propagation and uniform plasma generation in an electron cyclotron etching reactor for semiconductor manufacturing

Hitoshi Tamura

Dissertation submitted in partial fulfillment
of the requirements for the degree
Doctor of Philosophy in Engineering

Department of Mechanical Systems Engineering
Tokyo University of Agriculture and Technology
2021

Tokyo University of Agriculture and Technology

Abstract

Study on microwave propagation and uniform plasma generation in an electron cyclotron etching reactor for semiconductor manufacturing

Hitoshi Tamura

Chair of the Supervisory Committee:

Associate Professor Hiroyuki Nishida

Division of Advanced Mechanical Systems Engineering, Institute of Engineering,

Tokyo University of Agriculture and Technology

In the field of semiconductor manufacturing, plasma etcher utilizing electron cyclotron resonance has been developed over 30 years and used by major ULSI manufacturers since it has many advantages such as uniform plasma generation, controllability, and low wall damage. However, the mechanism of uniform plasma generation, which is essential to improve the ECR etcher, is not sufficiently understood. One of the reasons is the complexity of the microwave distribution in the ECR reactor. It is well known that the microwaves propagate in the ECR plasma, and the wavelength becomes very short near the resonance region.

In this thesis, first we performed microwave analysis in the ECR plasma by comparing the calculated results with theoretical analysis and found that Trivelpiece-Gould waves (TG wave), whose field pattern was very complicated, were observed, which showed that the simulation tool is valid and useful. Next, we developed a simulation tool for ECR plasma etcher by combining the validated microwave tool with

plasma generation analysis and plasma diffusion analysis, and confirmed the accuracy of the tool by comparing the simulation results with experimental ones.

By using the developed tool while considering plasma density distribution, we found a phenomenon that the introduced right-hand polarized microwaves (R wave) do not enter the high density region of $\omega_{pe}/\omega > 1$, where ω_{pe} is the plasma angular frequency, and ω is the angular frequency of the microwave. This phenomenon played an important role in uniform plasma generation. However, from the theoretical dispersion relation in unbounded space, an R wave, in principle, can propagate in high density plasma of $\omega_{pe}/\omega > 1$ and does not have a cutoff in the region of high static magnetic field $\omega_{ce}/\omega > 1$. To solve the seeming contradiction, theoretical analysis of the plasma waveguide with outer vacuum layer was performed, and it was found that the cause of the phenomenon, that the microwave does not enter high density plasma, is the effect of the wall boundary. Moreover, it was demonstrated that, for the first time as far as we know, the phenomenon can be understood by the mode transformation from the introduced right-hand polarized wave (R wave) to extraordinary wave (X wave) and TG wave at around the region of $\omega_{pe}/\omega = 1$.

Keywords

electron cyclotron resonance, plasma source, microwave plasma, plasma processing, mode transformation, plasma etching, semiconductor manufacturing, R wave TG wave, X wave

Acknowledgments

As the author, I would like to express my gratitude to Professor S. Shinohara for his guidance, support, and encouragement throughout this work. His advice based on extensive knowledge, long experience of research activities, and warm heart encouraged me a lot. I also thank Senior Assistant Professor D. Kuwahara of Chubu University and Associate Professor H. Nishida, who played a part in supervisor after Professor S. Shinohara, for their support and guidance. I would also thank Professor M. Kameda, Professor T. Uno, Associate Professor K. Iwami, and Associate Professor T. Hori for their valuable comments and suggestions to improve this thesis. I would also like to thank my colleagues for their support as well. In particular, Dr. T. Tetsuka, Mr. I. Sasaki, Ms. N. Tamari, Mr. T. Sekine and Mr. A. Amend are to be acknowledged for their contributions and fruitful discussions. I also thank Dr. M. Izawa, Mr. S. Tauchi, and Mr. N. Yasui for their support and encouragement.

Finally, I wish to thank my family, who gave me much energy and motivation.

Publications

Refereed Journal Papers (Web of Science Papers):

[1] **H. Tamura**, T. Tetsuka, N. Tamari, D. Kuwahara, and S. Shinohara, "Numerical identification of Trivelpiece–Gould waves in an electron cyclotron resonance etching reactor," IEEE Trans. Plasma Sci., vol. 46, no. 10, pp. 3662–3668, Oct. 2018.

[2] **H. Tamura**, T. Tetsuka, D. Kuwahara, and S. Shinohara, "Study on uniform plasma generation mechanism of electron cyclotron resonance etching reactor," IEEE Trans. Plasma Sci., vol. 48, no. 10, pp. 3606-3615, Oct. 2020.

[3] **H. Tamura**, T. Tetsuka, T. Sekine, and S. Shinohara, "Boundary effect on mode transformation in an electron cyclotron resonance etching reactor," Jpn. J. Appl. Phys., accepted.

Journal Papers:

[1] **H. Tamura**, "Plasma simulation of electron cyclotron resonance etching reactor," Keisan-Kougaku, vol. 27, No.1, pp.16- 19, 2022.

Conference presentations:

[1] **田村仁**, 手束勉, 玉利南菜子, 桑原大介, 篠原俊二郎, "電子サイクロトロン共鳴を用いたエッチング装置中の TG 波について," 第 34 回プラズマプロセシング研究会 (SPP34), 18pA2, 2017/1/18, 札幌, 北海道大学.

[2] **H. Tamura**, T. Tetsuka, D. Kuwahara, and S. Shinohara, "ECR plasma simulation for plasma etching reactor," the 10th EU-Japan Joint Symposium on Plasma Processing (JSPP2017), 2017/12, Okinawa, Japan.

[3] **H. Tamura**, T. Tetsuka, D. Kuwahara, and S. Shinohara, "Study on uniform plasma generation in electron cyclotron resonance plasma etching reactor," (**invited**) The 7th International Conference on Microelectronics and Plasma Technology (ICMAP2018), 03_3_1003, 2018/7/24-28, Incheon, Korea.

[4] **H. Tamura**, T. Tetsuka, D. Kuwahara, and S. Shinohara, "Study on uniform plasma generation mechanism of electron cyclotron resonance etching reactor," A-I22, 2nd Asia-Pacific Conference on Plasma Physics (AAPPS-DPP2018), 2018/11/16, Kanazawa, Japan.

[5] **H. Tamura**, T. Tetsuka, D. Kuwahara, and S. Shinohara, "Simulation of ECR etching reactor using COMSOL Multiphysics®," COMSOL Conference TOKYO 2018, 2018/12/7.

[6] **H. Tamura**, T. Tetsuka, D. Kuwahara, and S. Shinohara, "Study on uniform plasma generation and microwave propagation in electron cyclotron resonance etching reactor," The 12th Asian-European International Conference on Plasma Surface Engineering (AEPSE 2019), S2-OR02, 2019/9/3, Jeju, Korea.

[7] 田村仁, 手束勉, 桑原大介, 篠原俊二郎, "ECR プラズマエッチング装置における均一プラズマ生成とマイクロ波伝搬モードの検討", プラズマ・核融合学会 第36回年会, 講演番号 29Ca04, 2019 年 11 月

[8] **H. Tamura**, T. Tetsuka, and S. Shinohara, "Study on microwave propagation and uniform plasma generation in an ECR plasma etching reactor," (**invited**) 4th Asia Pacific Conference on Plasma Physics (AAPPS-DPP2020), A-I23, 2020/10/29, online.

[9] **H. Tamura**, T. Tetsuka, and S. Shinohara, "Effect of reactor wall on microwave electromagnetic field in electron cyclotron resonance etching reactor," 12th EU-Japan

Joint Symposium on Plasma Processing (JSPP-12) and the 15th Asia-Pacific Conference on Plasma science and Technology (APCPST-15), '21/4/2.

[10] **H. Tamura**, T. Tetsuka, T. Sekine, and S. Shinohara, "Mode transformation and absorption of microwaves in and electron cyclotron etching reactor," 42nd International Symposium on Dry Process (DPS2021), D-4, '21/11/18.

Reference Papers:

[1] **H. Tamura** and S. Kurazono, "Analysis of groove guide for short-millimeter waves," Electronics and Communications in Japan (Part II: Electronics), vol. 71, no. 12, pp. 63-73, 1988.

Co-authored papers:

[1] M. Furuse, **H. Tamura**, S. Watanabe, and O. Fukumasa, "Measurement of a three-dimensional distribution of microwave electric field in electron cyclotron resonance plasmas," Jpn. J. Appl. Phys., vol. 36, Number 7S, pp. 4617- 4619, 1997.

[2] S. Watanabe, **H. Tamura**, M. Sumiya, M. Furuse, and S. Kawaski, "Slant slot antenna-type electron cyclotron resonance plasma source," Jpn. J. Appl. Phys., vol. 37, Number 9R, pp. 5021-5027 , 1998.

[3] M. Furuse, S. Watanabe, **H. Tamura**, and O. Fukumasa, "Production of highly uniform electron cyclotron resonance plasmas by distribution control of the microwave electric field," J. Vac. Sci. Technol. A, Vac., Surf., Films, vol. 17, no. 6, pp. 3225–3229, Nov. 1999.

[4] S. Watanabe, M. Sumiya, **H. Tamura**, K. Yoshioka, T. Tokunaga, and T. Mizutani, "Evaluation of charge passed through gate-oxide films using a charging damage measurement electrode," Jpn. J. Appl. Phys., vol. 39, Number 2R, pp. 662- 668, 2000.

[5] S. Watanabe, **H. Tamura**, M. Sumiya, Y. Omoto, Ken Yoshioka, and T. Mizutani, "High-frequency measurements of plasma parameters in electron cyclotron resonance plasma etchers," Jpn. J. Appl. Phys., vol. 41, Number 1R, pp. 346- 351, 2002.

[6] M. Sumiya, **H. Tamura**, and S. Watanabe, "Mechanism of the reduction of electron shading charge build-up using pulsed plasma," Jpn. J. Appl. Phys., vol. 41, Number 2R, pp. 856- 859, 2002.

[7] K. Maeda, S. Obama, **H. Tamura**, G. Miya, and M. Izawa, "Study on the distribution control of etching rate and critical dimensions in microwave electron cyclotron resonance plasmas for the next generation 450 mm wafer processing," Jpn. J. Appl. Phys., vol. 51, Aug. 2012, Art. no. 08HD01.

Contents

List of Figures

Chapter 1

Chapter 2

Chapter 3

Chapter 4

List of Tables

Chapter 3

Symbols

ω	Angular frequency of microwave
ω_{pe}	Electron plasma angular frequency
ω_{ce}	Electron cyclotron angular frequency
ε_0	The permittivity of free space
μ_0	The permeability of free space
$\boldsymbol{\varepsilon}$	Permittivity tensor of cold plasma
β	Phase constant of TG wave
p_{nv}	The vth zero of the nth-order Bessel function
T	Propagation constant to the radial direction
m	Phase dependence of azimuthal direction
$k_{//}$	Wave number to parallel direction
v_{the}	Thermal velocity of the electron
$\mathbf{D}_\varepsilon$	Diffusion coefficient tensor of energy
n_ε	Energy density of electrons
D_e	Diffusion coefficient of electron
D_i	Diffusion coefficient of ion
μ_e	Electron mobility
μ_i	Ion mobility
D_a	Ambipolar diffusion coefficient
μ_a	Ambipolar mobility
$\mathbf{K}_a$	Diffusion coefficient tensor
n	Plasma density
S	Source of plasma generation

I_{is}	Ion saturation current density
P_{μ}	Microwave power
P_{Ar}	Argon pressure in the reactor
n_c	Cutoff plasma density
n_e	Electron density
k_z	Wavenumber with respect to the waveguide axis
c	The speed of light
$k_{\perp}$	Wavenumber with respect to perpendicular direction
i	The imaginary unit
$\boldsymbol{\kappa}$	Relative dielectric tensor
B_{0r}	The r component of the static magnetic field
B_{0z}	The z component of the static magnetic field
ν_m	Collision frequency of the electron and neutral gas molecule
B_r	The r component of magnetic flux density
B_{φ}	The φ component of magnetic flux density
B_z	The z component of magnetic flux density
E_r	The r component of electric field
E_{φ}	The φ component of electric field
E_z	The z component of electric field
k_R	Wavenumber of R wave
k_L	Wavenumber of L wave
k_X	Wavenumber of X wave
k_O	Wavenumber of O wave
k_0	Wavenumber of free space

$E_{//}$	Electric field component parallel to the static magnetic field
$H_{//}$	Magnetic field component parallel to the static magnetic field
E_R	Right-hand polarized electric field component to the static magnetic field
H_R	Right-hand polarized magnetic field component to the static magnetic field
E_L	Left-hand polarized electric field component to the static magnetic field
H_L	Left-hand polarized magnetic field component to the static magnetic field

Chapter 1

1. Introduction and background

1.1 Introduction

The performance of semiconductor devices typified by logic ICs and memory ICs has been improved remarkably over the last few decades. One of the reasons for the improvement is that miniaturization of circuits has helped to achieve improved performance and lower manufacturing costs at the same time. For further improvement in productivity, wafer diameter was increased, and large wafers whose diameter are 300 mm is mainly used now for major ULSI manufacturing. In such a semiconductor manufacturing process, plasma etching is one of the important steps. For this, an electron cyclotron resonance plasma source [1] is often used by the plasma etching apparatus [2] because of the following advantages.

(1) Plasma generation stability

An ECR plasma source can stably generate plasma even in extreme conditions such as low pressure < 0.1Pa, which is advantageous for micro-fabrication since ions rarely collide with neutral gas molecules and follow a straight path-of-flight.

(2) Plasma controllability

Plasma generation region and plasma diffusion can be easily controlled by static magnetic field distribution using multiple electro-magnets.

(3) Low wall damage

Damage of the inner wall of the reactor by the plasma can be minimized because plasma generation region can be located at some distance away from the reactor wall.

(4) Uniform plasma generation

Uniform plasma generation can be achieved because of microwave propagation characteristics as described elsewhere [3] and later in Chapters 3 and 4.

However, analysis of the plasma generated by the ECR plasma source for describing wave characteristics and plasma generation/transport, leading to full, quantitative understanding to control plasma behaviors is still challenging, and many unknown factors still remained. One of the reasons are the complexities in microwave analysis. The electromagnetic field using microwaves is difficult to measure and analyze, especially in bulk plasma because the wavelength is short and comparable to the reactor dimensions. In addition, the electromagnetic field is affected by the microwave sensor, which is constructed using conductive materials.

On the other hand, numerical analysis is useful to interpret a physical phenomenon that is difficult to measure, and finite element method (FEM) is often used to simulate physical models. However, when ordinary FEM is used to solve the Helmholtz equation that is the basic expression of the microwave analysis, spurious solutions might be derived as well [4]. Moreover, the electromagnetic field in the reactor is complicated because the microwaves can propagate in the ECR plasma, and many phenomena such as resonances and cutoffs occur in magnetized plasma [1, 5].

As for the microwave analysis by FEM, a method of preventing contamination of the spurious solutions by improving the discretization of the elements was developed [6], and a computer-aided engineering (CAE) tool using the improved method was commercially available since 1989 [7]. However, the tool was specialized to electromagnetic field analysis only, and could not be applied to magnetized plasma analysis because it did not correspond to the dielectric tensor.

To calculate electromagnetic fields numerically, the finite difference time domain (FDTD) method [8] is also often used. This method directly handles the Maxwell equations by finite difference method in space by using a staggered mesh and developing them temporally. The staggered mesh is also called Yee's mesh, which defines the electric and magnetic field on different nodes. This method is easy to understand, and electric and magnetic fields can be solved simultaneously because it is based on the Maxwell equations themselves. In the early works concerning ECR plasma sources for semiconductor manufacturing that include microwave calculations [11, 12, 13, 20], this FDTD method was used because the method of preventing the spurious problem in FEM had not been recognized at that time.

As for simulating the plasma source for semiconductor manufacturing, various inductively coupled plasma (ICP) simulations, which do not include the static magnetic field, have been reported [9, 10]. On the other hand, as for the ECR plasma source, reports are limited [11-13]. The reason is not clear, but it may be due to the difficulty and complexity of microwave analysis in the presence of a static magnetic field, as mentioned before.

In the 1990s, the ECR plasma source was studied by many researchers. The basic concept of the ECR plasma source is as follows [14]: Microwaves are introduced to the ECR reactor as right-hand polarized waves (R wave) through a microwave introducing window located at the position of the stronger magnetic field, that is stronger than the field satisfying the ECR. This is the so-called the magnetic beach concept [1], which is explained later in section 1.3. The microwave power can be delivered to the ECR surface, where the microwave power is absorbed by a resonance phenomenon. It can pass through the high-density plasma because the R wave can propagate in high-density plasma of

$\omega_{pe}/\omega > 1$ when the static magnetic field sufficiently strong that $\omega_{ce}/\omega > 1$, where ω_{pe} is the plasma angular frequency, ω is the angular frequency of the microwave, and ω_{ce} is the electron cyclotron angular frequency. It is because of the propagation characteristics of the R wave, that a high-density plasma of $\omega_{pe}/\omega > 1$ can be generated easily. While most of the research works including microwave analysis were based on this basic concept of propagation characteristics in free space to accept the R wave even in a high-density region, the works considering the wall or boundary effect were limited so far.

In early works regarding the ECR plasma source, a small reactor was frequently used whose electromagnetic field in the plasma was relatively simple. Carl *et al.* investigated the transition from the low-density mode to the high-density mode in an ECR plasma source that is relatively small with a diameter of 7.9 cm [15]. They measured the plasma density and electric field by a Langmuir probe and an *E* field probe. By doing this, they found a standing wave throughout the ECR chamber in the low mode and no standing wave past the ECR zone in the high mode. They explained the mode transition qualitatively by considering R wave and left-hand polarized wave (L wave).

Popov also studied ECR plasma source with small ECR chamber diameter [16]. He used graphite cylinders as ECR chambers whose diameters are 2.5 cm, 5 cm (below cutoff), and 7.6 cm (above cutoff). He found that the microwave could propagate in the ECR chamber that was smaller than cutoff diameter as a circular waveguide when $\omega_{pe}/\omega > 1$ and $\omega_{ce}/\omega > 1$. Furthermore, he found two electron temperatures and the microwave absorption through the Landau damping [1] by measuring *I–V* characteristics of the ECR plasma. He also indicated that mode transformation from R wave to L wave and vice versa was theoretically predicted when the angle between the wave propagation and the static magnetic field is nonzero and small.

Ueda *et al*. investigated microwave propagation in an ECR reactor by considering plasma with outer vacuum region whose diameter (29 cm) is large compared with the earlier works [17, 18]. They found that the vacuum region behaved as a waveguide and that a mode transformation into an extraordinary wave (X wave) or electrostatic wave occurred in the peripheral vacuum region. They indicated that upper hybrid resonance by the X wave played an important role in uniform plasma generation.

Furuse *et al*. measured the microwave electric field distribution in the ECR etching reactor for the processing of 200 mm diameter wafers, which is a rather large reactor compared with the earlier works, in which complicated electromagnetic fields are expected, by using a probe made of dielectric material to prevent perturbation [19]. They found that a microwave electric field was detected only in the region with a high magnetic field of $\omega_{ce}/\omega > 1$ when high microwave power was injected. On the other hand, they found that a microwave electric field was detected in all regions including $\omega_{ce}/\omega < 1$ when a low microwave power was injected.

Kinder and Kushner [12] studied the plasma properties in an ECR plasma source by using a simulation technique. They assumed the introduction of the TE_{0n} mode of a circular waveguide that had only an azimuthal electric field component into the plasma chamber and analyzed the microwave electromagnetic field approximately, by using the E_θ, B_r, and B_z components only, where E_θ is the azimuthal electric field component and B_r and B_z are the radial and axial magnetic field components, respectively.

Muta *et al*. calculated the microwave distribution considering the plasma distribution [20]. They studied microwave propagation in the ECR reactor and found that R wave and L wave were observed in the ECR reactor. They also stated briefly that the

electromagnetic waves, propagating in the peripheral low-density region, were converted into X waves or electrostatic waves.

Kaneko *et al*. investigated microwave with right- and left-hand polarizations in circular waveguides filled with magnetized plasma [21]. They also performed microwave measurements in a rather large chamber whose diameter is 20.8 cm and length is about 450 cm. It is well known that an L wave is not absorbed by the ECR process because of the propagation characteristics in free space without boundaries. However, they observed that the L wave was absorbed near the ECR region because of polarization reversal. They theoretically explained the phenomenon by considering the wall of the circular waveguide.

The microwave propagation is also affected by the plasma density distribution in the ECR reactor. Maeda *et al*. reported the development of an ECR etching reactor for 450 mm diameter wafers [22]. They measured the plasma distribution in the ECR reactor by a movable single probe and found a high-density plasma column along the static magnetic field on the wafer electrode with an outer low-density region. They estimated the plasma generation distribution by combining diffusion analysis and the measured plasma density distribution. As a result, they found a ring-shaped plasma generation region on the side surface of the plasma column, where the plasma density was very uniform along radial direction in the plasma column. The result of the plasma distribution in the reactor is qualitatively consistent with the results obtained by the simulation described later in Chapter 3.

As mentioned above, the microwave electromagnetic field in the ECR reactor becomes apparent to some extent through calculation and experiment, and it was shown experimentally that uniform plasma can be generated in the ECR reactor. However, the relationship between the generation of uniform plasma and the microwave characteristics

has not been clear since microwave analysis in the ECR reactor is insufficient. Therefore, we construct a simulation tool for the ECR reactor that analyzes the microwave distribution and the plasma generation simultaneously to identify the mechanism of uniform plasma generation by using the results of the simulation tool.

The contents of this thesis are as follows. In this chapter, background information concerning microwave analysis in magneto plasma is briefly described in Section 1.2, and representative plasma processing tools for semiconductor manufacturing are presented in Section 1.3.

In Chapter 2, microwave analysis in an ECR etching reactor is investigated as the first step in the ECR plasma simulation [23]. The results of the microwave electric field distribution showed highly complex patterns with fine structures, and we initially suspected that these patterns were spurious. Thus, the patterns were investigated in detail to determine whether they were spurious, and we found that they actually originated from Trivelpiece-Gould (TG) waves [24] based on their emergence conditions, dispersion relations, and characteristic wave patterns. Therefore, it was confirmed that the very complex patterns in the ECR reactor were not spurious, and it was also demonstrated that the developed code can calculate even very fine structures of the electromagnetic fields.

In Chapter 3, a simulation of the ECR reactor is performed. We developed a simulation tool for ECR etchers by using the verified microwave analysis, which is described in Chapter 2, combined with plasma generation analysis and plasma diffusion analysis. The simulated results were compared with the measured plasma density distribution, and it was confirmed that the simulation tool was valid quantitatively. Moreover, theoretical analysis of a waveguide filled with magneto-plasma [25] was performed, and wave propagation characteristics in the waveguide were discussed. As a

result of the simulation, a phenomenon was found, that the introduced R wave does not enter the high-density plasma of $\omega_{pe}/\omega > 1$ in strong magnetic field regions of $\omega_{ce}/\omega > 1$, and that a very uniform plasma, whose density almost corresponds to $\omega_{pe}/\omega = 1$, was generated. However, this phenomenon of R wave propagation in the reactor contradicts the propagation characteristics of an ordinary R wave, which can propagate in high density plasma of $\omega_{pe}/\omega > 1$ in strong magnetic field regions with $\omega_{ce}/\omega > 1$.

In Chapter 4, wave propagation characteristics in the ECR reactor were discussed in detail by using the electromagnetic field obtained by the verified simulation described in Chapter 3 to solve the contradiction of R wave propagation. We found X waves, TG waves, and surface waves in the ECR reactor in addition to introduced R waves. Moreover, theoretical analysis of plasma waveguide with outer vacuum layer, which simulates plasma distribution in the ECR reactor, was performed, and wave propagation characteristics considering wall boundary effect were derived. As a result, it was found that wave transformation from R wave to X wave and TG wave occurred in the reactor. Finally, comparing the theoretical result with the electromagnetic field distribution in the ECR reactor, the wave transformations were discussed. Concluding remarks and plans for future works were presented in Chapter 5.

1.2 Background

The microwave propagation in ECR reactors has been often discussed based on theoretical analysis results of electromagnetic wave propagation in free space without boundaries. They are often explained by using the Clemmow-Mullaly-Allis (CMA) diagram shown in Fig.1.1 [1, 5, 25]. It describes propagation region, resonances and cutoffs of the fundamental R, L, X waves, and ordinary waves (O waves) in a graph whose

horizontal and vertical axes are ω_{pe}^2/ω^2 or plasma density and ω_{ce}/ω or static magnetic field, respectively. Note that an ordinary CMA diagram considers the effect of ions such as ion cyclotron resonance and lower hybrid resonance. Note that $\omega_{pe}{}^2 = n_e e^2/m_e\,/\varepsilon_0$ and ω_{pe}^2 is proportional to plasma density, where n_e is plasma density, m_e is the electron mass, ε_0 is permittivity of vacuum, respectively, and $\omega_{ce} = eB_0/m_e$ and ω_{ce} is proportional to static magnetic flux density, where B_0 is static magnetic flux density. Moreover, the wave normal surfaces, which are the surfaces of the phase velocity versus angle to the static magnetic field, are plotted in each region of the CMA diagram. Figure 1.2 shows coordinate system used for the wave normal surface. The wave normal surface depicts phase velocities of fast and slow waves in a cylindrical coordinate system, whose static magnetic field is aligned along the z axis. By using the CMA diagram, it is found that the R wave propagates in low density plasma and even in high density plasma of $\omega_{pe}^2/\omega^2 > 1$ when the static magnetic field is strong, such that $\omega_{ce}/\omega > 1$.

In many textbooks [1, 5, 25], propagation characteristics based on cold plasma analysis is described. First, the description of fundamental waves in magnetized plasma without boundaries according to the textbook [25] is summarized as follows. Electromagnetic fields can be described by the Maxwell equations,

$$\nabla \times \boldsymbol{E} = -\frac{\partial \boldsymbol{B}}{\partial t},$$

$$\nabla \times \boldsymbol{B} = \mu_0 \left(\boldsymbol{\sigma} \cdot \boldsymbol{E} + \varepsilon_0 \frac{\partial \boldsymbol{E}}{\partial t} \right), \tag{1.1}$$

where $\boldsymbol{E}$ and $\boldsymbol{B}$ are the electric field vector and magnetic flux density vector of the microwave, ε_0 and μ_0 are the permittivity and the permeability of vacuum, and $\boldsymbol{\sigma}$ is

conductivity tensor. Considering a plane wave of the microwave whose angular frequency is ω and wavenumber $\boldsymbol{k}$, to the first order, the oscillations of $\boldsymbol{E}$ and $\boldsymbol{B}$ can be expressed as,

$$\boldsymbol{E} = \boldsymbol{E_1} \exp[i(\boldsymbol{k} \cdot \boldsymbol{r} - \omega t)],$$
$$\boldsymbol{B} = \boldsymbol{B_1} \exp[i(\boldsymbol{k} \cdot \boldsymbol{r} - \omega t)], \tag{1.2}$$

where $\boldsymbol{r}$ is the position vector, and i is the imaginary unit. By using Eq. (1.2), ∇ and $\partial/\partial t$ in Eq. (1.1) can be replaced by $i\boldsymbol{k}$ and $-i\omega$, respectively. Then, by using Eqs. (1.1) and (1.2), we obtain

$$\boldsymbol{n} \times (\boldsymbol{n} \times \boldsymbol{E_1}) + \boldsymbol{K} \cdot \boldsymbol{E_1} = \boldsymbol{0}, \tag{1.3}$$

where c is the velocity of light, $\boldsymbol{n} = \boldsymbol{k}c/\omega$ is refractive index vector that lies in the x-z plane, and $\boldsymbol{K} = \boldsymbol{1} + i/\omega/\varepsilon_0 \boldsymbol{\sigma}$ is the relative dielectric tensor. The conductivity tensor $\boldsymbol{\sigma}$ can be derived by considering electron velocity vector $\boldsymbol{v}_e$ in a static magnetic field $\boldsymbol{B}_0$, which can be solved by the following equation of motion using Lorentz force

$$-i\omega m_e \boldsymbol{v}_e = -e(\boldsymbol{E_1} + \boldsymbol{v}_e \times \boldsymbol{B}_0), \tag{1.4}$$

and the conduction current

$$\boldsymbol{\sigma} \cdot \boldsymbol{E_1} = -n_e e \boldsymbol{v}_e. \tag{1.5}$$

Note that the effect of ions for electromagnetic field analysis is not considered, since we mainly discuss microwaves in this thesis, which are barely affected by ion motion. When ion oscillation by the microwave and collisions between electron and neutral gas molecules are neglected, the relative dielectric tensor $\boldsymbol{K}$, whose static magnetic field is along the z axis, can be expressed as [1]

$$\boldsymbol{K} = \begin{bmatrix} S & -iD & 0 \\ iD & S & 0 \\ 0 & 0 & P \end{bmatrix}, \tag{1.6}$$

where $S = 1 - {\omega_{\mathrm{pe}}}^2/(\omega^2 - {\omega_{\mathrm{ce}}}^2)$, $D = -\omega_{\mathrm{ce}}/\omega \cdot {\omega_{\mathrm{pe}}}^2/(\omega^2 - {\omega_{\mathrm{ce}}}^2)$, $P = 1 - {\omega_{\mathrm{pe}}}^2/\omega^2$, ω_{pe} is the plasma angular frequency, and ω_{ce} is the electron cyclotron angular frequency. Here, we treat the two components of electrons and ions with an assumption of much heavier ion mass than electron one.

By using Eq. (1.6), Eq. (1.3) is

$$\begin{bmatrix} S - n^2\cos^2\theta & -iD & n^2\sin\theta\cos\theta \\ iD & S - n^2 & 0 \\ n^2\sin\theta\cos\theta & 0 & P - n^2\sin^2\theta \end{bmatrix} \begin{bmatrix} E_x \\ E_y \\ E_z \end{bmatrix} = \mathbf{0}, \tag{1.7}$$

where, n=|$\boldsymbol{n}$| is amplitude of the refractive index vector, θ is the angle between the static magnetic field and the wavenumber vector (see Fig. 1.2), and E_x and E_y and E_z are the components of $\boldsymbol{E}_1$. The dispersion relation of the microwave can be derived by setting the determinant of the coefficient matrix of Eq. (1.7) to zero. Then, the dispersion relation of the microwave is

$$An^4 - Bn^2 + C = 0, \tag{1.8}$$

where $A = S\sin^2\theta + P\cos^2\theta$, $B = (S^2 - D^2)\sin^2\theta + (1 + \cos^2\theta)SP$, $C = (S^2 - D^2)P$.

Needless to say, when n becomes infinite, it shows resonance with zero wavelength, leading to wave absorption. On the other hand, n approaches to zero, reflection of waves with infinite wavelength can be expected.

When the microwave propagates along the static magnetic field ($\theta = 0$), Eq. (1.8) in the ω_{ce} range, we obtain

$$n^2 = S \pm D = \begin{cases} 1 - \frac{\omega_{pe}{}^2}{\omega^2}\frac{1}{1-\omega_{ce}/\omega} \\ 1 - \frac{\omega_{pe}{}^2}{\omega^2}\frac{1}{1+\omega_{ce}/\omega} \end{cases}. \tag{1.9}$$

When the microwave propagates perpendicular to the static magnetic field ($\theta = \pi/2$),

$$n^2 = \begin{cases} (S^2 - D^2)/S \\ P \end{cases} = \begin{cases} 1 - \frac{\omega_{pe}{}^2}{\omega^2}\frac{1-\omega_{pe}{}^2/\omega^2}{1-\omega_{ce}{}^2/\omega^2-\omega_{pe}{}^2/\omega^2} \\ 1 - \frac{\omega_{pe}{}^2}{\omega^2} \end{cases}. \tag{1.10}$$

Equation (1.9) represents the dispersion relation of the R wave (right-hand circular polarization) and L wave (left-hand circular polarization), respectively (see Fig. 1.2). Here, we use $\omega = \omega_{ce}$, which leads to infinite n, using the R wave in our ECR scheme. Equation (1.10) represents the X wave and O wave, respectively. Here, X and O waves have the electric field perpendicular and parallel to the external magnetic field. By using

these dispersion relations, the propagation characteristics of the fundamental waves without boundary can be discussed later in Chapter 3 and 4. Note that, for an arbitrary propagation angle, we can see the CMA diagram in Fig. 1.1, shown before.

In this thesis, we treat a 2-D axisymmetric model since the shape of the wafer used for semiconductor manufacturing is round. When the spatial variation of the static magnetic field is small, the relative permittivity tensor of a 2-D axisymmetric static magnetic field can be represented as [11]

$$\boldsymbol{\varepsilon} = \begin{bmatrix} S + (P-S)\beta^2 & -iD\gamma & (P-S)\beta\gamma \\ iD\gamma & S & -iD\beta \\ (P-S)\beta\gamma & iD\beta & S + (P-S)\gamma^2 \end{bmatrix}, \tag{1.11}$$

where $\beta = B_{0r}/\sqrt{{B_{0r}}^2 + {B_{0z}}^2}$, $\gamma = B_{0z}/\sqrt{{B_{0r}}^2 + {B_{0z}}^2}$, B_{0r} and B_{0z} are the r and z component of the static magnetic flux density, respectively. We use this permittivity tensor in Chapters 2 and 3. Equation (1.11) is an extension of Eq. (1.6) for a general direction of the static magnetic field.

It is important to consider the effect of collisions between electrons and neutral gas molecules because it relates to propagation characteristics such as wave dumping and power absorption. By using collision frequency between electrons and neutral gas molecules ν_e, parameters in Eqs (1.6) – (1.11) can be represented as [25]

$$S = 1 - \frac{{\omega_{pe}}^2(\omega + i\nu_e)}{\omega\{(\omega + i\nu_e)^2 - {\omega_{ce}}^2\}}, \tag{1.12}$$

$$D = -\frac{\omega_{ce}{\omega_{pe}}^2}{\omega\{(\omega + i\nu_e)^2 - {\omega_{ce}}^2\}}, \tag{1.13}$$

$$P = 1 - \frac{{\omega_{pe}}^2}{\omega(\omega + i\nu_e)}. \tag{1.14}$$

By using S, D, and P of Eqs. (1.12) – (1.14), wave characteristics considering the collisional effect of fundamental waves can be evaluated.

Secondly, the dispersion relation at circular waveguides filled with magneto plasma [25], considering the wall effect, is summarized as follows. Microwaves that propagate along the z axis in magneto plasma with the static magnetic field along the z axis are considered. To the first order, the oscillating parts of the electric field and magnetic flux density are

$$\boldsymbol{E} = \boldsymbol{E}(r)\exp[i(k_z z + m\theta - \omega t)],$$
$$\boldsymbol{B} = \boldsymbol{B}(r)\exp[i(k_z z + m\theta - \omega t)], \tag{1.15}$$

where k_z is the wavenumber along the z axis, and m is an azimuthal mode number. By using Eq (1.15), the Maxwell equations in a cylindrical coordinate system are

$$(\nabla \times \boldsymbol{E})_r = \frac{im}{r}E_z - ik_z E_\theta = i\omega B_r,$$
$$(\nabla \times \boldsymbol{E})_\theta = ik_z E_r - \frac{d}{dr}E_z = i\omega B_\theta,$$
$$(\nabla \times \boldsymbol{E})_z = \frac{1}{r}\frac{d}{dr}(rE_\theta) - \frac{im}{r}E_r = i\omega B_z,$$
$$(\nabla \times \boldsymbol{B})_r = \frac{im}{r}B_z - ik_z B_\theta = -\frac{i}{\omega}(\kappa_1 E_r + \kappa_2 E_\theta),$$
$$(\nabla \times \boldsymbol{B})_\theta = ik_z B_r - \frac{d}{dr}B_z = -\frac{i}{\omega}(-\kappa_2 E_r + \kappa_1 E_\theta),$$
$$(\nabla \times \boldsymbol{B})_z = \frac{1}{r}\frac{d}{dr}(rB_\theta) - \frac{im}{r}B_r = -\frac{i}{\omega}\kappa_3 E_z, \tag{1.16}$$

where $\kappa_1 = S\,\omega^2/c^2$, $\kappa_2 = -iD\,\omega^2/c^2$, $\kappa_3 = P\,\omega^2/c^2$. Perpendicular components of electromagnetic field with respect to the z axis can be derived from Eq. (1.16) as follows.

$$\boldsymbol{E}_\perp = a\nabla_\perp E_z + b\nabla_\perp B_z + c\hat{\boldsymbol{e}}_z \times \nabla_\perp E_z + d\hat{\boldsymbol{e}}_z \times \nabla_\perp B_z,$$
$$\boldsymbol{B}_\perp = p\nabla_\perp E_z + a\nabla_\perp B_z + q\hat{\boldsymbol{e}}_z \times \nabla_\perp E_z + c\hat{\boldsymbol{e}}_z \times \nabla_\perp B_z, \tag{1.17}$$

where $\boldsymbol{E}_\perp = \boldsymbol{E} - \hat{\boldsymbol{e}}_z E_z$, $\boldsymbol{B}_\perp = \boldsymbol{B} - \hat{\boldsymbol{e}}_z B_z$, $\nabla_\perp = \nabla - \hat{\boldsymbol{e}}_z \frac{\partial}{\partial z}$, $\gamma = {k_z}^2 - \kappa_1$, $a = -\frac{ik_z\gamma}{\gamma^2+{\kappa_2}^2}$, $c = \frac{ik_z\kappa_2}{\gamma^2+{\kappa_2}^2}$, $b = \frac{i\omega\kappa_2}{\gamma^2+{\kappa_2}^2}$, $d = \frac{i\omega\gamma}{\gamma^2+{\kappa_2}^2}$, $p = -\frac{i{k_z}^2\kappa_2}{\omega(\gamma^2+{\kappa_2}^2)}$, $q = -\frac{i(\kappa_1\gamma-{\kappa_2}^2)}{\omega(\gamma^2+{\kappa_2}^2)}$.

By using Eq. (1.17) to eliminate perpendicular components from Eq. (1.16),

$$(c^2 - qd){\nabla_\perp}^4 E_z + \left(i\omega q - \frac{id\kappa_3}{\omega}\right){\nabla_\perp}^2 E_z - \kappa_3 E_z = 0,$$
$$(c^2 - qd){\nabla_\perp}^4 B_z + \left(i\omega q - \frac{id\kappa_3}{\omega}\right){\nabla_\perp}^2 B_z - \kappa_3 B_z = 0. \tag{1.18}$$

Equation (1.18) can be written as

$$\left({\nabla_\perp}^2 + {k_{\perp 1}}^2\right)\left({\nabla_\perp}^2 + {k_{\perp 2}}^2\right)\begin{pmatrix} E_z \\ B_z \end{pmatrix} = 0, \tag{1.19}$$

$$(c^2 - qd){k_\perp}^4 + \left(i\omega q - \frac{id\kappa_3}{\omega}\right){k_\perp}^2 - \kappa_3 = 0, \tag{1.20}$$

where ${k_{\perp 1}}^2$ and ${k_{\perp 2}}^2$ are solutions of Eq. (1.20). By reorganizing Eq. (1.20), the dispersion relation for a cold uniform plasma can be derived as

$$\left(\gamma^2 + {\kappa_2}^2 + \gamma {k_\perp}^2\right)\kappa_3 + {k_\perp}^2\left\{\kappa_1\left(\gamma + {k_\perp}^2\right) - {\kappa_2}^2\right\} = 0. \tag{1.21}$$

Here, the perpendicular wavenumber $k_\perp$ is determined by a boundary condition. This dispersion relation will be used later in Chapters 2, 3 and 4.

Next, the Trivelpiece-Gould wave (TG wave) is summarized as follows since it plays an important role in this thesis. It was first described in [24], and the dispersion relation was derived based on electrostatic approximation. We summarize the equations that we use later as follows, according to the paper [24]. The plasma geometry is the same as in Fig. 4.2, which is a circular waveguide partially filled with magneto plasma. The inner plasma radius is *a*, and the waveguide radius is *b*. The electric field vector of the TG wave is derived by Laplace's equation

$$\boldsymbol{\nabla} \cdot (\boldsymbol{\varepsilon} \cdot \boldsymbol{E}) = 0, \tag{1.22}$$

where $\boldsymbol{\varepsilon} = \begin{bmatrix} \varepsilon_1 & i\varepsilon_2 & 0 \\ -i\varepsilon_2 & \varepsilon_1 & 0 \\ 0 & 0 & \varepsilon_3 \end{bmatrix}$ is dielectric tensor, $\varepsilon_1 = \varepsilon_0\left(1 - \frac{{\omega_{pe}}^2}{\omega^2 - {\omega_{ce}}^2}\right) = \varepsilon_0 S$, $\varepsilon_2 = \varepsilon_0 \frac{\omega_{ce}}{\omega}\left(\frac{{\omega_{pe}}^2}{\omega^2 - {\omega_{ce}}^2}\right) = -\varepsilon_0 D$, $\varepsilon_3 = \varepsilon_0\left(1 - \frac{{\omega_{pe}}^2}{\omega^2}\right) = \varepsilon_0 P$. Although these parameters are almost the same as the ones mentioned before, we continue to describe according to the paper [24].

$\boldsymbol{E}$ is represented by a scaler potential as

$$\boldsymbol{E} = -\boldsymbol{\nabla}\phi. \tag{1.23}$$

Then, Eq. (1.22) in cylindrical coordinates becomes

$$\varepsilon_1 \left\{ \frac{1}{r} \frac{\partial}{\partial r} \left(r \frac{\partial \phi}{\partial r} \right) + \frac{1}{r^2} \frac{\partial^2 \phi}{\partial \theta^2} \right\} + \varepsilon_3 \frac{\partial^2 \phi}{\partial z^2} = 0. \tag{1.24}$$

Assuming $\phi = \phi(Tr) \exp[-i(m\theta + \beta z)]$, Eq. (1.24) becomes

$$R^2 \frac{\partial^2 \phi(R)}{\partial R^2} + R \frac{\partial \phi(R)}{\partial R} + \left(-\beta^2 \frac{\varepsilon_3}{\varepsilon_1} \frac{1}{T^2} R^2 - m^2 \right) \phi(R) = 0, \tag{1.25}$$

where $R=Tr$.

Equation (1.23) is the Bessel's differential equation when

$$T^2 = -\beta^2 \frac{\varepsilon_3}{\varepsilon_1} = -\beta^2 \frac{(\omega^2 - \omega_{pe}{}^2)(\omega^2 - \omega_{ce}{}^2)}{\omega^2 (\omega^2 - \omega_{pe}{}^2 - \omega_{ce}{}^2)}. \tag{1.26}$$

The solution of Eq. (1.25) is

$$\phi = A J_m(Tr) \exp[-i(m\theta + \beta z)] \quad 0 < r < a,$$

$$\phi = B\{I_m(\beta r) K_m(\beta b) - I_m(\beta b) K_m(\beta r)\} \exp[-i(m\theta + \beta z)] \quad a < r < b, \tag{1.27}$$

where J_m is m-th order Bessel function of the 1st kind, I_m is m-th order modified Bessel function of the 1st kind, and K_m is m-th order modified Bessel function of the 2nd kind.

By using the boundary conditions on the interface of the plasma and outer vacuum layer ($r = a$) and of the waveguide wall ($r = b$), the dispersion relation can be derived as

$$\varepsilon_1 Ta \frac{J_m{}'(Ta)}{J_m(Ta)} + m\varepsilon_2 = K_e \varepsilon_0 \beta a \frac{I_m{}'(\beta a)K_m(\beta b) - I_m(\beta b)K_m{}'(\beta a)}{I_m(\beta r)K_m(\beta b) - I_m(\beta b)K_m(\beta a)}, \quad (1.28)$$

where K_e is the dielectric constant of the region outside the plasma. When the plasma completely fills the waveguide ($a = b$), the dispersion relation is

$$\beta a = \pm p_{m\nu} \sqrt{\frac{-\omega^2(\omega^2 - \omega_{pe}{}^2 - \omega_{ce}{}^2)}{(\omega^2 - \omega_{pe}{}^2)(\omega^2 - \omega_{ce}{}^2)}}, \quad (1.29)$$

where $p_{m\nu}$ is the νth zero of the m-th order Bessel function of the first kind.

Next, we summarize a discussion in Yasaka's paper [11], dealing with the wave damping by the ECR scheme in comparing the hot and cold plasma dispersion relations. So far, we have treated wave phenomena under the cold plasma approximation. However, in ECR plasma that operates in low pressure, hot plasma effects such as Doppler-shifted ECR, where $\omega = \omega_{ce} - k_{//} v_{ez}$ (v_{ez}: electron velocity along the magnetic field), might be important since they relate to the thickness of the ECR region. They discussed the similarities and differences between hot plasma and cold plasma. Power absorption of R waves can be represented based on cold plasma approximation as

$$p_{abs} = n_e \frac{e^2 E^2}{2m_e} \frac{\nu_e}{(\omega - \omega_{ce})^2 + \nu_e{}^2}, \quad (1.30)$$

where n_e is the plasma density, e is the elementary charge, E is the amplitude of the electric field of the R wave, m_e is the electron mass, ν_e is the collision frequency of the electron and neutral gas molecules. They stated that power absorption of the R wave based on hot plasma is

$$p_{abs} \cong n_e \frac{e^2E^2}{2m_e}\sqrt{\pi}\frac{k_\parallel v_{the}}{(\omega-\omega_{ce})^2+{k_\parallel}^2{v_{the}}^2}, \tag{1.31}$$

by assuming that $(\omega - \omega_{ce})/k_\parallel v_{the}$ is small, where $k_\parallel$ is the wavenumber parallel to the static magnetic field, and v_{the} is the thermal velocity of the electrons. Equation (1.31) for hot plasma is similar to Eq. (1.30) for cold plasma approximation, if $k_\parallel v_{the}$ corresponds to the collision frequency of ν_e. In this case, the absolute value agrees within a factor of $\sqrt{\pi}$. They conclude that hot plasma effects can be approximately simulated by adjusting the collision frequency in cold plasma.

A surface wave is observed in the ECR reactor as mentioned later in Chapter 4. Generally, it propagates along the interface between different media such as quartz plate and plasma, and it attenuates as the distance from the interface increases. There are some plasma sources utilizing surface waves for semiconductor manufacturing [31]. A typical example is as follows. In a microwave plasma source without static magnetic field, microwaves often turn into surface waves localized at the interface between the microwave introducing window and the plasma generated in the chamber, since the microwaves cannot propagate in high density plasma of $\omega_{pe}/\omega > 1$. The power of the microwave is absorbed at the plasma surface after changing into a surface wave, and the plasma volume increases as the microwave power increases since the plasma density is saturated at the density corresponding to $\omega_{pe}/\omega = 1$.

1.3 Plasma source for semiconductor manufacturing

Although various types of ECR plasma sources have been proposed [14], two types of ECR plasma source are practically used for semiconductor manufacturing. One

is the ECR etcher that is described in this thesis that we call typical ECR reactor as shown in Fig. 1.3. Another is called the "NTT system" as shown in Fig. 1.4, that was originally developed by the Nippon Telegram and Telephone (NTT) Corporation.

The typical ECR reactor used to manufacture semiconductors is shown in Fig. 1.3 [2]. Microwaves with a frequency f of 2.45 GHz were introduced as right-hand polarized waves (R waves) through a circular waveguide into a cavity region to trim the microwave electromagnetic distribution. Here, the microwave mode in the circular waveguide was TE_{11}. A quartz window was positioned between the cavity region and plasma chamber, which was surrounded by electromagnets to generate a static magnetic field. Each current of electromagnets could be varied independently to control the static magnetic field distribution in the plasma chamber. The positions of the ECR and plasma diffusion regions, which are important to determine plasma distribution, could be controlled by the currents of each magnet. A quartz tube was located on the inner surface of the cylindrical plasma chamber to protect from plasma contamination and maintain floating conditions. A wafer with a diameter of 300 mm was placed on a wafer electrode in the plasma chamber.

There have been many reports concerning "NTT system", shown in Fig.1.4 used for plasma process etching [26], chemical vapor deposition (CVD) [27], and sputter deposition [28]. Microwaves are introduced through the rectangular waveguide and window to the plasma generation chamber. Around the plasma generation chamber, electromagnets are set to generate an ECR region in it. Under the plasma generation chamber, a plasma processing chamber is located. This reactor is characterized by the division into two plasma chambers, one for generation and another for processing.

In the above mentioned two types of ECR plasma sources, a static magnetic field is designed based on the so-called magnetic beach concept [1] (see Fig.1.3). Without the static magnetic field, high density plasma of $\omega_{pe}/\omega > 1$ is difficult to generate since microwaves can only propagate in low density plasma of $\omega_{pe}/\omega < 1$ if there are no boundaries according to theoretical analysis. However, by utilizing static magnetic fields, high density plasma of $\omega_{pe}/\omega > 1$ can be easily generated because R waves, whose propagation direction is parallel to the static magnetic field, can propagate in high density plasma of $\omega_{pe}/\omega > 1$, when $\omega_{ce}/\omega > 1$, and the microwave power can be delivered to the ECR region of $\omega_{ce}/\omega = 1$ where the microwave power is absorbed by electron cyclotron resonance. The magnetic beach concept utilizes these propagation and absorption characteristics of R waves. To realize the magnetic beach concept, the static magnetic field is designed so that the microwave is introduced to the reactor parallel to it, where the static magnetic field is higher than $\omega_{ce}/\omega > 1$ in the vicinity of the microwave introducing window, and gradually decreases to $\omega_{ce}/\omega < 1$ along the axial direction, as shown in Fig. 1.3.

Other plasma sources such as capacitively coupled plasma (CCP) [29] and inductively coupled plasma (ICP) [30] in the radio frequency range instead of the microwave one are also used for semiconductor manufacturing. Figure 1.5 shows an example of a CCP source. A typical CCP reactor consists of two parallel electrodes, one is for grounding and the other is connected to an RF power source of 13.56 MHz through a blocking condenser. The upper electrode, which is grounding, is often made of silicon. Plasma is produced near the electrode with the Ohmic heating mostly within a skin layer of c/ω_{pe} (evanescent electric field). By using the blocking condenser, the wafer is negatively biased, so-called self-bias, and ions in the plasma are accelerated toward the

wafer. The CCP reactor can accept large diameter wafers with an electron density being much lower than that of the ECR scheme by more than two orders of magnitude. Figure 1.6 shows an example of an ICP reactor. An RF power source whose frequency is typically 13.56MHz is connected to an induction coil and generates an electromagnetic field in the reactor through a dielectric window. An induction current within a skin layer on the surface of the plasma is generated by the induction coil and the power loss by the induction current through Ohmic heating maintains the plasma to the same order of electron density as the ECR plasma. The generation region and the distribution of the plasma can be controlled easily by the position of the induction coil since the plasma is generated just under the coil. However, damage of the dielectric window by the plasma might be severe since the RF power is dissipated at the surface of the plasma. There is another type of ICP reactor whose induction coil is located at the side surface of the reactor.

Impedance matching is important to supply the power of electromagnetic waves to the plasma effectively. In a plasma source without a static magnetic field, which operates in over-dense region or surface wave mode (see Section 1.2), the large reflection coefficient of the electromagnetic waves often becomes a problem, because the electromagnetic waves cannot propagate in the plasma. However, as for the ECR plasma source, the reflection coefficient tends to be low because the microwaves propagate and are absorbed easily by the effect of static magnetic fields including through resonance. We also identified that the reflection coefficient is not so high in the simulation results of the ECR reactor, which is shown later in Fig. 4.3.

In the plasma processing tools for semiconductor manufacturing, various gases are used. For example, chlorine or hydrogen bromide for silicon etching, fluorocarbon for

silicon dioxide etching, monosilane for silicon CVD, and methane for carbon CVD are used. Moreover, other gases such as oxygen, hydrogen, nitrogen, and noble gases are often mixed to improve quality and/or productivity of the plasma processing. In this thesis, argon is used to investigate fundamental characteristics of the ECR etcher since plasma composition and analysis are simple. In the argon plasma generated by the ECR plasma etching reactor, electrons, argon ions with an electric charge of 1, and other excited species are included, and no negative ions are contained. Moreover, plasma diffusion can be treated as ambipolar diffusion [5], which is the phenomenon of electrons and ions diffusing together, since they are connected to each other by electrostatic force. We have experimentally confirmed that the fundamental characteristics of argon concerning plasma distribution are almost the same as for other gasses. Therefore, analysis using argon is enough to be used. However, as for research fields in which chemical reactions are important, it is essential that reactive gases must be considered.

References

[1] T. H. Stix, Waves in Plasmas. New York, NY, USA: Springer, 1992.

[2] H. Enami, Y. Ogawa, M. Izawa, and T. Saito, "History and future of Hitachi's plasma etching system," Hitachi Rev., vol. 60, no. 5, pp. 198- 202, Aug. 2011.

[3] **H. Tamura**, T. Tetsuka, D. Kuwahara, and S. Shinohara, "Study on uniform plasma generation mechanism of electron cyclotron resonance etching reactor," IEEE Trans. Plasma Sci., vol. 48, no. 10, pp. 3606-3615, Oct. 2020.

[4] M. Koshiba and K. Inoue, "Simple and efficient finite-element analysis of microwave and optical waveguides," IEEE Trans. Microw. Theory Techn., vol. 40, no. 2, pp. 371–377, 1992.

[5] F. F. Chen, Introduction to Plasma physics. New York, NY, USA: Plenum Press, 1974.

[6] Z. J. Cendes, “Vector finite elements for electromagnetic field computation,” IEEE Trans. Magn., vol. 27, no. 5, pp. 3958–3966, Sep. 1991.

[7] Z. J. Cendes, “EM simulators=CAE tools,” IEEE Spectr., vol. 27, no. 11, pp. 73–77, Nov. 1990.

[8] K. S. Yee, “Numerical Solution of Initial boundary value problems involving Maxwell’s equation in isotropic media,” *IEEE Trans. Antennas Propagation*, vol. 14, pp. 302-307, 1966.

[9] P. L. G. Ventzek, T. J. Sommerer, R. J. Hoekstra, and M. J. Kushner, “Two-dimensional hybrid model of inductively coupled plasma sources for etching,” Appl. Phys. Lett., vol. 63, no. 5, pp. 605- 607, 1993.

[10] L. Liu, S. Sridhar, W. Zhu, V. M. Donnelly, D. J. Economou, M. D. Logue, and M. J. Kushner, “External control of electron energy distributions in a dual tandem inductively coupled plasma,” J. Appl. Phys., vol. 118, 083303, 2015.

[11] Y. Yasaka, A. Fukuyama, A. Hatta, and R. Itatani, “Two–dimensional modeling of electron cyclotron resonance plasma production,” J. Appl. Phys., vol. 72, no. 7, pp. 2652–2658, 1992.

[12] R. L. Kinder and M. J. Kushner, “Consequences of mode structure on plasma properties in electron cyclotron resonance sources,” J. Vac. Sci. Technol. A, Vac. Surf. Films, vol. 17, no. 5, pp. 2421- 2430, 1999.

[13] Y. Yasaka and N. Uda, “Practical scheme for three-dimensional simulation of electron cyclotron resonance plasma reactors,” J. Appl. Phys., vol. 89, no. 7, pp. 3594–3601, 2001.

[14] A. Lieberman and A. J. Lichtenberg, Principals of Plasma Discharges and Materials Processing. New York, NY, USA: Wiley, 1994.

[15] D. A. Carl, M. C. Williamson, M. A. Lieberman, and A. J. Lichtenberg, "Axial radio frequency electric field intensity and ion density during low to high mode transition in argon electron cyclotron resonance discharges," J. Vac. Sci. Technol. B, Microelectron., vol. 9, no. 2, pp. 339–347, 1991.

[16] O. A. Popov, "Effects of magnetic field and microwave power on electron cyclotron resonance–type plasma characteristics," J. Vac. Sci. Technol. A, Vac., Surf., Films, vol. 9, no. 3, pp. 711–716, 1991.

[17] Y. Ueda, and Y. Kawai, "Effect of upper hybrid waves on uniform electron cyclotron resonance plasmas," J. Vac. Sci. Technol. A, vol. 16, no. 3, p.1454 ,1998.

[18] Y. Ueda, H. Muta, and Y. Kawai, "Role of peripheral vacuum regions in the control of the electron cyclotron resonance plasma uniformity," Appl. Phys. Lett., vol. 74, no. 14, p. 1972 ,1999.

[19] M. Furuse, S. Watanabe, **H. Tamura**, and O. Fukumasa, "Production of highly uniform electron cyclotron resonance plasmas by distribution control of the microwave electric field," J. Vac. Sci. Technol. A, Vac., Surf., Films, vol. 17, no. 6, pp. 3225–3229, 1999.

[20] H. Muta, Y. Ueda, and Y. Kawai, "Investigation of the microwave propagation in an ECR plasma using a self-consistent particle-wave model," Surf. Coat. Technol., vol. 131, nos. 1–3, pp. 44–49, 2000.

[21] T. Kaneko, K. Takahashi, and R. Hatakeyama, "Verification of polarization reversal of electromagnetic waves with electron cyclotron frequency controlling plasma-structure formation," Plasma Fusion Res., vol. 2, 038, 2007.

[22] K. Maeda, S. Obama, **H. Tamura**, G. Miya, and M. Izawa, "Study on the distribution control of etching rate and critical dimensions in microwave electron cyclotron resonance plasmas for the next generation 450 mm wafer processing," Jpn. J. Appl. Phys., vol. 51, Aug. 2012, Art. no. 08HD01.

[23] **H. Tamura**, T. Tetsuka, N. Tamari, D. Kuwahara, and S. Shinohara, "Numerical identification of Trivelpiece–Gould waves in an electron cyclotron resonance etching reactor," IEEE Trans. Plasma Sci., vol. 46, no. 10, pp. 3662–3668, 2018.

[24] A. W. Trivelpiece and R. W. Gould, "Space charge waves in cylindrical plasma columns," J. Appl. Phys., vol. 30, no. 11, pp. 1784-1793, 1959.

[25] D. G. Swanson, Plasma Waves. San Diego, CA, USA: Academic, 1989.

[26] S. Matsuo and Y. Adachi, "Reactive ion beam etching using a broad beam ECR ion source," Jpn. J. Appl. Phys., vol. 21, pp. L4-L6 1982.

[27] S. Nakayama, "ECR (electron cyclotron resonance) plasma for thin film technology," Pure & Appl. Chem., vol. 62, No.9, pp. 1751-1756, 1990.

[28] T. Ono, H. Nishimura, M. Shimada, and S. Matsuo, "Electron cyclotron resonance plasma source for conductive film deposition," J. Vac. Sci. Technol., A12(4), p.1281, 1989

[29] Z. Bi, Y. Liu, W Jiang, X. Xu, and Y. Wang, "A brief review of dual-frequency capacitively coupled discharges," Current Applied Physics, vol. 11, Issue 5, Supplement, pp. S2-S8 2011.

[30] H. Lee, "Review of inductively coupled plasmas: Nano-applications and bistable hysteresis physics," Applied physics reviews, 5, 011108 (2018).

[31] S. Watanabe, M. Sumiya, and S. Kawasaki, "Concentric Spread Plasma Source," Jpn. J. Appl. Phys., vol 37, pp. 5751-5756, 1998

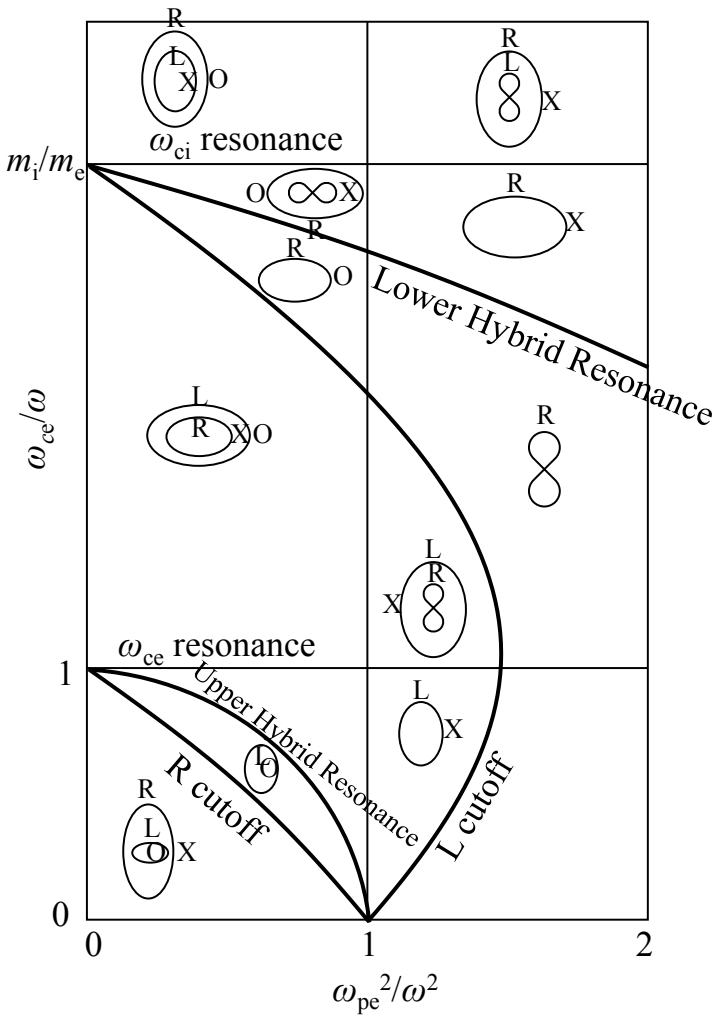

Fig. 1.1 A Clemmow–Mullaly–Allis (CMA) diagram for classification of waves in a cold plasma

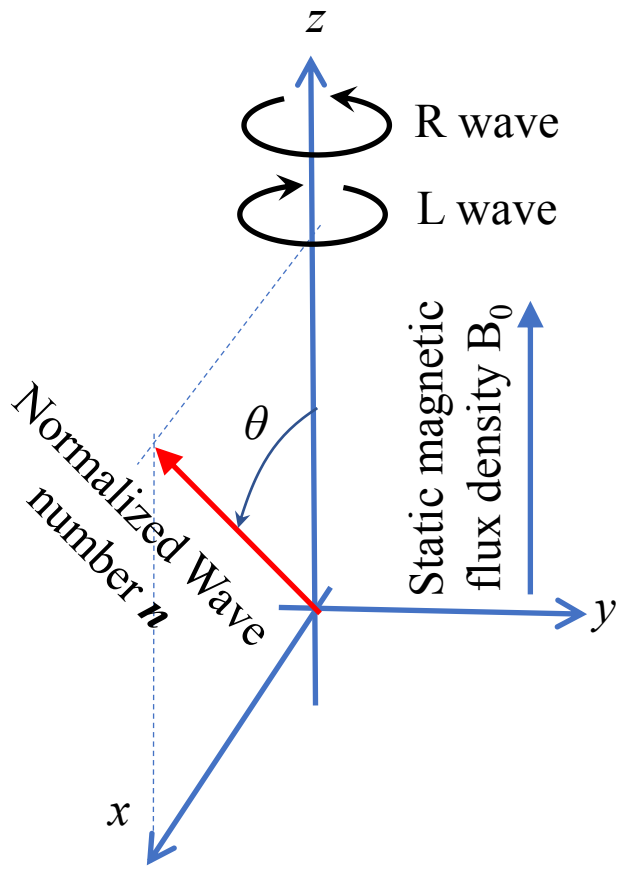

Fig. 1.2 Coordinate system used for microwave propagation in magneto plasma.

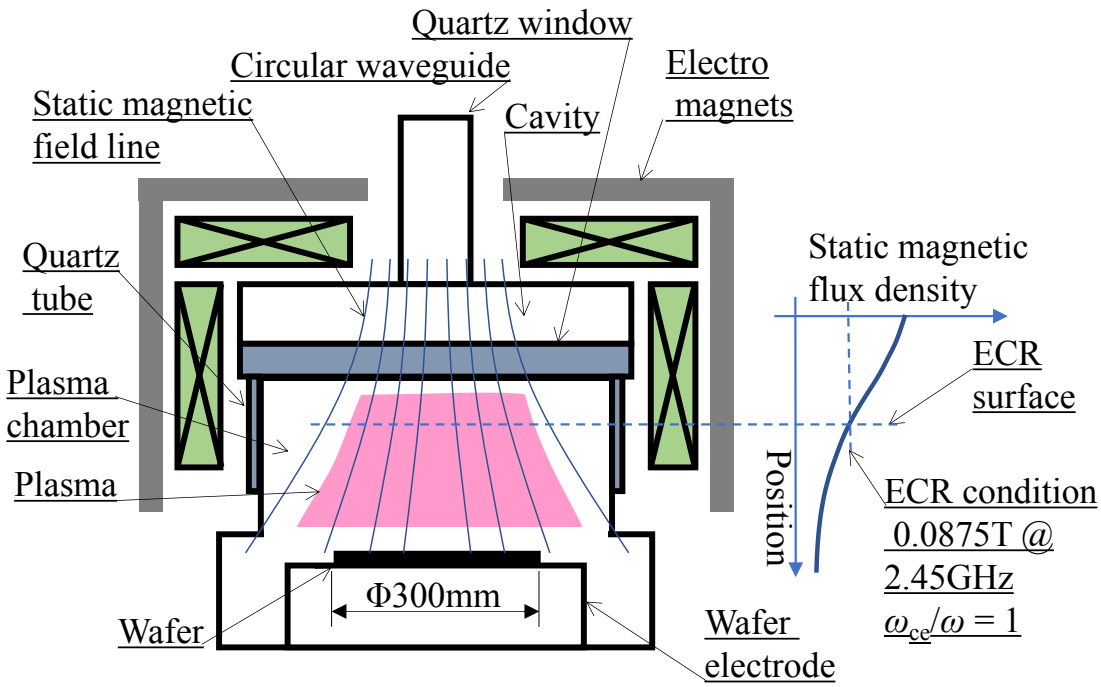

Fig. 1.3 Typical ECR reactor and static magnetic field distribution based on *magnetic beach concept*.

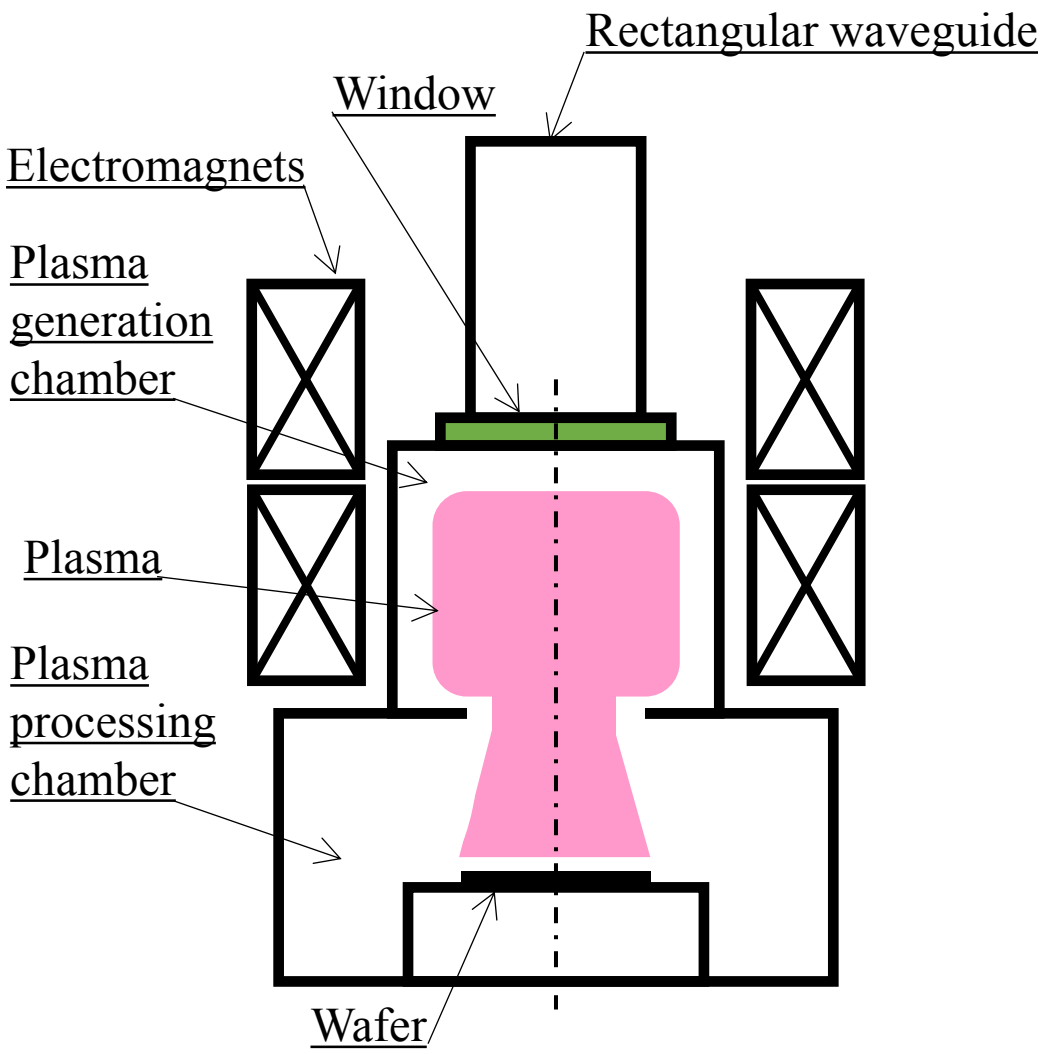

Fig. 1.4 An example of the ECR plasma reactor "NTT system".

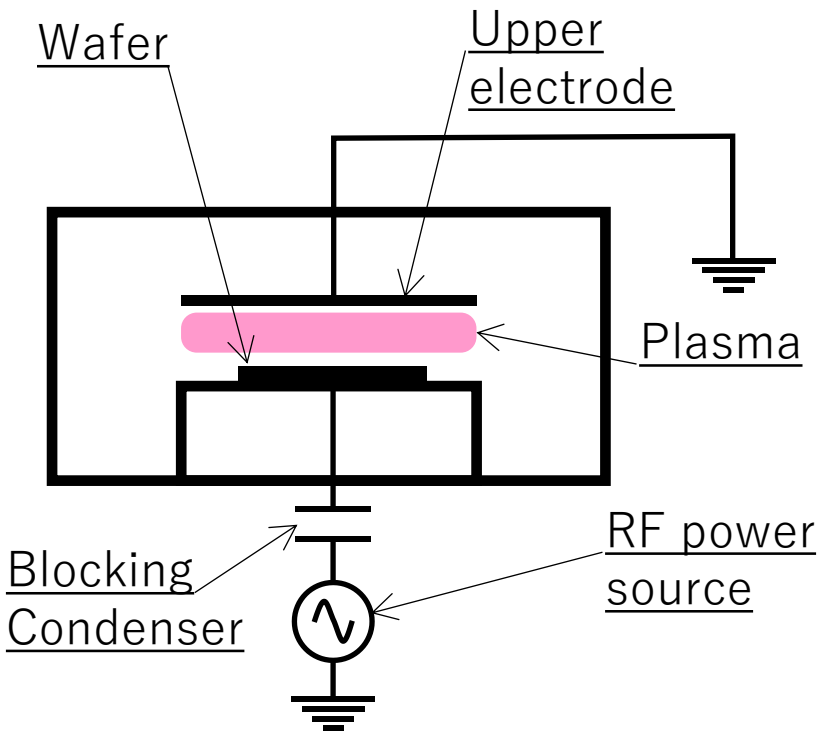

Fig. 1.5 Typical configuration of capacitively coupled plasma.

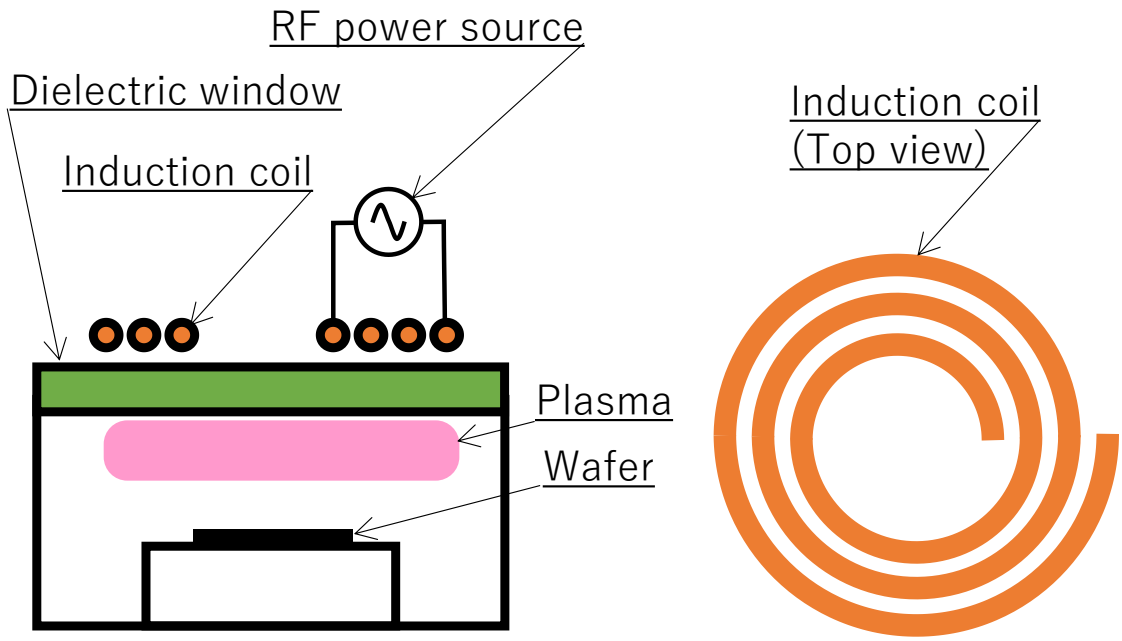

Fig. 1.6 Typical configuration of inductively coupled plasma.

Chapter 2

2. Numerical Identification of Trivelpiece–Gould Waves in an Electron Cyclotron Resonance Etching Reactor

2.1 Introduction

In this chapter, microwave analysis in the ECR plasma reactor is investigated and its simulation tool is validated. The microwave electric field distribution results showed very complex patterns, as will be discussed later in Fig. 2.2(b). At first, we suspected that the result might be spurious because the calculation tool we used is based on FEM and microwave analysis by ordinary FEM might produce the problem of spurious solutions, as mentioned in Chapter 1. The patterns will be investigated in detail to determine whether they are spurious or not, which also reveals the accuracy of the wave analysis using this simulation tool. Moreover, the calculation result of the tool will be checked by comparing them with the results of theoretical analysis. After describing an electrostatic wave called the Trivelpiece-Gould wave (TG wave) [1], the relationship between the very complex patterns, obtained from our simulations, and the TG wave will be discussed.

The model and calculation procedure are described in Section 2.2, followed by the calculation results and discussion in Sections 2.3 and 2.4, respectively. In Section 2.3, we consider the complex jagged patterns that form under various plasma density and static magnetic field conditions. In Section 2.4, after checking the validity of the present tool for analysis, we have examined the jagged pattern by comparing the simulation results

with wave theory, and found that the patterns show characteristics of TG waves. Concluding remarks are presented in Section 2.5.

2.2 Modeling and calculation procedure

2.2.1 Modeling

We used a 2-D axisymmetric model for the microwave analysis. The configuration of the model is the same as the typical ECR reactor described in Section 1.3 and shown in Fig. 1.3. Plasma density was set to be uniform in the chamber and a plasma sheath between the wall and the bulk plasma was not considered.

To make the simulation easier, the simplified reactor model shown in Fig. 2.1(b) was also used [2]. Microwaves with f = 2.45 GHz were introduced into the plasma chamber through a single-mode circular waveguide with a diameter of 90 mm. Here, the microwave mode in the circular waveguide was TE_{11}. A quartz window was positioned between the plasma chamber and circular waveguide. To decrease microwave reflection at the end boundary of the plasma chamber [Fig. 2.1(b) (bottom)], a matching layer was included. The impedance of the matching layer was set to be nearly the same as that of the plasma region, so that the reflection due to impedance mismatch at the interface of plasma and the matching layer is decreased. A uniform static magnetic field was applied along the axis of the model, and the plasma chamber was filled with uniform cold plasma.

We used the triangular mesh shown in Fig. 2.1(a) [2]. To calculate the complicated electromagnetic field pattern, fine mesh elements that are smaller than the features of the complicated pattern are needed. Here, we used a fine mesh whose node distance was less than 2 mm in the whole plasma chamber of the typical ECR reactor and the simplified reactor model. It took a couple of minutes to calculate microwave electric

field for these models using the fine mesh by a Windows-based PC with a Xeon® 3.4GHz CPU. To calculate the microwave electromagnetic field numerically with a high resolution, usually more than 10 nodes in a wavelength are needed. This node distance, which is less than 2 mm, corresponds to the wavelength of less than 20 mm.

2.2.2 Calculation procedure

The calculation method for the 2-D axisymmetric microwave ECR plasma is similar to that in [3]. The microwave electric field in the plasma chamber can be solved by the following wave equation, which is called the Helmholtz equation:

$$\nabla \times \nabla \times \mathbf{E} - \omega^2 \varepsilon_0 \mu_0 \boldsymbol{\varepsilon} \mathbf{E} = 0, \tag{2.1}$$

where ω is the angular frequency of the microwave, ε_0 and μ_0 are the permittivity and permeability of free space, respectively, and $\boldsymbol{\varepsilon}$ is the permittivity tensor of the cold plasma [4] [see Eq. (1.9)]. In other regions of the model (the circular waveguide, the cavity, the quartz window, and the quartz tube), relative permittivity of the medium (vacuum or quartz) is used instead of the permittivity tensor. We imposed perfect conductor conditions on the boundaries of the waveguide, the cavity, and the chamber wall, namely the electric field parallel to the boundaries is zero. As for the permittivity tensor $\boldsymbol{\varepsilon}$, a static magnetic field distribution shown in Fig. 2.2(a) is considered for the model of a typical ECR reactor, and the plasma density is assumed to be uniform in the reactor. For the simplified reactor model, the permittivity tensor $\boldsymbol{\varepsilon}$ is assumed to be uniform in the reactor that corresponds to uniform plasma density and uniform static magnetic field.

The static magnetic field distribution for the typical ECR reactor model was calculated by the following equation:

$$\nabla^2 \mathbf{A} - \mu_0 \mathbf{J} = 0, \tag{2.2}$$

where **A** is the vector potential and **J** is the coil current density. The static magnetic flux density $\mathbf{B}_0$ was calculated by the following equation:

$$\mathbf{B}_0 = \nabla \times \mathbf{A}. \tag{2.3}$$

For the simplified reactor model, a uniform magnetic flux density was applied along the axis. The plasma chamber was filled with uniform plasma for each model. Each element of the permittivity tensor depends on plasma density and static magnetic field distribution. For the typical ECR reactor model, magnetic flux density distribution [see Fig. 2.2(a)] was considered. For the simplified reactor model, we used a uniform permittivity tensor in the plasma chamber.

We used the differential equation solver of COMSOL Multiphysics® [5] to solve (2.1) and (2.2), respectively. We employed the boundary conditions and the parameters of the medium as mentioned earlier. When the Helmholtz equation of Eq. (2.1) is solved, the tool uses the special method of FEM that prevents the contamination of the solution by spurious solutions, which is briefly described in Chapter 1. However, the detailed calculation method of the tool cannot be identified since the tool is commercially available and its code is not publicly disclosed. Therefore, we validate the result of the tool carefully as mentioned later in this chapter.

An analytical solution for a circular waveguide filled with the cold magnetized plasma is provided in [6]. We applied the solution to the simplified reactor model [see Fig. 2.1(b)] to identify the result of the simulation tool. The dispersion relation and boundary condition for a waveguide filled with cold magnetized plasma are derived in [6]. The dispersion relation is briefly described in Section 1.2 [see Eq. (1.19)]. We calculated the analytical field distribution using these two nonlinear equations.

2.3 Calculation results

2.3.1 Electric fields in the plasma chamber

Before using the simplified plasma generation conditions in Fig. 2.1(b), the calculation results for the typical ECR reactor model are considered, as shown in Fig. 2.2 [2] [see also Fig. 1.3]. Figure 2.2(a) [2] displays the magnetic flux density distribution calculated for the typical ECR reactor. A divergent magnetic field based on the magnetic beach concept was applied to the plasma chamber, whose ECR region was 0.0875 T, and the field strength was almost flat along the radial direction.

Figure 2.2(b) [2] shows the simulated microwave electric field in the case of a uniform high-density (10^{17} m^{-3}) plasma. Very complicated jagged patterns were found in the high magnetic field region. In contrast, the jagged pattern was not found in the case of a uniform low-density plasma (10^{16} m^{-3}) and a high electric field at ECR surface is clearly observed [see Fig. 2.2(c)]. We use ω_{pe}^2/ω^2 (or ω_{pe}/ω) and ω_{ce}/ω instead of plasma density and static magnetic field hereinafter, since plasma density and static magnetic field are proportional to ω_{pe}^2 and ω_{ce} as explained in Section 1.2. A plasma density of 7.5 $\times$ 10^{16} m^{-3} and a static magnetic field of 0.0875 T are equivalent to $\omega_{pe}^2/\omega^2 = 1$ (or $\omega_{pe}/\omega = 1$) and $\omega_{ce}/\omega = 1$, respectively, for a microwave frequency of 2.45 GHz. Here, ω is the

microwave angular frequency, ω_{pe} is the plasma angular frequency, and ω_{ce} is the electron cyclotron angular frequency.

Comparing the results for a static magnetic field [Fig. 2.2(a)] and a microwave electric field of the high-density case [Fig. 2.2(b)], the jagged pattern was found only in the region of high magnetic field larger than the ECR condition of 0.0875 T ($\omega_{ce}/\omega > 1$).

2.3.2 Simplified reactor model (Small-diameter plasma chamber)

After examining various cases, it was found that the jagged pattern was observed in the high-density of $\omega_{pe}^2/\omega^2 > 1$ and the strong magnetic field region of $\omega_{ce}/\omega > 1$ for the typical ECR reactor model. However, there is a possibility that this jagged pattern will also appear in other parameter regions. To investigate the conditions needed to form the jagged pattern in more detail, various plasma densities and static magnetic fields were applied to the simplified reactor model in Fig. 2.1(b). Figure 2.3 [2] illustrates three examples of the calculation results. As shown in Fig. 2.3(a) and (b), slanted line patterns, which are equivalent to the jagged pattern in the typical ECR reactor [see Fig. 2.2(b)], were observed when the plasma density was as high as $\omega_{pe}^2/\omega^2 > 1$. Conversely, in the case of low-density of $\omega_{pe}^2/\omega^2 < 1$ [Fig. 2.3(c)], no sharp slanted lines or jagged patterns were seen.

Figure 2.4 shows the regions where the jagged pattern formed. Here, "○" and "×" indicate the cases with and without the jagged patterns observed in simulations, respectively. The jagged patterns appeared in the following regions 1 and 2, the conditions of which are as follows. Region 1: high density ($\omega_{pe}/\omega > 1$) and high magnetic field (ω_{ce}/ω

> 1), and Region 2: low density (ω_{pe}/ω < 1) and low magnetic field (ω_{ce}/ω < 1) and $(\omega_{pe}/\omega)^2 + (\omega_{ce}/\omega)^2 > 1$.

2.4 Discussion

2.4.1 Verification of the FEM tool

It is well-known that spurious solutions are sometimes obtained for electromagnetic analysis using the ordinary FEM [7] as mentioned in Chapter 1. We suspected that it was possible that the jagged pattern was spurious. To validate that the calculation tool was effective, we compared an analytical solution with our simulation result for the simplified reactor model.

We compared the analytical solution [6] and the result of the simulation tool for a circular waveguide filled with cold magnetized plasma. The equations of the analytical solution for a circular waveguide filled with uniform plasma with a static magnetic field along the axis are presented in [6], and the dispersion relation [Eq. (1.19)] is briefly explained in Section 1.2. We numerically calculate the analytical solution. Figure 2.5 [2] presents the results for the two cases. The wavelength and waveforms of the electric fields coincide with each other. Thus, the FEM tool using COMSOL Multiphysics®, is suitable for these systems.

2.4.2 Trivelpiece-Gould wave (TG Wave)

We investigated electromagnetic waves in magnetized plasma and found that the propagation region of TG waves coincided with the region where the jagged pattern was observed. Here, we discuss the dispersion relation of the TG waves [1], which is written as

$$\beta = \pm T \left[\frac{-\omega^2(\omega^2 - \omega_{pe}{}^2 - \omega_{ce}{}^2)}{(\omega^2 - \omega_{pe}{}^2)(\omega^2 - \omega_{ce}{}^2)} \right]^{\frac{1}{2}},$$

$$T = \frac{p_{n,v}}{a}, \tag{2.4}$$

where β is the phase constant of the TG wave, a is the waveguide radius, $p_{n,v}$ is the vth zero of the nth-order Bessel function, and T is the propagation constant of the radial direction. Two propagation regions (with β real), derived using Eq. (2.4), are shown in Fig. 2.4 (colored yellow), which coincide with the region where the jagged pattern was observed.

In addition, we investigated the angle of the jagged pattern for the simplified reactor model (see Fig. 2.6) to compare it to the theoretical TG wave propagation angle. Anderson *et al*. [8] stated that a complicated many-wave structure is formed by mixing degenerate TG waves in a Penning–Malmberg trap. The result is that the ratio of β–T is constant with the same ω, ω_{pe}, and ω_{ce} despite different n or v in the dispersion relation of Eq. (2.4). Here, the ratio of β–T is related to the wave propagation angle. Figure 2.7 [2] shows superimposed TG waves with various v values. As the number of waves increases, a jagged pattern is clearly observed.

We measured the angle of the jagged pattern (see Fig. 2.6) from the electric field distribution results and compared it with $\tan^{-1}(T/\beta)$ calculated by Eq. (2.4). These angles also coincided very clearly with each other, as illustrated in Figs. 2.8 (as functions of ω_{ce}/ω and ω_{pe}/ω) and 2.9 (combined data from Fig. 2.8).

These results showed clearly that the jagged pattern observed in the typical ECR reactor [see Fig. 2.2(b)] was not spurious but originated from TG waves and that it was

only possible that the jagged patterns emerged in the regions indicated in Fig. 2.4 where TG waves occur. However, it is not clear that the jagged pattern is important to control the characteristics of the plasma process on the wafer. To better understand this, it is important to analyze the electromagnetic field for a reasonable plasma distribution. We have already confirmed a ring-shaped plasma distribution in the reactor of the ECR plasma etcher by measuring the ion saturation current distribution [9]. Microwave electromagnetic field analysis with consideration of the plasma distribution is discussed in Chapter 4.

2.5 Chapter conclusion

We calculated the microwave electromagnetic field in a typical ECR reactor by the FEM to simulate an ECR plasma reactor. We found that complicated jagged patterns were formed in the reactor under certain conditions. We investigated the conditions where the jagged pattern was formed using a small-diameter plasma chamber model and found that they agreed with the propagation region of the TG wave. Furthermore, we identified that the angle of the jagged patterns coincided with the theoretical value of the TG wave. At first, we suspected that the jagged patterns resulted from spurious solutions, which are often observed in electromagnetic field analysis by ordinary FEM analysis. However, they are not spurious, and these results clearly revealed that the jagged patterns actually originated from the TG wave, which has a very short wavelength, hard to be recognized experimentally. This chapter also showed that the analysis by this simulation code is a powerful approach to analyze electromagnetic fields in ECR plasma, because even very fine wave structures can be identified, down to 2 mm size [see Fig. 2.1(b)]. It is possible that the controllability of the plasma distribution can be improved in ECR plasma reactors

by TG wave generation because the wavelength of TG waves can be very short under certain conditions, as mentioned and therefore TG waves have a crucial effect on ECR plasma generation. Experimental identification of TG waves in ECR plasma reactors is still required. To measure TG wave in an ECR plasma reactor, high spatial resolution is needed because TG wave have a fine structure.

References

[1] A. W. Trivelpiece and R. W. Gould, "Space charge waves in cylindrical plasma columns," J. Appl. Phys., vol. 30, no. 11, pp. 1784-1793, 1959.

[2] **H. Tamura**, T. Tetsuka, N. Tamari, D. Kuwahara, and S. Shinohara, "Numerical identification of Trivelpiece–Gould waves in an electron cyclotron resonance etching reactor," IEEE Trans. Plasma Sci., vol. 46, no. 10, pp. 3662–3668, 2018.

[3] Y. Yasaka, A. Fukuyama, A. Hatta, and R. Itatani, "Two–dimensional modeling of electron cyclotron resonance plasma production," J. Appl. Phys., vol. 72, no. 7, pp. 2652–2658, 1992.

[4] T. H. Stix, Waves in Plasmas. New York, NY, USA: Springer, 1992.

[5] COMSOL Multiphysics® Software. Accessed: 2020. [Online]. Available: https://www.comsol.com/

[6] D. G. Swanson, Plasma Waves. San Diego, CA, USA: Academic, 1989.

[7] M. Koshiba and K. Inoue, "Simple and efficient finite-element analysis of microwave and optical waveguides," IEEE Trans. Microw. Theory Techn., vol. 40, no. 2, pp. 371–377, 1992.

[8] M. W. Anderson T. M. O'Neil, D. H. E. Dubin, and R. W. Gould, "Degenerate mixing of plasma waves on cold, magnetized single-species plasmas," Phys. Plasmas, vol. 18, no. 10, 2011, Art. no. 102113.

[9] K. Maeda, S. Obama, **H. Tamura**, G. Miya, and M. Izawa, "Study on the distribution control of etching rate and critical dimensions in microwave electron cyclotron resonance plasmas for the next generation 450 mm wafer processing," Jpn. J. Appl. Phys., vol. 51, no. 8S1, p. 08HD01, 2012.

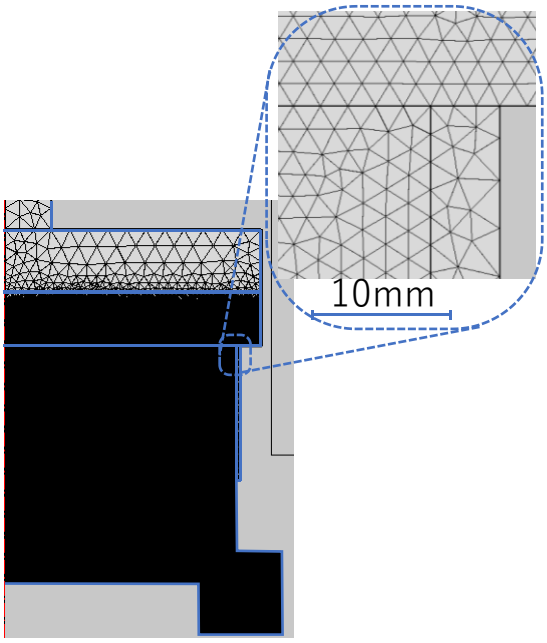

(a)

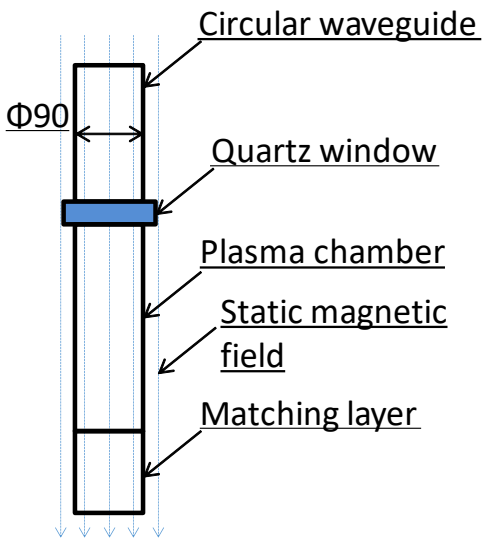

(b)

Fig. 2.1. Simulation models [2].

(a) Mesh for typical ECR reactor model and (b) simplified reactor model.

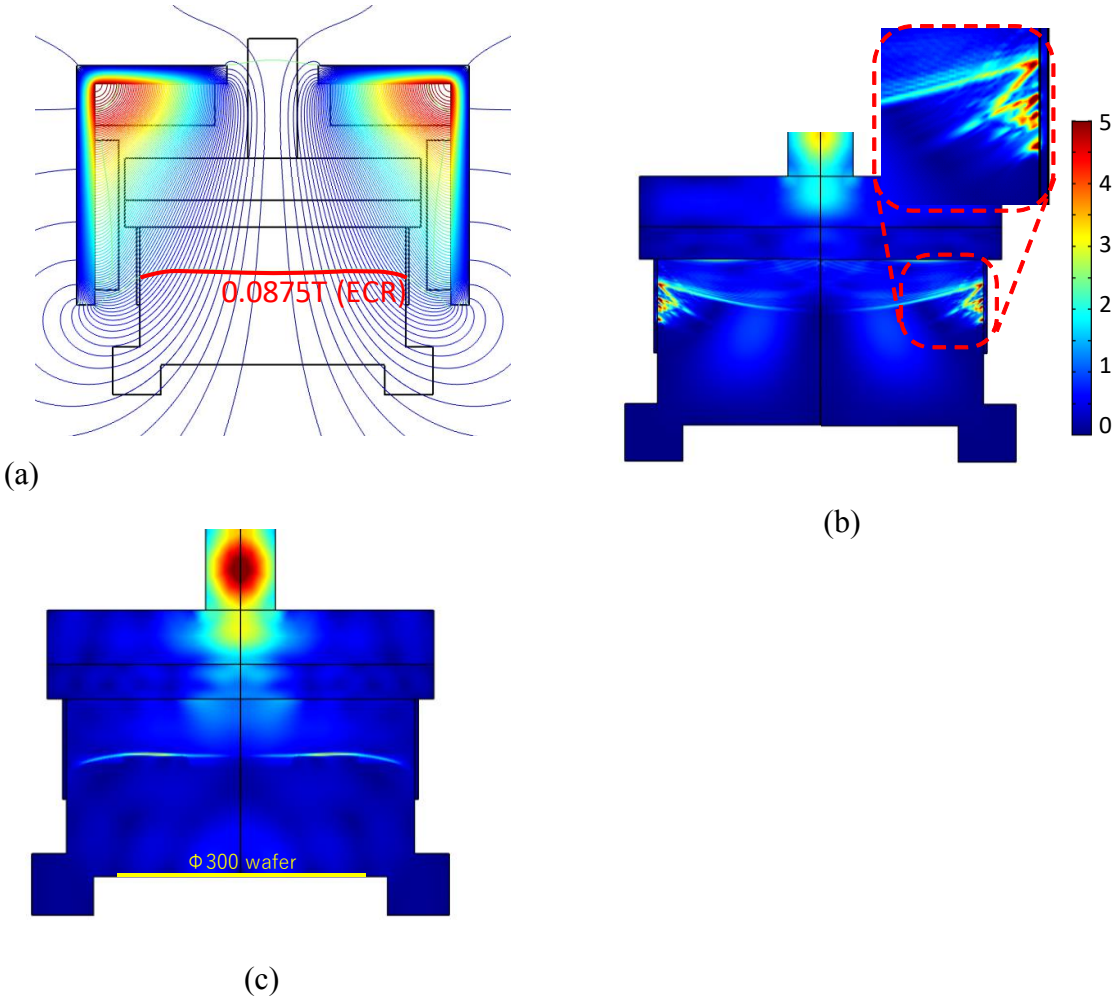

(a)

(b)

(c)

Fig. 2.2. Static magnetic field and electric field distributions in the typical ECR reactor [2]**.**

(a) Static magnetic field lines. (b) Electric field distribution for a uniform plasma density of 10^{17} m^{-3}. (c) Electric field distribution for a uniform plasma density of 10^{16} m^{-3}. The results of (b) and (c) were obtained with COMSOL Multiphysics® tool using the permittivity tensor of cold plasma.

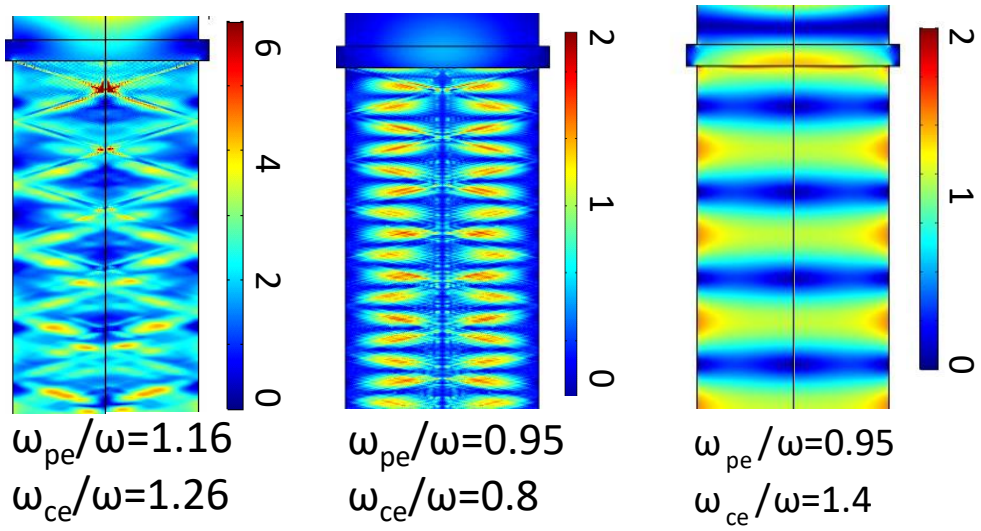

(a) (b) (c)

Fig. 2.3. Electric field in the simplified reactor model (a) and (b) with and (c) without the jagged patterns [2].

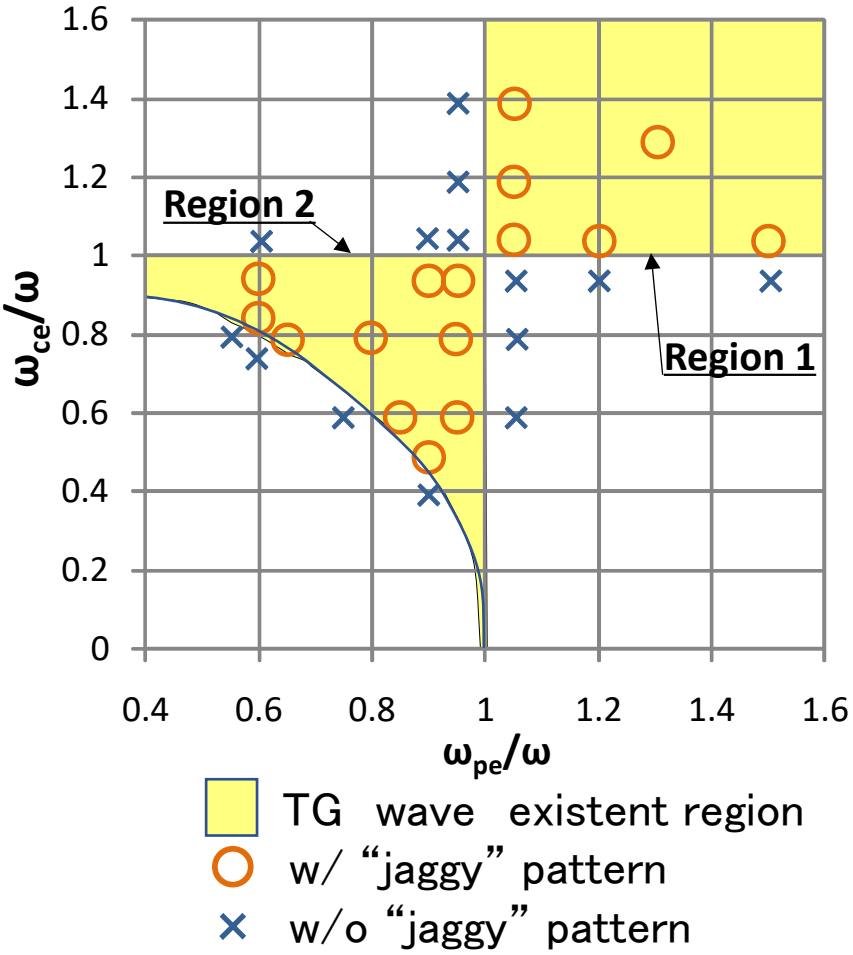

Fig. 2.4. Regions with TG waves and jagged patterns [2].

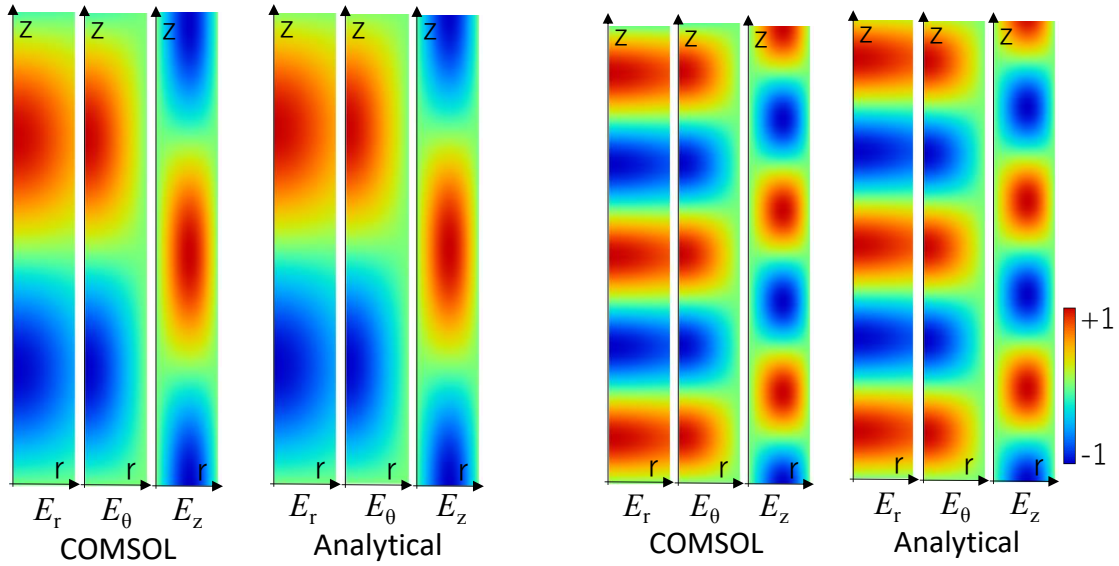

(a) $B_z = 0.04$ (T) and $n_e = 10^{16}$ (m^{-3}) (b) $B_z = 0.09$ (T) and $n_e = 10^{15}$ (m^{-3})

Fig. 2.5. Electric field comparison of analytical solution and the simulation tool for (a) $B_z = 0.04$ (T) and $n_e = 10^{16}$ (m^{-3}) and (b) $B_z = 0.09$ (T) and $n_e = 10^{15}$ (m^{-3}), where B_z is the magnetic flux density along the axis and n_e is the plasma density [2].

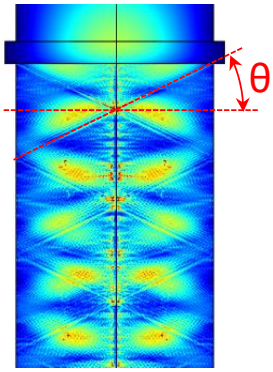

Fig. 2.6. Wave propagation angle of the jagged pattern [2]**.**

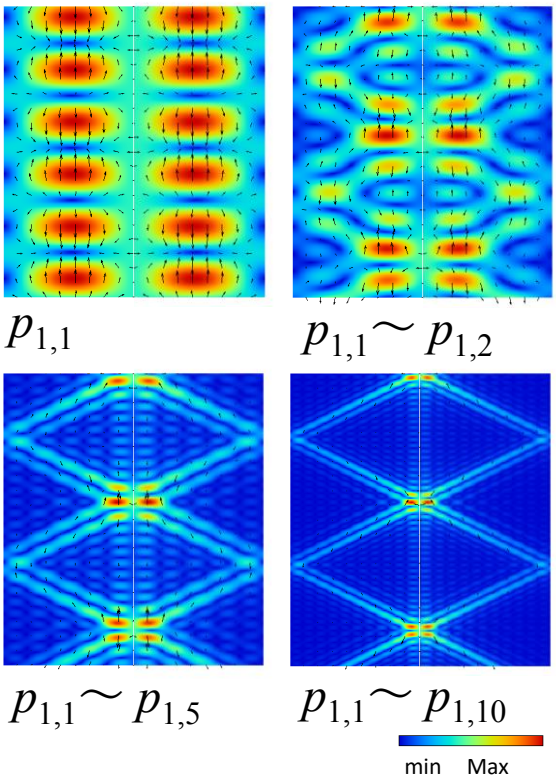

Fig. 2.7. Jagged pattern made by mixing degenerate TG waves [2]**.**

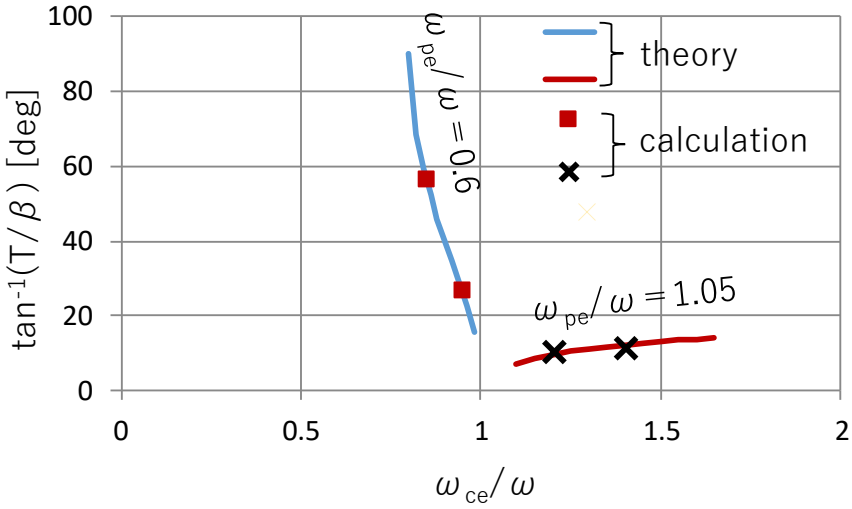

(a) ω_{ce}/ω

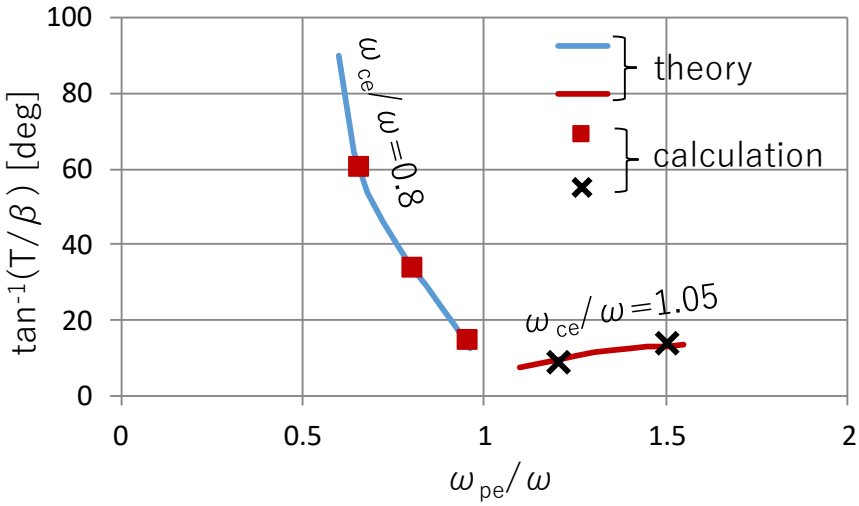

(b) ω_{pe}/ω

Fig. 2.8. Angles of β/T obtained by calculation and theory [8] as a function of (a) ω_{ce}/ω and (b) ω_{pe}/ω, where β is the phase constant of TG waves, T is the propagation constant to the radial direction, ω_{ce} is the cyclotron angular frequency, ω_{pe} is the plasma angular frequency, and ω is the microwave angular frequency [2].

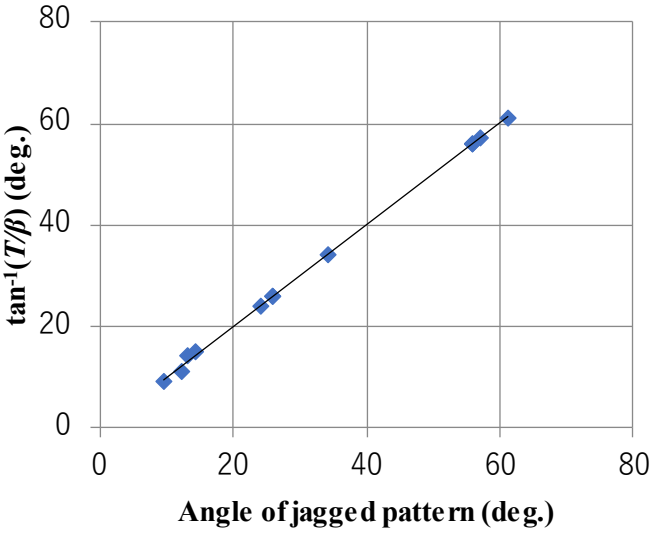

Fig. 2.9. Relationship between theoretical and calculated angles of *β*–*T* obtained by combining the data in Fig. 2.8 [2]**.**

Chapter 3

3. Study on Uniform Plasma Generation Mechanism of Electron Cyclotron Resonance Etching Reactor

3.1 Introduction

In Chapter 2, the validity of the microwave analysis in the ECR reactor was verified with a good spatial accuracy. In this chapter, we combine the verified microwave analysis tool with the developed plasma generation analysis code and a similar plasma diffusion analysis code to simulate the plasma generation and distribution in the ECR reactor in a consistent way. Then, we confirm the simulation results via comparison with measured plasma distribution results. Using the simulation results, the mechanism for uniform plasma generation is discussed. Additionally, a theoretical solution for a magnetic plasma-filled waveguide [1] is evaluated to validate the simulated microwave propagation results in the ECR plasma reactor, and the uniform plasma generation mechanism is discussed.

The contents of this chapter are as follows. The model and the calculation procedure are shown in Section 3.2. The calculation and measurement results, to validate the simulation method along with the results of the microwave analysis in the reactor, is presented in Section 3.3. In Section 3.4, microwave propagation in the etching reactor with a static magnetic field, while considering the boundary conditions, is discussed. Concluding remarks are presented in Section 3.5.

3.2 Modeling and calculation procedure

3.2.1 Modeling

A 2-D axisymmetric model to analyze the ECR plasma characteristics is used. The model is the same as the one shown in Fig. 1.3 and has already been explained in Section 1.3. The plasma sheath between the wall and the bulk plasma is not considered in the calculations. The triangular mesh shown in Fig. 2.1(a) [2] is used in this simulation. To calculate the complex electromagnetic field pattern, fine mesh elements that are smaller than the complex pattern, are required. In the plasma chamber, a fine mesh with a node distance of less than 2 mm is used. Argon as the working gas is considered to make the plasma composition simple. The plasma sheath is relatively thin, whose thickness is several times of the Debye length λ_D, since the plasma density is high. The inner surface of the upper part of the reactor is covered by quartz, which is made of a dielectric material. Therefore, the sheath layer is treated as an additional thin capacitive layer, mainly on the quartz surface, and its effect small.

3.2.2 Calculation procedure

The calculation procedure is illustrated in Fig. 3.1 [2]. First, the static magnetic field is calculated, and a uniform low-density plasma is distributed in the plasma chamber as the initial condition. Next, the microwave electric field, the plasma generation process, and the plasma diffusion are analyzed. These three analyses are iterated to determine a final steady state solution. The procedure of the microwave analysis is the same as the one described in Chapter 2. We add the analyses of the plasma generation region and the plasma diffusion and calculate them in a consistent way.

The microwave electric field in the plasma chamber can be solved using the following wave equation [3], which is identical to Eq. (2.1):

$$\nabla \times \nabla \times \mathbf{E} - \omega^2 \varepsilon_0 \mu_0 \boldsymbol{\varepsilon} \mathbf{E} = 0, \tag{3.1}$$

where ε_0 and μ_0 are the permittivity and the permeability in a vacuum, respectively, and $\boldsymbol{\varepsilon}$ is the permittivity tensor of the cold plasma of Eq. (1.9) [3, 4]. In the other regions in the model (i.e., the waveguide, cavity, quartz window, and quartz tube), the relative permittivity of the medium (i.e., vacuum or quartz) is used rather than the permittivity tensor. Microwaves are introduced via the TE_{11} mode of the circular waveguide, as described above, and thus we calculate the microwave dependence on azimuthal direction as $m = 1$. Metal surfaces in the model such as the waveguide wall, the cavity wall, and the reactor wall are treated as perfect conductors. Therefore, the tangential component of the electric field is zero on the metal surface. On other boundaries such as vacuum-quartz interface, and plasma-quartz interface, we apply the condition that the tangential electric component is continuous.

It is known that the ECR region becomes thicker than the value obtained by cold plasma approximation, because of the Doppler shift effect present in a hot plasma [4], as mentioned in Section 1.2. We calculated the microwave electric field by using a modified collision frequency in cold plasma to simulate hot plasma. We added an effective term representing $k_{//}v_{\mathrm{the}}$ to the ordinary collision frequency, where $k_{//}$ is a wavenumber along a parallel direction and v_{the} is the velocity of electrons [see Eqs. (1.28) and (1.29)]. The plasma permittivity tensor does not have the problem of tending to infinity near the ECR

region because of the collision term. This treatment can also explain approximately the power absorption due to electron cyclotron damping based on the hot plasma theory [4].

We assume the microwave power is absorbed only by electrons in the plasma, because other heavy charged particles (i.e., ions) cannot follow the high frequency change of the microwave. We analyze the electron temperature using the following diffusion equation of energy:

$$\nabla \cdot \nabla(\mathbf{D}_\varepsilon n_\varepsilon) + S_\varepsilon = 0, \tag{3.2}$$

where $\mathbf{D}_\varepsilon$ is the diffusion coefficient tensor of the energy, n_ε is the energy density of electrons, and S_ε is the source energy [5, 6]. Here, $\mathbf{D}_\varepsilon$ is given by

$$\mathbf{D}_\varepsilon = \frac{5}{3}\frac{D_a}{d_s}\begin{bmatrix} 1 + {\mu_a}^2 {B_{0r}}^2 & {\mu_a}^2 B_{0r} B_{0z} \\ {\mu_a}^2 B_{0r} B_{0z} & 1 + {\mu_a}^2 {B_{0z}}^2 \end{bmatrix}, \tag{3.3}$$

$$d_s = 1 + {\mu_a}^2 |\mathbf{B}|^2,$$

$$D_a = (\mu_i D_e + \mu_e D_i)/(\mu_i + \mu_e),$$

$$\mu_a = 2\mu_i \mu_e/(\mu_i + \mu_e),$$

where $|\mathbf{B}|$ is the magnitude of the static magnetic flux density, B_{0r} and B_{0z} are the static magnetic flux densities of the r and z components, respectively, in a cylindrical geometry, $D_e = k_B T_e/m_e/\nu_e$ and $D_i = k_B T_i/m_i/\nu_i$ are the electron and ion diffusion coefficients, respectively, and $\mu_e = e/m_e/\nu_e$ and $\mu_i = e/m_i/\nu_i$ are the electron and ion mobilities, respectively. Here, k_B is the Boltzmann constant, T_e is electron temperature in kelvin, m_e is the electron mass, ν_e is collision frequency between electrons and neutral gas molecules,

T_i is the ion temperature in kelvin, m_i is the ion mass, ν_i is collision frequency between ions and neutral gas molecules, and e is the elementary charge. Ions with an electric charge of 1 are considered.

We consider the Ar reaction in the plasma as shown in Table 3.1, and we use the rate coefficient for each reaction as described in [7]. By using this rate coefficient, and considering the electron temperature and the density of each species (i.e., electron, excited argon, argon ion, and neutral argon), the generation rate of each species can be calculated.

Ions generally diffuse together with electrons, since ions and electrons attract each other by electrostatic force. This phenomenon is well known as ambipolar diffusion. We therefore treat the plasma diffusion as ambipolar diffusion. The diffusion coefficient for ambipolar diffusion without the static magnetic field is provided in many books (see e.g., [4, 9]). Yasaka and Uda [8] briefly reported results for an ambipolar diffusion tensor in a magnetized plasma. However, they did not explain their derivation explicitly.

Here, we have derived an ambipolar diffusion tensor in a magnetized plasma using an ordinary procedure. At first, an ambipolar electric field is derived by assuming that electron flux and ion flux are the same. Next, by eliminating the electric field in the diffusion equation, the ambipolar diffusion tensor can be derived. Use of this tensor allows the diffusion analysis to be simplified. The plasma density distribution can then be analyzed using the following diffusion equation:

$$\nabla \cdot (\mathbf{K}_a \nabla n) + S = 0, \tag{3.4}$$

where $\mathbf{K}_a$ is the diffusion coefficient tensor, n is the plasma density, and S is the source of the plasma generation.

We assume that the ions and electrons diffuse together under the ambipolar electric field in directions parallel and perpendicular to the static magnetic field, respectively, which is valid if the ends of the magnetic field lines are terminated by insulators [9]. Namely, we assume the flux of ions and electrons is the same. The diffusion coefficient tensor $\mathbf{K}_a$ is given by

$$\mathbf{K}_a = \begin{bmatrix} \gamma^2 D_\perp + \beta^2 D_\parallel & \beta\gamma(D_\perp - D_\parallel) \\ \beta\gamma(D_\perp - D_\parallel) & \beta^2 D_\perp + \gamma^2 D_\parallel \end{bmatrix}, \tag{3.5}$$

$$\beta = B_{0r}/|\mathbf{B}|,$$

$$\gamma = B_{0z}/|\mathbf{B}|,$$

$$D_\parallel = (\mu_i D_e + \mu_e D_i)/(\mu_i + \mu_e),$$

$$D_\perp = D_\parallel/(1 + {\mu_a}^2|\mathbf{B}|^2).$$

As for other species without charge, the density distribution is calculated by the diffusion equation using the diffusion coefficient and generation rate of each species.

We confirmed Eq. (3.5) as the same equation that was described in [8]. Therefore, we adopted the ambipolar diffusion coefficient for use in the present and general models because most of the plasma boundaries in the typical ECR reactor model consist of insulators, including the quartz window and quartz tubes. We assume that the ions and the electrons in the plasma run out to the reactor wall with Bohm velocity [1]. As for the neutral species, we assume that they run out to the reactor wall with thermal velocity. We used the boundary conditions and parameters of the medium as stated above.

An analytical solution for a circular waveguide filled with cold magnetized plasma is provided in [1], in which the dispersion relation and boundary conditions for a waveguide filled with cold magnetized plasma are all derived (see Sections 1.2, 2.2.2,

and 2.4.1). We thus used this dispersion relation to investigate the fundamental microwave propagation characteristics in the plasma chamber.

We used the differential equation solver from COMSOL Multiphysics® [10] to solve Eqs. (3.1), (3.2), and (3.4) above. COMSOL Multiphysics® contains various modules, including a plasma module. We tried to use this plasma module initially, but the results did not agree with our experimental results. Therefore, we did not use the plasma module, but developed the ECR plasma model using the equations presented above.

3.2.3 Experimental method

We measured the ion saturation current distribution on the wafer electrode to confirm the simulated results. The experimental setup is shown schematically in Fig. 3.2 [2]. We used the M-7×2A microwave etching apparatus for 300-mm wafers manufactured by Hitachi Ltd. in 1998 [11]. The configuration of the apparatus is the same as the typical ECR reactor explained in Section 1.3 and Fig. 1.3 (not "NTT system"). We placed 25 planar electrostatic probes within the 300-mm diameter on the wafer electrode to measure the ion saturation current (I_{is}) distribution. A DC voltage bias of -50 V was applied to each probe to repel the electron current and collect the ion current, which was measured using an isolated amplifier.

3.3 Calculation and measurement results

3.3.1 Comparison of simulated and measured results

The static magnetic field distribution in the plasma chamber is illustrated in Fig. 3.3 [2]. The line where $\omega_{ce}/\omega = 1$ is also plotted in the figure, where ω is the angular frequency of the microwaves. We use the divergent magnetic field, i.e., the so-called

magnetic beach condition [4], which includes a surface with magnetic field strength of 0.0875 T ($\omega_{ce}/\omega = 1$) to satisfy the ECR process, where the magnitude is higher in the upper part of the chamber and the ECR region is in an intermediate location that is almost flat in the radial direction. This field configuration is often used in ECR tools to deliver microwave power to the ECR region, even in high density plasmas for which $\omega_{pe}/\omega > 1$, where ω_{pe} is the electron plasma angular frequency, as mentioned previously in Section 1.3.

The measurement results for the I_{is} distribution on the wafer electrode are shown in Fig. 3.4 [2], with an argon pressure in the plasma chamber (P_{Ar}) of 0.4 Pa. This distribution was almost uniform along the azimuthal direction and the measurement data on the four axes are almost identical. Namely, 4 dots corresponding to data on 4 axes in the graph overlap each other. When the microwave power P_{μ} is low (200–500 W), I_{is} is also low and the radial distribution is shown to be nearly uniform, i.e., a slightly peaked profile. We call this the "low mode" [12]. However, when P_{μ} is high (600 W), I_{is} becomes dramatically higher and the distribution changes to convex from a relatively uniform profile. We call this the "high mode."

The simulated results are also plotted in Fig. 3.4 [2] for comparison. We see that the mode transition from low to high mode also occurred in the simulation model. Here, we assume that 30% of the incident microwave power is absorbed by the plasma in the low mode (P_{μ} = 200 - 500 W). In the high mode (P_{μ} = 600 W), we assume that 40% of the incident microwave power is absorbed because of high density plasma localized near the center, whose loss at the wall is expected to reduce. Charles *et al*. measured and estimated power absorption in each part of their ICP tool without static magnetic field, which operated in a capacitive mode [13], and they reported that the power efficiency

was about 20%. The values we use (30% and 40%) are higher than those of their ICP tool and these values are consistent considering that plasma loss is reduced by the static magnetic field. In the low mode, the plasma density on the substrate electrode remained almost constant, however, as P_μ increased, the density also increased gradually.

The results of the simulation show worse uniformity than the experimental ones, especially at $P_\mu = 600$ W, as shown in Fig. 3.4. Needless to say, the calculated, absolute value in our case is much better (agrees well with the experimental one) than using the model [3], where the loss term is underestimated. Figures 3.5 and 3.6 show that a part of the microwave power is absorbed at the upper part of the reactor, whose static magnetic field is strong, such that $\omega_{ce}/\omega > 1$, and the remaining microwave power is absorbed at the lower part of the reactor, whose static magnetic field is weak, such that $\omega_{ce}/\omega < 1$. The power absorption region in the lower part is in the vicinity of the center. It is possible that the effect of the absorption region of the lower part is overestimated in the simulation results. We can simulate hot plasma effect by adjusting collision frequency (see Section 1.2), e.g., by using effective parameter that correctly present hot plasma effect. In this case, almost all the power is absorbed at the upper part and nearly no power absorption occurs in the lower part, and then, the accuracy of the simulation may be improved.

3.3.2 Dependence of plasma distribution on microwave power

The dependences of the plasma distribution and the power absorption on the microwave power are illustrated in Fig. 3.5 [2]. The black and yellow dotted lines indicate the cutoff plasma density n_c of 7.5×10^{16} m^{-3} (corresponding to $\omega_{pe}/\omega = 1$) and the ECR surface field of 0.0875 T (corresponding to $\omega_{ce}/\omega = 1$). When $P_\mu = 200$-500 W (low mode), the maximum plasma density remained almost constant, as mentioned above, and as the

microwave power increased, the plasma volume, where $\omega_{pe}/\omega > 1$, became larger. In the case where P_μ = 600 W (high mode), the plasma density increased dramatically near the center axis and exceeded n_c on the inner window surface. The main plasma absorption region showed a neighboring region where $n_e = n_c$ (on yellow dotted lines) for each P_μ. As P_μ increases, the plasma volume, which has a density that is higher than n_c, also increases.

The microwave electric field distribution for the case of P_μ = 300 W is shown in Fig. 4.3 [2] (in Chapter 4). In this figure, the distributions are shown in the (r, z) plane along with the (r, θ) plane indicated by axial positions of the red dotted lines. The microwave electric fields shown here are represented by the amplitude of their instantaneous values (real part). Note that the field patterns of these figures rotate at a microwave frequency with respect to the center axis because circularly polarized microwaves are introduced. As Kaneko *et al*. [14] noted, the direction of electric field rotation is dependent on the position of the waveguide. On the center axis, the amplitude of the electric field does not change while the direction of the electric field rotates because R waves are introduced. Namely, the electric field on the center axis is circularly polarized perfectly. However, except for the center axis, the amplitude of the electric field changes, and this means that the wave is not perfectly circularly polarized at that point. The wavefront of the electric field pattern is oriented almost perpendicular to the static magnetic field lines and the microwaves propagate along these magnetic field lines (see Fig. 3.3).

The Poynting vector [Re ($\mathbf{E}\times\mathbf{H}^*$)] of the microwaves in the reactor is shown in Fig. 3.6 [2] for the case of P_μ = 300W. The line where $\omega_{pe}/\omega = 1$ is also plotted in the figure. The finite value of the Poynting vector was mainly distributed within the low-

density region, where $\omega_{pe}/\omega < 1$ and corresponds to the power absorption distribution (see Fig. 3.5 [2]). It appears that the microwave power does not enter the high-density region where $n > n_c$ ($\omega_{pe}/\omega > 1$); this will be discussed in Section 3.4.

As can be seen in Figs. 3.5 and 3.6 [2], a plasma volume whose density is $\omega_{pe}/\omega > 1$ increases radially along the ECR surface in the low mode ($P_\mu = 200$ W – 500 W) when microwave power increases because microwave power does not enter the high density region of $\omega_{pe}/\omega > 1$. When the microwave power is 500 W, which is the maximum power in the low mode, the high-density plasma region of $\omega_{pe}/\omega > 1$ cannot increase its volume in radial direction since it reaches to the wall boundary. When a higher microwave power of 600 W is introduced, microwave power absorption inevitably changes, and mode change to the high mode occurs, where the power absorption is under the quartz window, leading to the peaked density profile.

3.4 Discussion

The result, that the microwave power does not enter the high-density region where $n > n_c$ ($\omega_{pe}/\omega > 1$) for the low mode, is important for the discussion of the uniform plasma generation mechanism, as noted in the preceding section. However, this contradicts the propagation characteristics of microwaves in free space without boundaries [15], where the R wave can propagate into a region even at $n > n_c$. To resolve this conflict, we discuss the plasma density dependence of the microwave analysis in a uniform plasma in Section 3.4.1, and perform a theoretical microwave analysis in a circular waveguide filled with cold magnetized plasma in Section 3.4.2. Finally, we present the mechanism for uniform plasma generation in Section 3.4.3.

3.4.1 Microwave propagation in etching reactor

To identify the fundamental characteristics of the microwave distribution in the reactor, we calculate the microwave electric field and the wave absorption under uniform plasma density conditions, as shown in Fig. 3.7 [2]. Here, again, the static magnetic field distribution (see Fig. 3.3 [2]) is considered in the calculations. When the plasma density is low with $\omega_{pe}/\omega < 1$, the electric field in the ECR region is high and the power absorption in the ECR region is dominant. In contrast, when the plasma density is high and $\omega_{pe}/\omega > 1$, the electric field and the absorption pattern become complex and jagged, and the ECR absorption process is no longer dominant. These jagged patterns appear in the high static magnetic field region, where $\omega_{ce}/\omega > 1$. Note that we investigated the jagged patterns and found that these patterns originated from TG waves [16, 17] as explained in Chapter 2.

When the plasma density distribution in the reactor is considered, it is possible that the TG waves become dominant in the high density and high magnetic field region where $\omega_{pe}/\omega > 1$ and $\omega_{ce}/\omega > 1$.

3.4.2 Microwave propagation in circular waveguide filled with a cold magnetized plasma

As mentioned earlier, Figs. 3.5 [2] and 3.6 [2] seem to indicate that the microwave power does not enter the high-density plasma region where $\omega_{pe}/\omega > 1$, while it is well known that, generally, R waves can propagate in high density plasma where $\omega_{pe}/\omega > 1$ if $\omega_{ce}/\omega > 1$ [1, 4, 9, 15]. However, this interpretation is based on wave propagation characteristics in free space with no boundaries. To identify the effects of the reactor walls (finite size), we calculate the propagation characteristics in a circular waveguide filled with a cold magnetized plasma with its static magnetic field oriented

along the waveguide axis. The dispersion relation for a cold uniform plasma in a circular waveguide [1] is

$$\left(\gamma^2 + \kappa_2{}^2 + \gamma k_\perp{}^2\right)\kappa_2 + k_\perp{}^2\left[\kappa_1\left(\gamma + k_\perp{}^2\right) - \kappa_2{}^2\right] = 0, \tag{3.6}$$

where $\gamma = k_z{}^2 - \kappa_1$, $\kappa_1 = \omega^2/c^2\left\{1 - \omega_{pe}{}^2/(\omega^2 - \omega_{ce}{}^2)\right\}$, $\kappa_2 = i\,\omega^2/c^2 \cdot \omega_{pe}{}^2\omega_{ce}/(\omega^2 - \omega_{ce}{}^2)$, $\kappa_3 = \omega^2/c^2\left(1 - \omega_{pe}{}^2\right)$, k_z is the wavenumber with respect to the waveguide axis, c is the speed of light, $k_\perp$ is the wavenumber with respect to the perpendicular direction, and i is the imaginary unit (see Section 1.2 for more detail).

Here, k_z and $k_\perp$ exist together in Eq. (3.6) because of the waveguide boundary. Two solutions for $k_z{}^2$ and $k_\perp{}^2$ can be derived from this equation since it is a quadratic equation involving $k_z{}^2$ and $k_\perp{}^2$. We confirmed that Eq. (3.6) satisfies the general R and L waves when $k_\perp = 0$, meaning an infinite radial boundary, and the general X and O waves when $k_z = 0$. Namely, this means free space conditions without any boundaries.

The two solutions to Eq. (3.6) are represented in Fig. 3.8 [2] by blue and orange lines. Two solutions for $k_\perp = 0$ (equivalent to the R and L waves) are plotted using black dotted lines for comparison. Vertical axis represents the square of the normalized wave number, and the horizontal axis represents $\omega_{pe}{}^2/\omega^2$, which is proportional to the plasma density. When $k_\perp \neq 0$, the dispersion relation changes dramatically at approximately $\omega_{pe}{}^2/\omega^2 = 1$. In the region where the value of vertical axis is negative, waves attenuate and do not propagate. Under a low magnetic field of $\omega_{ce}/\omega = 0.8$ [see Fig. 3.8(a)], the blue line solution that propagates can only exist in the low-density region and meets the cutoff ($k_z = 0$) in the vicinity of $\omega_{pe}{}^2/\omega^2 = 1$. Under a high magnetic field of $\omega_{ce}/\omega = 1.2$ [see Fig. 3.8(b)], the blue line solution shows the transformations from R to L waves in the vicinity

of $\omega_{pe}^2/\omega^2 = 1$ if the plasma density (ω_{pe}^2/ω^2) increases. The orange line solution almost coincides with the L wave in the low-density region and meets the cutoff ($k_z = 0$) in the vicinity of $\omega_{pe}^2/\omega^2 = 1$. With regard to the blue line solution, where $\omega_{pe}^2/\omega^2 < 1$, the wavenumber becomes small and the propagation toward the parallel direction to the static magnetic field is reduced if the plasma density increases to the vicinity of $\omega_{pe}^2/\omega^2 = 1$. As a result of this small wavenumber in the parallel direction, perpendicular propagation is emphasized. It is possible that the reason why microwave power does not enter the high-density region, where $\omega_{pe}^2/\omega^2 > 1$, is a mode transformation from R wave to L wave that occurs in the vicinity of $\omega_{pe}^2/\omega^2 = 1$, because of the presence of the wall boundaries.

3.4.3 Mechanism of uniform plasma generation in ECR plasma etcher

In the ECR reactor, the microwave distribution becomes complex, because the reactor is not large enough when compared with the wavelength, and transition or transformation of the waves can therefore occur, due to the presence of finite boundaries. When the waveguide boundaries (reactor walls) are considered, the propagation characteristics must be modified around $\omega_{pe}/\omega = 1$. The uniform plasma generation mechanism is summarized here as follows.

1) For low microwave power, microwave absorption and plasma generation in the ECR region are dominant when the plasma density is lower than n_c ($\omega_{pe}/\omega < 1$) and plasma is easily generated in the ECR region by the resonance by the R wave normally recognized.

2) For high microwave power, the microwave power is not supplied to the high-density region of $\omega_{pe}/\omega > 1$, and this power is mainly absorbed at the surface of the high-density plasma region where n nearly equals n_c ($\omega_{pe}/\omega = 1$), and at the ECR surface. The reason why no power absorption in the high-density region of $\omega_{pe}/\omega > 1$ relates to the mode

transformation that occurs at around the plasma density corresponding to $\omega_{pe}/\omega = 1$, which emerges when the boundary effect is considered. We will discuss the mode transformation precisely in the next chapter.

3) As the microwave power increases, the plasma density region where $\omega_{pe}/\omega = 1$ is enlarged, because the microwave power is not supplied to the region where $\omega_{pe}/\omega > 1$. As a result of this enlargement, a more uniform plasma can be realized, which is useful for industrial applications.

3.5 Chapter conclusion

We developed a simulation method for ECR etching reactors by combining microwave electromagnetic field analysis with a plasma generation region analysis, and a plasma diffusion analysis. We found consistent solutions to these analyses and confirmed the simulation results by comparing them with experimental results.

Using the simulated results and theoretical considerations, we investigated the uniform plasma generation mechanism, which is crucial for industrial applications. We found that as the microwave power increases, microwave absorption occurs near the surface where $\omega_{pe}/\omega = 1$, and the volume of the high-density plasma, whose density corresponds to $\omega_{pe}/\omega = 1$, increases while the plasma density remains nearly constant. Microwaves do not enter the high-density plasma where $\omega_{pe}/\omega > 1$ and they are absorbed at the surface of the high-density plasma, whose density corresponds to $\omega_{pe}/\omega > 1$. Therefore, the microwave absorption profile generates the uniform plasma. Although we have discussed the mode transformation due to boundary effects, further consideration of the microwave propagation in the reactor is required.

References

[1] D. G. Swanson, Plasma Waves. San Diego, CA, USA, Academic, 1989.

[2] **H. Tamura**, T. Tetsuka, D. Kuwahara, S. Shinohara, "Study on uniform plasma generation mechanism of electron cyclotron resonance etching reactor," IEEE Trans. Plasma Sci., vol. 48, no. 10, pp. 3606-3615, 2020.

[3] Y. Yasaka, A. Fukuyama, A. Hatta, and R. Itatani, "Two–dimensional modeling of electron cyclotron resonance plasma production," J. Appl. Phys., vol. 72, no. 7, pp. 2652–2658, 1992.

[4] T. H. Stix, Waves in Plasmas. New York, NY, USA: Springer, 1992.

[5] G. J. M. Hagelaar and L. C. Pitchford, "Solving the Boltzmann equation to obtain electron transport coefficients and rate coefficients for fluid models," Plasma Sources Sci., Technol. Vol. 14, pp.722-733, 2005.

[6] E. Gogolides and H. H. Sawin, "Continuum modeling of radio-frequency glow discharges. I. Theory and results for electropositive and electronegative gases," J. Appl. Phys., vol. 72, pp.3971-3987, 1992.

[7] E. G. Thorsteinsson and J. T. Gudmundsson, "A global (volume averaged) model of a Cl2/Ar discharge: I. continuous power," J. Phys. D, Appl. Phys., vol. 43, no. 11, Mar. 2010, Art. no. 115201.

[8] Y. Yasaka and N. Uda, "Practical scheme for three-dimensional simulation of electron cyclotron resonance plasma reactors," J. Appl. Phys., vol. 89, no. 7, pp. 3594–3601, 2001.

[9] F. F. Chen, Introduction to Plasma physics. New York, NY, USA: Plenum Press, 1974.

[10] COMSOL Multiphysics® Software. Accessed: 2020. [Online]. Available: https://www.comsol.com/

[11] H. Enami, Y. Ogawa, M. Izawa, and T. Saito, "History and future of Hitachi's plasma etching system," Hitachi Rev., vol. 60, no. 5, pp. 198- 202, Aug. 2011.

[12] D. A. Carl, M. C. Williamson, M. A. Lieberman, and A. J. Lichtenberg, "Axial radio frequency electric field intensity and ion density during low to high mode transition in argon electron cyclotron resonance discharges," J. Vac. Sci. Technol. B, Microelectron., vol. 9, no. 2, pp. 339–347, 1991.

[13] C. Charles, R. W. Boswell, and M. A. Lieberman, "Energy balance in a low pressure capacitive discharge driven by a double-saddle antenna," Phys. Plasmas, vol. 10, no. 3, pp. 891–899, 2003.

[14] T. Kaneko, K. Takahashi, and R. Hatakeyama, "Verification of polarization reversal of electromagnetic waves with electron cyclotron frequency controlling plasma-structure formation," Plasma Fusion Res., vol. 2, 038, 2007.

[15] A. Lieberman and A. J. Lichtenberg, Principals of Plasma Discharges and Materials Processing. New York, NY, USA: Wiley, 1994.

[16] A. W. Trivelpiece and R. W. Gould, "Space charge waves in cylindrical plasma columns," J. Appl. Phys., vol. 30, no. 11, pp. 1784-1793, 1959.

[17] **H. Tamura**, T. Tetsuka, N. Tamari, D. Kuwahara, and S. Shinohara, "Numerical identification of Trivelpiece–Gould waves in an electron cyclotron resonance etching reactor," IEEE Trans. Plasma Sci., vol. 46, no. 10, pp. 3662–3668, 2018.

Table 3.1. Reaction set for Ar discharge, where temperature range $0.01 < T_e < 10$ V [5].

No.	Reaction	Rate coefficient ($m^3 s^{-1}$)
1	$e + Ar \rightarrow Ar^+ + e + e$	$2.39 \times 10^{-14} T_e^{0.57} \exp(-17.43/T_e)$
2	$e + Ar^m \rightarrow Ar^+ + e + e$	$2.71 \times 10^{-13} T_e^{0.26} \exp(-4.59/T_e)$
3	$e + Ar^r \rightarrow Ar^+ + e + e$	$2.70 \times 10^{-13} T_e^{0.29} \exp(-4.24/T_e)$
4	$e + Ar \rightarrow Ar^m + e$	$9.73 \times 10^{-16} T_e^{-0.07} \exp(-11.69/T_e)$
5	$e + Ar \rightarrow Ar^r + e$	$3.93 \times 10^{-15} T_e^{0.46} \exp(-12.09/T_e)$
6	$e + Ar \rightarrow Ar(4p) + e$	$8.91 \times 10^{-15} T_e^{-0.04} \exp(-14.18/T_e)$
7	$e + Ar(4p) \rightarrow Ar^+ + e + e$	$1.09 \times 10^{-12} T_e^{0.29} \exp(-3.42/T_e)$
8	$e + Ar^m \rightarrow Ar(4p) + e$	$2.39 \times 10^{-12} T_e^{-0.15} \exp(-1.82/T_e)$
9	$e + Ar^m \rightarrow Ar^r + e$	3.70×10^{-13}
10	$e + Ar^r \rightarrow Ar^m + e$	9.10×10^{-13}
11	$Ar^m + Ar^m \rightarrow Ar + Ar$	2.00×10^{-13}
12	$Ar^m + Ar^r \rightarrow Ar + Ar^+ + e$	2.10×10^{-15}
13	$Ar(4p) + Ar(4p) \rightarrow Ar + Ar^+ + e$	5.00×10^{-16}
14	$Ar^m + Ar^m \rightarrow Ar + Ar^+ + e$	6.40×10^{-16}
15	$Ar + Ar^m \rightarrow Ar + Ar$	2.10×10^{-21}
16	$Ar^r \rightarrow Ar + \hbar\omega$	$1.00 \times 10^5 s^{-1}$
17	$Ar(4p) \rightarrow Ar + \hbar\omega$	$3.20 \times 10^7 s^{-1}$
18	$Ar(4p) \rightarrow \{ Ar^m, Ar^r \} + \hbar\omega$	$3.00 \times 10^7 s^{-1}$

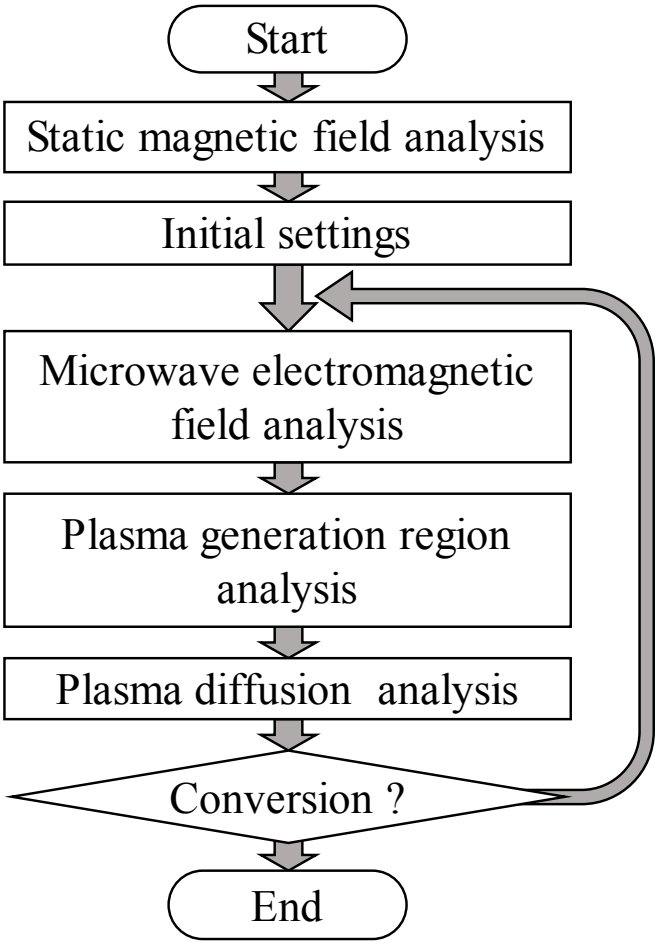

Fig. 3.1. Calculation procedure [2].

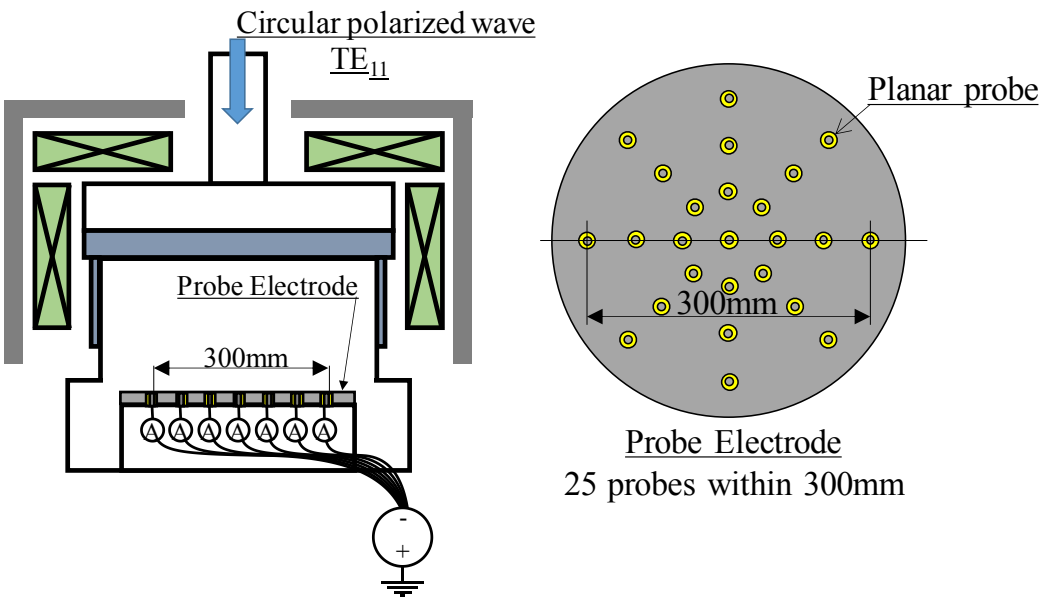

Fig. 3.2. Experimental setup in the ECR reactor [2].

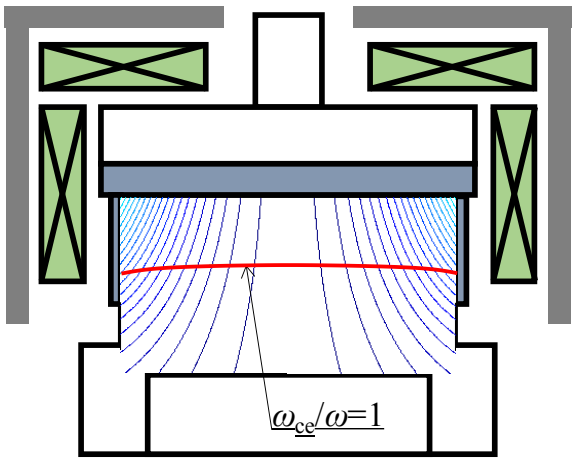

Fig. 3.3. Static magnetic field lines in the reactor [2].

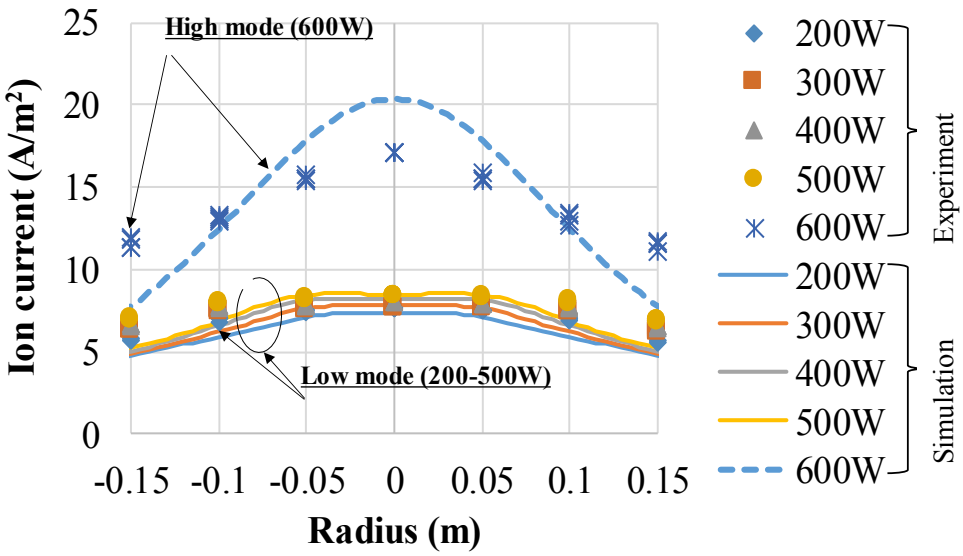

Fig. 3.4. I_{is} on substrate electrode (experimental data and simulated data) in the case where P_{Ar} = 0.4 Pa [2].

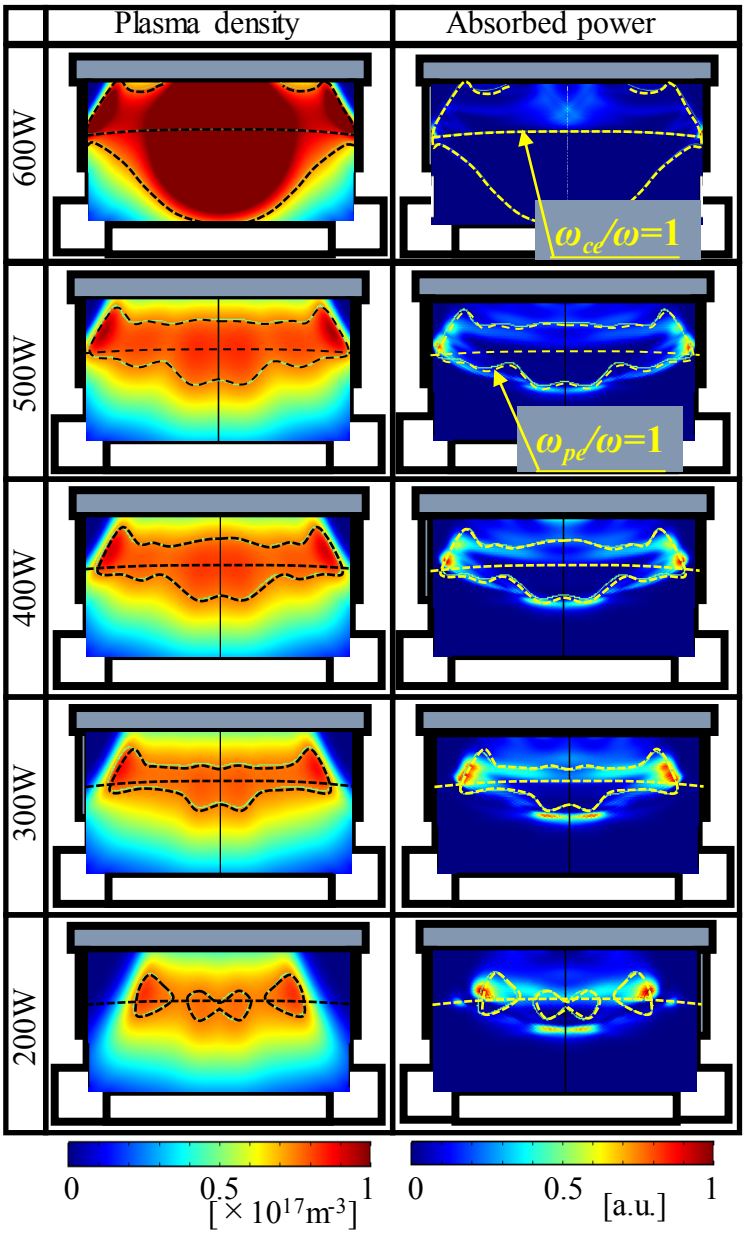

Fig. 3.5. Dependences of the plasma distribution and the microwave power absorption on the microwave power [2]. In the figure, the black and yellow dotted lines indicate a plasma density of 7.5 × 10^{16} m^{-3}, which corresponds to n_c ($\omega_{pe}/\omega = 1$), and the ECR surface corresponds to $\omega_{ce}/\omega = 1$.

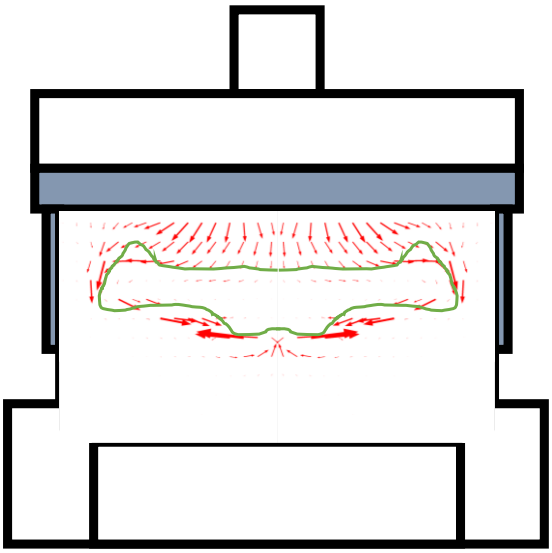

Fig. 3.6. Poynting vector [Re (E×H*)] for P_μ = 300 W and P_{Ar} = 0.4 Pa [2]. The green line indicates the cutoff plasma density n_c.

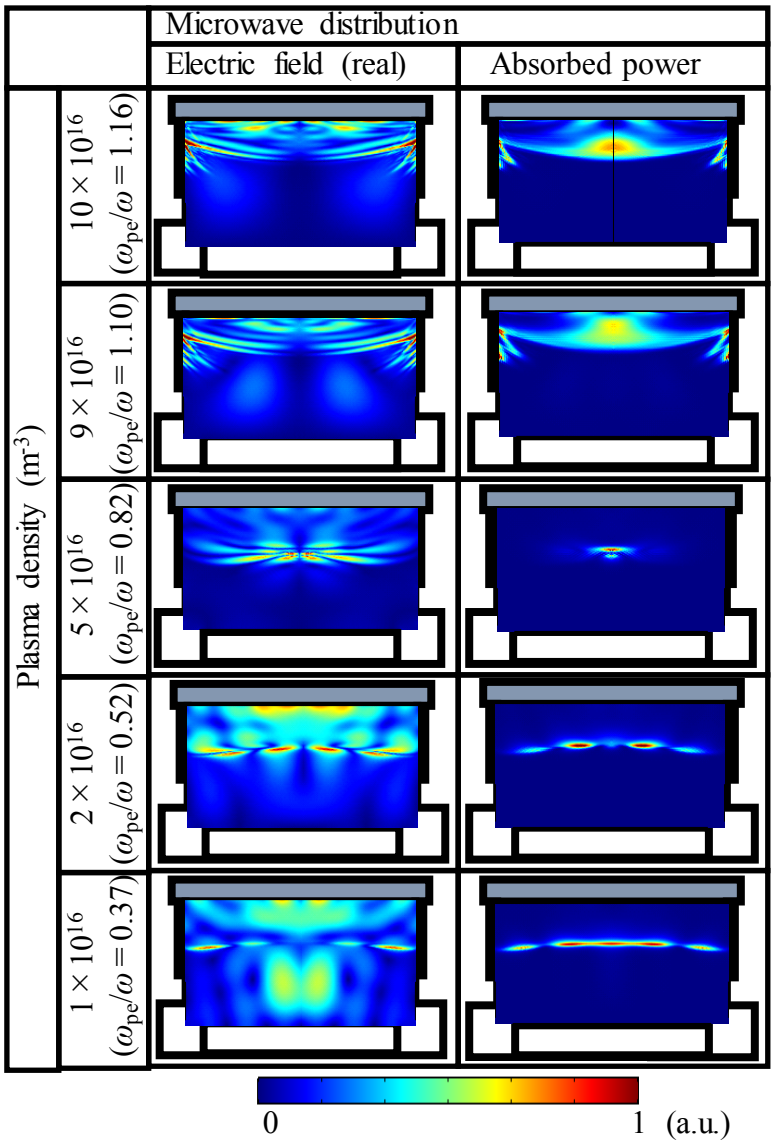

Fig. 3.7. Microwave distribution for uniform plasma density P_{Ar} = 0.4 Pa [2].

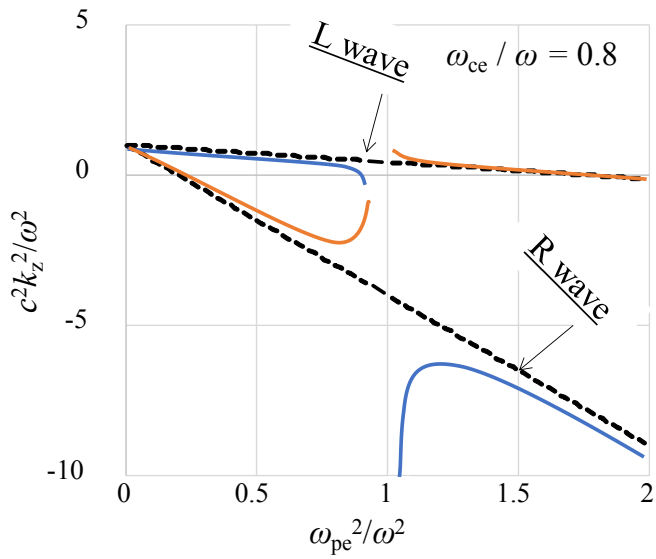

(a) $\omega_{ce}/\omega = 0.8$

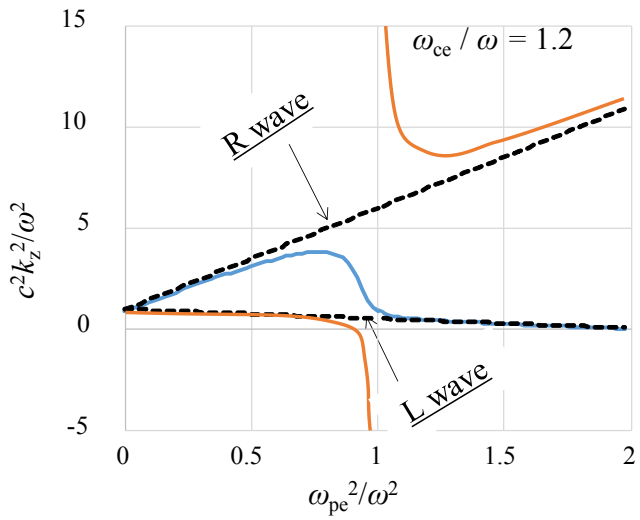

(b) $\omega_{ce}/\omega = 1.2$

Fig. 3.8. Propagation characteristics in circular waveguide filled with magnetized plasma for the case where $k_\perp$ = 16.0 (rad/m) (a) ω_{ce}/ω = 0.8, (b) ω_{ce}/ω = 1.2 [2]. Orange and blue lines indicate two solutions of the dispersion relation, and black dotted lines indicate R and L wave.

Chapter 4

4. Boundary Effect on Mode Transformation in an Electron Cyclotron Resonance Etching Reactor

4.1 Introduction

In Chapter 3, we found that the power of the microwave introduced by R wave does not enter the high density region of ω_{pe}/ω >1 and is absorbed at the surface of ω_{pe}/ω =1, even in strong magnetic fields of ω_{ce}/ω >1, which conflicts with the ordinary propagation characteristics of the theoretical R wave. In addition, this phenomenon is important to generate uniform plasma because the plasma density is saturated at around $\omega_{pe}/\omega = 1$. To solve the seeming contradiction, we investigated the boundary effect of the reactor, and we found that the propagation characteristics must be modified at around the density of $\omega_{pe}/\omega = 1$.

In this chapter, microwave propagation and mode transformation, considering plasma distribution and the effect of the reactor wall, is discussed more precisely by using the simulated results of the electromagnetic field in the ECR reactor and the results of the theoretical analysis of the plasma waveguide with outer vacuum layer, which simulates the plasma distribution in the reactor. Note that, we have already briefly presented the theoretical results of a plasma waveguide loaded with uniform plasma, which has no outer vacuum layer, in Section 3.4.2. Here we present the theoretical formulation and the calculation results of a plasma waveguide with outer vacuum layer, which considers the plasma distribution in the waveguide.

In Section 4.2, we describe the configuration of the typical ECR etching reactor for large diameter wafers of 300 mm as a model, the calculation method of the microwaves in the ECR reactor, and the formulation of the theoretical analysis of the plasma waveguide with outer vacuum layer that simulates the plasma distribution in the ECR reactor. Moreover, we confirm the theoretical characteristics of fundamental waves in magnetized plasma without boundary, to identify the observed waves in the ECR reactor. In Section 4.3, we present the result of the microwave analysis in the ECR reactor and identify the observed waves in the reactor by comparing them with the theoretical fundamental waves, including surface waves. Furthermore, by using the result of the theoretical analysis of the plasma waveguide with outer vacuum layer, the mode transformation characteristics from the introduced R wave into an X wave and the electrostatic Trivelpiece–Gould wave (TG wave), that occurs due to the wall effect, are clarified. Finally, we discuss the microwave propagation characteristics and mode transformation in the reactor, considering the wall effect and plasma distribution. Concluding remarks are presented in Section 4.4.

4.2. Method of investigation

4.2.1 Typical ECR reactor

The typical configuration of an ECR reactor as a 2-D axisymmetric model used in this chapter is the same as the one used in former chapters shown in Fig. 1.3. The reactor was described in detail in Section 1.3. Furthermore, we use the result of the simulation described in Chapter 3.

In the actual apparatus, the reactor is evacuated by a turbomolecular pump. A variable valve is provided between the turbomolecular pump and the reactor, which can

change the exhaust speed. Along with the flow rate of the processing gas, the reactor is controlled by this valve to maintain a predetermined pressure. In the simulation, the pressure in the reactor is constant, and the density of the gas is determined by the pressure. We use argon as the processing gas.

4.2.2 Electromagnetic field in the ECR reactor by simulation

The Calculation procedure is the same as the one described in Chapter 3, shown in Fig. 3.1. See the previous papers [1, 2] and Section 3.3 for further details. The calculation result, that will be used in this chapter, is shown in Fig. 4.1 [3]. The pressure in the reactor is 0.4 Pa, and the microwave power is 300 W. For the microwave analysis, the mode number of the wave field in the azimuthal direction m is 1. Hereinafter, we use these parameters for calculations in the ECR reactor. The plasma density is shown on the left-hand side of the figure and the static magnetic field lines on the right-hand side of the figure. The lines of $\omega_{pe}/\omega = 1$ and $\omega_{ce}/\omega = 1$ are also shown in the figure. As stated before, the line of $\omega_{pe}/\omega = 1$ corresponds to the cutoff density for waves in non-magnetized plasma or for the ordinary wave (O wave) with the static magnetic field. This cutoff density is important because characteristics of the wave propagation drastically change at this density, as mentioned before in Section 3.4 and later in Section 4.3. The line of $\omega_{ce}/\omega = 1$ corresponds to the ECR surface. The plasma is very uniform in the inner region of the line of $\omega_{pe}/\omega = 1$, where the ω_{pe}/ω value slightly exceeds 1, and a steep density gradient and a low-density region can be seen in the outer peripheral region. We simulate this density distribution by a plasma waveguide with outer vacuum region in Section 4.2.3.

The electric field of the microwave in the ECR reactor is calculated by the Helmholtz equation, described in Section 3.2.2 and Eq. (3.1) while considering the

plasma density distribution shown in Fig.4.1 [3]. The magnetic field of the microwave can be calculated by Faraday's law of electromagnetic induction. The power absorption of the microwaves in the reactor can be evaluated by Eq. (4.1) [4].

$$p_{abs} = \frac{1}{4} i\omega\varepsilon_0 \boldsymbol{E}^* \cdot (\boldsymbol{\kappa}^{\boldsymbol{T}} - \boldsymbol{\kappa}) \cdot \boldsymbol{E}, \tag{4.1}$$

where ε_0 is the dielectric constant of vacuum.

4.2.3 Analytical model of plasma waveguide with outer vacuum layer

To identify the propagation characteristics of microwaves in the ECR reactor, we theoretically analyze the plasma waveguide with outer vacuum layer. The model for the theoretical calculation is shown in Fig. 4.2 [3], using the cylindrical coordinate system. A uniform static magnetic field along the z direction is applied. In the circular waveguide, whose radius is b, an inner uniform plasma whose radius is a, is loaded. The outer region of $a < r < b$, that simulates a low-density plasma region in the ECR reactor (see Fig. 4.1), is vacuum, i.e., the plasma density is equal to zero.

The following dispersion relationship is satisfied in the inner plasma region also described in Section 1.2 and Eq. (1.19) [5].

$$\left(\gamma^2 + {\kappa_2}^2 + \gamma {k_\perp}^2\right)\kappa_3 + {k_\perp}^2\left\{\kappa_1\left(\gamma + {k_\perp}^2\right) - {\kappa_2}^2\right\} = 0, \tag{4.2}$$

where $\gamma = {k_z}^2 - \kappa_1$, $\kappa_1 = {k_0}^2\left(1 - \frac{{\omega_{pe}}^2}{\omega^2}\frac{\omega^2}{\omega^2 - {\omega_{ce}}^2}\right)$, $\kappa_2 = {k_0}^2 i \frac{{\omega_{pe}}^2}{\omega^2}\frac{\omega_{ce}}{\omega}\frac{\omega^2}{\omega^2 - {\omega_{ce}}^2}$, $\kappa_3 = {k_0}^2\left(1 - \frac{{\omega_{pe}}^2}{\omega^2}\right)$, k_z is the wavenumber along the z axis, and $k_\perp$ is the wavenumber

perpendicular to the z axis. By solving the dispersion relation of Eq. (4.2), the following two solutions of $k_{\perp 1}$ and $k_{\perp 2}$ corresponding to two modes are obtained.

$$\begin{cases} {k_{\perp 1}}^2 = \frac{-\{(\kappa_3+\kappa_1)\gamma-{\kappa_2}^2\}+\sqrt{\{(\kappa_3+\kappa_1)\gamma-{\kappa_2}^2\}^2-4(\gamma^2+{\kappa_2}^2)\kappa_3\kappa_1}}{2\kappa_1} \\ {k_{\perp 2}}^2 = \frac{-\{(\kappa_3+\kappa_1)\gamma-{\kappa_2}^2\}-\sqrt{\{(\kappa_3+\kappa_1)\gamma-{\kappa_2}^2\}^2-4(\gamma^2+{\kappa_2}^2)\kappa_3\kappa_1}}{2\kappa_1} \end{cases}. \tag{4.3}$$

The electromagnetic field of the inner plasma region is as follows [5].

$$\begin{cases} B_z = A_m J_m(k_{\perp j} r) \\ B_r = iA_m \left\{ k_z \frac{J_m{}'(k_{\perp j} r)}{k_{\perp j}} + \frac{m\kappa_1}{r k_z i\kappa_2} \beta_j \frac{J_m(k_{\perp j} r)}{{k_{\perp j}}^2} \right\} \\ B_\varphi = -A_m \left\{ \frac{\kappa_1}{k_z i\kappa_2} \beta_j \frac{J_m{}'(k_{\perp j} r)}{k_{\perp j}} + \frac{m k_z}{r} \frac{J_m(k_{\perp j} r)}{{k_{\perp j}}^2} \right\} \\ E_z = A_m \frac{i\omega\kappa_1}{k_z i\kappa_2\kappa_3} \beta_j J_m(k_{\perp j} r) \\ E_r = -\omega A_m \left\{ \frac{\delta_j}{i\kappa_2} \frac{J_m{}'(k_{\perp j} r)}{k_{\perp j}} + \frac{m}{r} \frac{J_m(k_{\perp j} r)}{{k_{\perp j}}^2} \right\} \\ E_\varphi = -i\omega A_m \left\{ \frac{J_m{}'(k_{\perp j} r)}{k_{\perp j}} + \frac{m\delta_j}{r i\kappa_2} \frac{J_m(k_{\perp j} r)}{{k_{\perp j}}^2} \right\} \end{cases}, j = 1,2, \tag{4.4}$$

where $\beta_j = \gamma - \frac{{\kappa_2}^2}{\kappa_1} + {k_{\perp j}}^2$, $\delta_j = \gamma + {k_{\perp j}}^2$, and J_m is the m-th order Bessel function of the first kind.

On the other hand, the following dispersion relation is satisfied in the outer vacuum layer [6].

$${k_{\perp out}}^2 + {k_z}^2 = {k_0}^2, \tag{4.5}$$

where $k_{\perp out}$ is the wavenumber perpendicular to the axis in the outer vacuum layer. In the outer vacuum layer, the electromagnetic field can be separated into a transverse electric mode (TE), whose electric field component along the axis E_z is zero, and a transverse magnetic (TM) mode, whose magnetic flux density component along the axis B_z is zero. Here, we consider the TM mode only because the electric field component parallel to the static magnetic field is dominant in the ECR reactor, in the vicinity of the place where the density gradient is steep along the radial direction, as mentioned later in Section 4.3.1. As for the TE mode, its formulation is described in the Appendix.

When $k_{\perp out}^2 > 0$, the electromagnetic field distribution is

$$\begin{cases} B_z = 0 \\ B_r = \frac{{k_0}^2}{\omega {k_{\perp out}}^2} \frac{m}{r} \{A_{1E} J_m(k_{\perp out} r) + A_{2E} N_m(k_{\perp out} r)\} \\ B_\varphi = \frac{i{k_0}^2}{\omega k_{\perp out}} \{A_{1E} {J_m}'(k_{\perp out} r) + A_{2E} {N_m}'(k_{\perp out} r)\} \\ E_z = A_{1E} J_m(k_{\perp out} r) + A_{2E} N_m(k_{\perp out} r) \\ E_r = \frac{ik_z}{k_{\perp out}} \{A_{1E} {J_m}'(k_{\perp out} r) + A_{2E} {N_m}'(k_{\perp out} r)\} \\ E_\varphi = -\frac{k_z}{{k_{\perp out}}^2} \frac{m}{r} \{A_{1E} J_m(k_{\perp out} r) + A_{2E} N_m(k_{\perp out} r)\} \end{cases}, \tag{4.6}$$

where N_m is the m-th order Bessel function of the second kind [6]. When $k_{\perp out}^2 < 0$, the electromagnetic field distribution is

$$
\begin{cases}
B_z = 0 \\
B_r = \frac{{k_0}^2}{\omega {k_{\perp out}}^2}\frac{m}{r}\left\{A_{1E} I_m\left(\frac{k_{\perp out}}{i} r\right) + A_{2E} K_m\left(\frac{k_{\perp out}}{i} r\right)\right\} \\
B_\varphi = \frac{{k_0}^2}{\omega k_{\perp out}}\left\{A_{1E} {I_m}'\left(\frac{k_{\perp out}}{i} r\right) + A_{2E} {K_m}'\left(\frac{k_{\perp out}}{i} r\right)\right\} \\
E_z = A_{1E} I_m\left(\frac{k_{\perp out}}{i} r\right) + A_{2E} K_m\left(\frac{k_{\perp out}}{i} r\right) \\
E_r = \frac{k_z}{k_{\perp out}}\left\{A_{1E} {I_m}'\left(\frac{k_{\perp out}}{i} r\right) + A_{2E} {K_m}'\left(\frac{k_{\perp out}}{i} r\right)\right\} \\
E_\varphi = -\frac{k_z}{{k_{\perp out}}^2}\frac{m}{r}\left\{A_{1E} I_m\left(\frac{k_{\perp out}}{i} r\right) + A_{2E} K_m\left(\frac{k_{\perp out}}{i} r\right)\right\}
\end{cases}, \tag{4.7}
$$

where I_m is the m-th order modified Bessel function of the first kind, and K_m is the m-th order modified Bessel function of the second kind [6].

Now, we consider the boundary conditions to connect the solutions of the inner plasma and the outer vacuum regions, where the tangential electric field (E_z and E_φ) is continuous on the plasma-vacuum interface ($r = a$). Moreover, at the vacuum-waveguide interface ($r = b$), we apply the boundary condition that the tangential electric field is zero. When $k_{\perp out}^2 > 0$, the boundary condition is as follows:

$$
\begin{cases}
A_m \frac{i\omega\kappa_1}{k_z i\kappa_2\kappa_3}\beta_j J_m(k_{\perp j} a) = A_{1E} J_m(k_{\perp out} a) + A_{2E} N_m(k_{\perp out} a) \\
-i\omega A_m\left\{\frac{{J_m}'(k_{\perp j} a)}{k_{\perp j}} + \frac{m\delta_j}{ai\kappa_2}\frac{J_m(k_{\perp j} a)}{{k_{\perp j}}^2}\right\} = -\frac{k_z}{{k_{\perp out}}^2}\frac{m}{a}\{A_{1E} J_m(k_{\perp out} a) + A_{2E} N_m(k_{\perp out} a)\}, \\
A_{1E} J_m(k_{\perp out} b) + A_{2E} N_m(k_{\perp out} b) = 0
\end{cases}
$$

$j = 1, 2.$ (4.8)

When $k_{\perp out}^2 < 0$,

$$\begin{cases} A_m \frac{i\omega\kappa_1}{k_z i\kappa_2\kappa_3}\beta_j J_m(k_{\perp j}a) = A_{1E} I_m\left(\frac{k_{\perp out}}{i}a\right) + A_{2E} K_m\left(\frac{k_{\perp out}}{i}a\right) \\ -i\omega A_m \left\{\frac{J_m{}'(k_{\perp j}a)}{k_{\perp j}} + \frac{m\delta_j}{ai\kappa_2}\frac{J_m(k_{\perp j}a)}{{k_{\perp j}}^2}\right\} = -\frac{k_z}{{k_{\perp out}}^2}\frac{m}{a}\left\{A_{1E} I_m\left(\frac{k_{\perp out}}{i}a\right) + A_{2E} K_m\left(\frac{k_{\perp out}}{i}a\right)\right\}, \\ A_{1E} J_m(k_{\perp out}b) + A_{2E} N_m(k_{\perp out}b) = 0 \end{cases}$$

$j = 1, 2.$ (4.9)

There are three indeterminate coefficients in Eqs. (4.4), (4.6), and (4.7) of A_m, A_{1E}, A_{2E}. They can be successfully eliminated by using the boundary conditions of Eq. (4.8) for $k_{\perp out}^2 > 0$ or Eq. (4.9) for $k_{\perp out}^2 < 0$, since there are the same number of boundary equations. Next, the wavenumber along the z axis k_z can be derived theoretically by using the dispersion relations of Eqs. (4.2) and (4.5).

4.2.4 Fundamental waves in plasma without boundary

It is well known that there are four kinds of fundamental electromagnetic waves in magnetized plasma without boundary. They are the right-hand polarized wave (R wave), the left-hand polarized wave (L wave), the extraordinary wave (X wave), and the ordinary wave (O wave). R and L waves propagate along the direction of a static magnetic field, and X and O waves propagate along the direction that is perpendicular to the static magnetic field. Theoretical wavenumbers of these fundamental waves are as follows, in the microwave range [7].

$$\text{R wave: } \frac{{k_\mathrm{R}}^2}{{k_0}^2} = 1 - \frac{{\omega_\mathrm{pe}}^2}{\omega^2}\frac{\omega}{\omega - \omega_\mathrm{ce}}, \tag{4.12}$$

$$\text{L wave: } \frac{{k_\mathrm{L}}^2}{{k_0}^2} = 1 - \frac{{\omega_\mathrm{pe}}^2}{\omega^2}\frac{\omega}{\omega + \omega_\mathrm{ce}}, \tag{4.13}$$

$$\text{X wave: } \frac{{k_\mathrm{X}}^2}{{k_0}^2} = 1 - \frac{{\omega_\mathrm{pe}}^2}{\omega^2}\frac{\omega^2 - {\omega_\mathrm{pe}}^2}{\omega^2 - {\omega_\mathrm{pe}}^2 - {\omega_\mathrm{ce}}^2}, \tag{4.14}$$

$$\text{O wave: } \frac{{k_\mathrm{O}}^2}{{k_0}^2} = 1 - \frac{{\omega_\mathrm{pe}}^2}{\omega^2}, \tag{4.15}$$

where k_R, k_L, k_X, and k_O are the theoretical wavenumbers of the R, L, X, and O waves, respectively. See Section 1.2 for details. These equations are used to identify the observed waves in the ECR reactor, as described in Section 4.3.2. Note that for an arbitrary propagation angle, wave characteristics become complex, because the behaviors of these waves are mixed (see the CMA diagram in Fig. 1.1).

A wave whose wavenumber is k_z that propagates along the z axis, can be represented as

$$A \exp(ik_z z) = |A| \exp(i\theta_0 + i\theta), \tag{4.16}$$

where A=$|A|\exp(i\theta_0)$ is the amplitude of the wave, θ is the phase angle of the wave, and θ_0 is the initial phase at $z = 0$. As mentioned later in Section 4.3.1, some of the above four waves are observed in the ECR reactor, and the phase angle of the waves can be evaluated by electric or magnetic field components. We compare the phase angle of the observed waves in the ECR reactor with that of the fundamental waves calculated by the theoretical wavenumber to identify the observed waves.

4.3. Results and discussion

4.3.1 Simulated results of electromagnetic field

Figure 4.3 [3] shows the absolute values of an instantaneous electric field distribution in the (r, z) plane along with the (r, θ) plane, indicated by the axial positions of the red dotted lines in the figure. Since a circularly polarized microwave is introduced, the patterns rotate at the frequency of the microwave with respect to the central axis. This

ensures the uniformity of plasma parameters such as the electron density along the azimuthal direction. It is confirmed that the electric field pattern in the circular waveguide represents the TE_{11} mode, because the waveguide radius is small and only the lowest mode of TE_{11} can propagate. The electric field near the center axis is stronger in the upper region from the quartz window without plasma. On the other hand, the electric field tends to be weaker in the vicinity of the center axis of the reactor with plasma.

We investigate the distribution of electromagnetic field in the ECR reactor in detail. As shown later in this section, various waves can be seen in a part of the region in the ECR reactor. To characterize miscellaneous wave characteristics, we separate four spatial regions: Figure 4.4 [1] shows the four regions of (1) Reg01: low-density ($\omega_{pe}/\omega < 1$) and strong magnetic field ($\omega_{ce}/\omega > 1$), (2) Reg02: high-density ($\omega_{pe}/\omega > 1$) and strong magnetic field ($\omega_{ce}/\omega > 1$), (3) Reg03: high-density ($\omega_{pe}/\omega > 1$) and weak magnetic field ($\omega_{ce}/\omega < 1$), and (4) Reg04: low-density ($\omega_{pe}/\omega < 1$) and weak magnetic field ($\omega_{ce}/\omega < 1$).

We calculate the power absorption ratio in each region. They are (1) Reg01: 31%, (2) Reg02: 47%, (3) Reg03: 9%, and (4) Reg04: 13%. In the strong magnetic field region of Reg01 and Reg02, most of microwave power (78%) is absorbed, therefore these regions are important.

Figures 4.5 [3] and 4.6 [3] show the instantaneous electric and magnetic field distributions in terms of absolute value ($|\boldsymbol{E}|$, $|\boldsymbol{H}|$), parallel component to the static magnetic field ($E_{//}$, $H_{//}$), left-hand polarized component (E_L, H_L), and right-hand polarized component (E_R, H_R) for the phase angle of 0 radian [(a), (b)] and $\pi/2$ radian [(c), (d)]. Lines of $\omega_{pe}/\omega = 1$ and $\omega_{ce}/\omega = 1$ are also shown in the figures. When the phase angle is increased by π, the value of the electromagnetic field of the microwave is reversed. In other words, the phase angle of 0 radian or $\pi/2$ radian corresponds to the real part or the

imaginary part of the electromagnetic field, respectively. By the phase change, we can distinguish the propagating waves with direction and standing waves.

In this simulation, the cold plasma approximation is used, but in ECR plasma that operates at low pressure, it is possible that treating it as a hot plasma is effective to improve the accuracy [8] (see Section 1.2). By using the hot plasma approximation, it is expected that the loss of microwave power is large in the strong magnetic field region compared with cold plasma, and power absorption in the strong magnetic field region is important. However, there is not an appreciable change of wave phenomena between the cold plasma with electron collisions and the hot plasma [4]. Therefore, we focus on the upper part of the reactor, whose static magnetic field is strong ($\omega_{ce}/\omega > 1$), as follows.

(1) Reg01: The region of $\omega_{pe}/\omega < 1$ and $\omega_{ce}/\omega > 1$

As for the region of the upper part of the reactor below the quartz plate, where $\omega_{pe}/\omega < 1$ and $\omega_{ce}/\omega > 1$, the field components of E_R and H_R whose electric and magnetic fields are right-hand polarized, are dominant. This is natural, because a right-hand polarized microwave is introduced. The electromagnetic waves, seen with the E_R and the H_R components, propagate parallel to the static magnetic field, and there is a possibility of dominant R wave propagation. As mentioned later in Section 4.3.2, this wave is identified as the R wave by comparing the phase angle of the wave with the theoretical R wave.

Moreover, a localized wave on the interface of the quartz plate and the plasma surface is observed in the $H_{//}$ and the E_L components. This wave hardly moves and is almost a standing wave along the interface. It attenuates along the static magnetic field line, which is almost perpendicular to the interface of the quartz window and the plasma, and the skin depth of the $H_{//}$ component is approximately 0.014 m. Therefore, the wave

represents a surface wave whose wavelength along the interface is almost the same as the one in the quartz window (see Fig. 4.3).

As for the calculated magnetic field component H_z along the z axis in the quartz window, we identified that it closely represents the TE_{17} mode of circular waveguide. We theoretically studied a circular waveguide filled with uniform plasma with a static magnetic field along the axis, and the mode of the waveguide corresponding to the TE_{17} mode, which is cutoff and exponentially attenuates along the axis, was calculated. As a result, we identified that the skin depth of 14.7 mm along the axis of the mode is almost the same as the one observed in the reactor (14.8 mm).

(2) Reg02: The region of $\omega_{pe}/\omega > 1$ and $\omega_{ce}/\omega > 1$

In this region, the $E_{//}$ component, that is parallel to the static magnetic field, and the H_R component, that is right-hand polarized, are dominant. This wave propagates along the static magnetic field, and the direction of the electric field is almost the same as the direction of propagation. Therefore, we conclude that this wave is the electrostatic wave. The wavelength of the electrostatic wave becomes short in the vicinity of $\omega_{pe}/\omega = 1$ and $\omega_{ce}/\omega = 1$. It can be concluded that this electrostatic wave represents the TG wave [9], based on the analyzed result described in Chapter 1 and the consistency of the existence region of $\omega_{pe}/\omega > 1$ and $\omega_{ce}/\omega > 1$ [2]. In addition, waves that propagate perpendicular to the static magnetic field from the peripheral region toward the center can be seen in the E_L and the $H_{//}$ components. There is a possibility that this wave is the X wave, considering the propagation direction and the electromagnetic field, and it can actually be identified as the X wave by comparing it with the theoretical phase angle, as described later in Section 4.3.2.

As for the Reg03, and Reg04, we do not treat these regions because of their lower relative importance as compared to Reg01 and Reg02, based on the discussion in this section.

From the above results, the microwave that is introduced from the upper part of the reactor by right-hand polarized wave is divided into the R wave and the surface wave, localized at the plasma–quartz interface, and the R wave is transformed to the X wave and the electrostatic wave of the TG wave in the vicinity of $\omega_{pe}/\omega = 1$. In the next section, we will describe the mode transformed X and the TG waves by the effect of the radial boundary in more detail.

Figure 4.7 [1] shows the distribution of power absorption and the instantaneous electric field vector in the ECR reactor. The power absorption is shown on the left side of the figure, and the electric field vector is shown on the right side of the figure by arrows, together with the plasma density distribution. An enlarged view of the electric field vector in the vicinity of the region of the steep density gradient along the perpendicular direction to the static magnetic field is also shown in the figure. As shown, the electric field parallel to the static magnetic field $E_{//}$ is dominant in the region of $\omega_{pe}/\omega > 1$ (inside of the line of $\omega_{pe}/\omega = 1$), and a wave that is attenuated along the perpendicular direction to the static magnetic field can be seen in the region of the steep density gradient. The wavelength is short, and the electric field is large in the region around the steep density gradient. As a result, a large power absorption is observed in this region. Since the electrostatic wave of the TG wave is dominant in Reg02 ($\omega_{pe}/\omega > 1$ and $\omega_{ce}/\omega > 1$), power absorption of the TG wave is important.

4.3.2 Comparison between waves in reactor and fundamental theoretical waves

At the upper part of the reactor where $\omega_{ce}/\omega > 1$, waves that propagate along static magnetic field are observed with the E_R component, as mentioned in Section 4.3.1. We compare the phase angle of the simulated wave with the theoretical fundamental wave to identify the type of the wave. Figure 4.8 [3] shows the comparison the phase angle of the E_R component with the theoretical R wave on the static magnetic field line.

Figure 4.8(a) shows the coordinates along a magnetic field line plotted by a red dotted line. The origin of the coordinates is the interface of the quartz plate and the plasma surface. Figure 4.8(b) shows the E_R component on the coordinates shown in Fig. 4.8(a). The horizontal axis represents the distance along the coordinates from the origin. The position of the $\omega_{pe}/\omega = 1$ and $\omega_{ce}/\omega = 1$ is also shown in the figure. The E_R component is attenuated while propagating along the static magnetic field line and becomes very small in the vicinity of the ECR surface of $\omega_{ce}/\omega = 1$. Figure 4.8(c) shows the result of the phase comparison of the E_R component with the theoretical R wave. The initial phase of the theoretical R wave is adjusted to that of the E_R component. The phase angle of the theoretical R wave is calculated by Eqs. (4.12) and (4.16) using the values of ω_{pe}/ω and ω_{ce}/ω at each position of the coordinates shown in Fig. 4.8(a). The phase angle of the theoretical R wave changes drastically as the position becomes closer to the ECR surface of $\omega_{ce}/\omega = 1$, because the wavelength becomes short. The phase angle of the E_R component corresponds to the theoretical R wave, when the distance to the quartz window is small. The E_R component can be identified as the theoretical R wave, because of the consistency of phase angle, electric field direction, and propagation direction. The phase deviation between the E_R component and the theoretical R wave increases as the location

is close to the position of $\omega_{pe}/\omega = 1$. The cause of the deviation is the mode transformation to the X wave by the radial boundary effect, which will be discussed later in Section 4.3.3.

Next, waves that propagate along the perpendicular direction to the static magnetic field were observed in the ECR reactor, as mentioned in Section 4.3.1. We compare the phase angle of the observed wave with the theoretical X wave in a similar procedure in Fig. 4.9 [3]. Figure 4.9(a) shows the coordinates on a flow line, that is perpendicular to the static magnetic field, plotted by a red dotted line. The origin of these coordinates is on the center axis. Figure 4.9(b) shows the $H_{//}$ component on the coordinates shown in Fig. 4.9(a) together with the theoretical X wave. The amplitude and the initial phase of the theoretical X wave are adjusted to match the $H_{//}$ component. Figure 4.9(c) shows the result of phase comparison with the theoretical X wave. The initial phase of the theoretical X wave is adjusted to match the phase angle. Excluding the region around the center, the $H_{//}$ component in the ECR reactor matches the theoretical X wave by according to comparison of the phase angle and the distribution. Therefore, the wave shown in the $H_{//}$ component in the intermediate region is identified as the theoretical X wave.

4.3.3 Theoretical results of plasma waveguide with outer vacuum layer

R wave and X waves are identified in the ECR reactor, mainly in the Reg01 and Reg02, respectively, as mentioned in Section 4.3.2. In this section, wave propagation characteristics are theoretically calculated, considering plasma distribution and the wall effect. Furthermore, relations between the waves in the ECR reactor will be discussed later in Section 4.3.4.

Figure 4.10 [3] shows the theoretical wavenumber of plasma waveguide with outer vacuum layer in the case of a strong magnetic field of $\omega_{ce}/\omega = 1.1$. There are two solutions for $j = 1$ and $j = 2$, that can be derived from the dispersion relation of Eq. (4.3) for the inner plasma region. Figure 4.10(a) shows the mode corresponding to the solution of $j = 1$, and Fig. 4.10(b) shows the solution of $j = 2$. The vertical axis of each graph is the square of normalized total wave number $(k_z^2+k_\perp^2)/k_0^2$ in logarithmic scale, and the horizontal axis is ω_{pe}^2/ω^2, that is proportional to the plasma density of the inner plasma region. We used the parameters of plasma radius $a = 0.2$ m, waveguide radius $b = 0.25$ m, and $m = 1$. Fundamental modes of the R, L, X, and O waves are plotted in each figure by solid lines for comparison. The many point rows, each of which corresponds to the results of a separate propagation modes, can be seen, because the waveguide radius is large compared with the wavelength.

When the static magnetic field is as strong as $\omega_{ce}/\omega = 1.1$, the mode of $j = 1$ [Fig. 4.10(a)] corresponds to a small wavenumber or long wavelength mode, and the mode of j=2 [Fig. 4.10(b)] corresponds to a large wavenumber or short wavelength mode. As for the mode corresponding to $j = 1$ [Fig. 4.10(a)], the point rows are in the vicinity of the L wave and O wave lines. It shows that the mode transformation from L wave to O wave and vice versa can occur when the plasma density changes. As for the mode corresponding to $j = 2$ [Fig. 4.10(b)], when the plasma density is as low as $\omega_{pe}^2/\omega^2 < 1$, the point rows are placed between the lines of the R wave and X wave, and as the plasma density increases, the point rows move from R wave vicinity to X wave vicinity. It also shows that the mode transformation from R wave, originally introduced from the waveguide, to X wave can occur by the effect of the waveguide boundary. When the plasma density exceeds $\omega_{pe}^2/\omega^2 = 1$, the point rows are divided into the X wave vicinity

and upper region of the R wave. At the upper region of the R wave, in the vicinity of $\omega_{pe}^2/\omega^2 = 1$, the wave represents the electrostatic wave of the TG wave, as shown later in Fig. 4.12 [3].

In Section 4.3.2, we compared the phase angle of the wave in the ECR reactor with that of the R wave, and the deviation became large as the propagation distance increases and the position of $\omega_{pe}/\omega = 1$ becomes closer. In Fig. 4.10(b), the deviation between R wave and theoretical value becomes large as ω_{pe}^2/ω^2 approaches $\omega_{pe}^2/\omega^2 = 1$ in each point row in the low-density region of $\omega_{pe}^2/\omega^2 < 1$. This tendency of the deviation is consistent with each other. The cause of the phase deviation in the ECR reactor might be the dependence on the density, proportional to ω_{pe}^2/ω^2.

Figure 4.11 [3] shows plots of the theoretical wavenumber of the plasma waveguide with outer vacuum layer, whose horizontal axis is ω_{ce}/ω, that is proportional to the static magnetic field. Figures 4.11(a) and (b) show the low-density case of $\omega_{pe}/\omega = 0.95$, and Figs. 4.11(c) and (d) show the high-density case of $\omega_{pe}/\omega = 1.05$. The vertical axis of each graph is the square of the normalized wavenumber, that is the same as in Fig. 4.10, and the parameters are also the same. The wavenumber of the plasma waveguide with outer vacuum layer drastically changes before and after $\omega_{ce}/\omega = 1$, and it becomes very large at around $\omega_{ce}/\omega = 1$ in Figs. 4.11(b) and (d), which shows the ECR phenomenon. When ω_{pe}/ω and ω_{ce}/ω approach to 1 in the region of $\omega_{pe}/\omega > 1$ and $\omega_{ce}/\omega > 1$, the total wavenumber becomes very large, as can be seen in Figs. 4.10(b) and 4.11(d).

As mentioned previously in Section 4.3.1, it is observed that the electrostatic wave of the $E_{//}$ component is dominant in the region of $\omega_{pe}/\omega > 1$ and $\omega_{ce}/\omega > 1$ in the reactor. Figure 4.12 [3] shows the example of an instantaneous electric field and power absorption distribution of a plasma waveguide with outer vacuum layer for the case of

$\omega_{pe}/\omega > 1$ and $\omega_{ce}/\omega > 1$ in the plasma region. We use the parameters of plasma radius a = 0.2 m, waveguide radius b = 0.25 m, ω_{pe}/ω = 1.02, ω_{ce}/ω = 1.1, m = 1, and the propagation mode of j = 2. In the plasma layer of $r < a$ (0.2 m), the z component of the electric field is dominant. Therefore, the wave is the electrostatic wave, because the wavenumber is parallel to the electric field, and the electric field pattern is similar to the pattern in the ECR reactor shown in Fig. 4.7. The r component of the electric field E_r is localized at the plasma surface only.

4.3.4 Discussion

Uniform plasma generation is very important for semiconductor manufacturing tools of large diameter substrates utilizing plasma. To generate uniform plasma on the substrates, plasma generation region must be controlled to be ring-shaped, considering the diffusion process. In the ECR reactor, the ring-shaped power absorption, which results in a similar plasma generation, is observed in the vicinity of the steep density gradient (see Fig. 4.7).

In order to understand the observed phenomena by investigating wave characteristics, we identified that the R wave transforms into the X wave and electrostatic wave of the TG wave by theoretical analysis, when plasma density increases and exceeds ω_{pe}/ω = 1 in the strong magnetic field region of $\omega_{ce}/\omega > 1$. We also found, that the wavenumber became large in the vicinity of $\omega_{pe}^2/\omega^2 = 1$, from $\omega_{ce}/\omega = 1$ by the result of theoretical analysis of the plasma waveguide with outer vacuum layer (see Figs. 4.10 and 4.11). We have shown that the mode transformation also occurs in the ECR reactor, because of the existence of the R wave, the X wave, and the TG wave.

In the traditional concept of the ECR plasma source mentioned in Chapter 1, the R wave delivers the microwave power to the ECR surface directly, and high-density plasma of $\omega_{pe}/\omega > 1$ can be generated. However, by considering the boundary effect, we found, that the R waves do not enter high-density plasma of $\omega_{pe}/\omega > 1$, from the mode transformation phenomena and the power absorption that occurs in the peripheral region, where a steep density gradient is observed. Therefore, this is an effective mechanism to generate ring-shaped power absorption, leading to the uniform plasma profile by combining its effect with that of the diffusion, where the main central (edge) region has the lower (higher) diffusivity. Note that for higher microwave power, the density shows a peaked radial profile due to the strong power absorption underneath the quartz glass window (see Fig. 3.5) [1]. Extension of the present analysis can reveal the conditions for lower or higher microwave power than the present one with good uniform density profile, this will be discussed in a separate paper.

4.4. Chapter conclusions

The microwave electromagnetic field in the ECR reactor was investigated for the purpose of clarifying the mechanism of uniform plasma generation. We used the simulation results of the plasma distribution, and a theoretical analysis of the plasma waveguide with outer vacuum layer was performed, while considering the wall effect. As a result, we identified that the extraordinary wave (X wave) and electrostatic wave of the TG wave existed in the reactor by comparing our results with the theoretical wavenumber, in addition to the right-hand polarized wave (R wave), which is introduced to the waveguide. Moreover, the excited surface wave, located at the interface of the quartz window and the plasma, was observed.

We clarified the generation of the above waves: the introduced R wave is transformed to the X wave and the TG wave in the vicinity of the plasma density $\omega_{pe}/\omega = 1$ due to the radial boundary effect. By considering the mode transformation in the ECR reactor, we found that a ring-shaped power absorption, that is essential to generate uniform plasma, is realized.

References

[1] **H. Tamura**, T. Tetsuka, D. Kuwahara, S. Shinohara, "Study on uniform plasma generation mechanism of electron cyclotron resonance etching reactor," IEEE Trans. Plasma Sci., vol. 48, no. 10, pp. 3606-3615, 2020.

[2] **H. Tamura**, T. Tetsuka, N. Tamari, D. Kuwahara, and S. Shinohara, "Numerical identification of Trivelpiece–Gould waves in an electron cyclotron resonance etching reactor," IEEE Trans. Plasma Sci., vol. 46, no. 10, pp. 3662–3668, 2018.

[3] **H. Tamura**, T. Tetsuka, T. Sekine, and S. Shinohara, "Boundary effect on mode transformation in an electron cyclotron resonance etching reactor," Jpn. J. Appl. Phys., accepted.

[4] T. H. Stix, Waves in Plasmas. New York, NY, USA: Springer, 1992.

[5] D. G. Swanson, Plasma Waves. San Diego, CA, USA, Academic, 1989.

[6] R. E. Collin, Field Theory of Guided Waves, Wiley-IEEE Press, 1990.

[7] F. F. Chen, Introduction to Plasma physics. New York, NY, USA: Plenum Press, 1974.

[8] Y. Yasaka, A. Fukuyama, A. Hatta, and R. Itatani, "Two–dimensional modeling of electron cyclotron resonance plasma production," J. Appl. Phys., vol. 72, no. 7, pp. 2652–2658, 1992.

[9] A. W. Trivelpiece and R. W. Gould, “Space charge waves in cylindrical plasma columns,” J. Appl. Phys., vol. 30, no. 11, pp. 1784-1793, 1959.

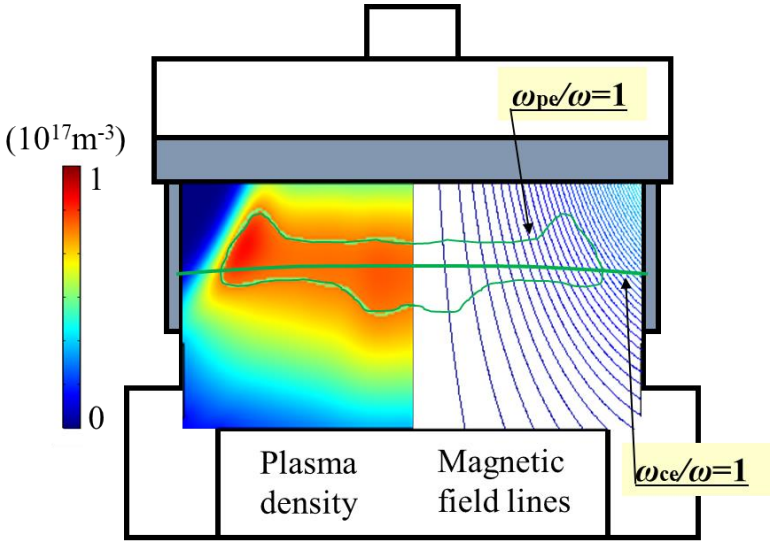

Fig. 4.1. Distributions of plasma density and static magnetic field line in the ECR reactor [1].

Pressure is 0.4 Pa, microwave power is 300 W, processing gas is argon, and the azimuthal mode number m = 1 regarding the electromagnetic fields by injecting the microwave.

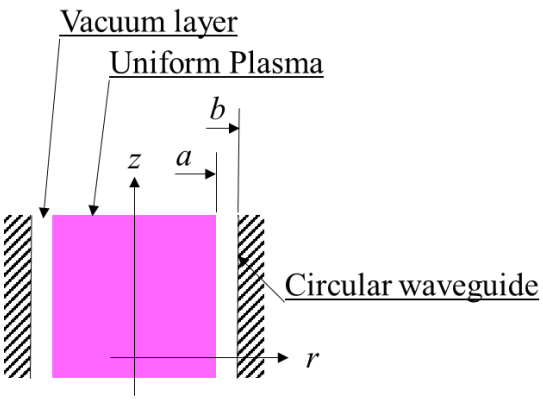

Fig. 4.2. Theoretical model of plasma waveguide with outer vacuum layer [1].

Uniform static magnetic field along the z axis: B_{0z}.

Waveguide radius: b.

Inner uniform plasma at $r < a$.

Outer vacuum layer at $a < r < b$.

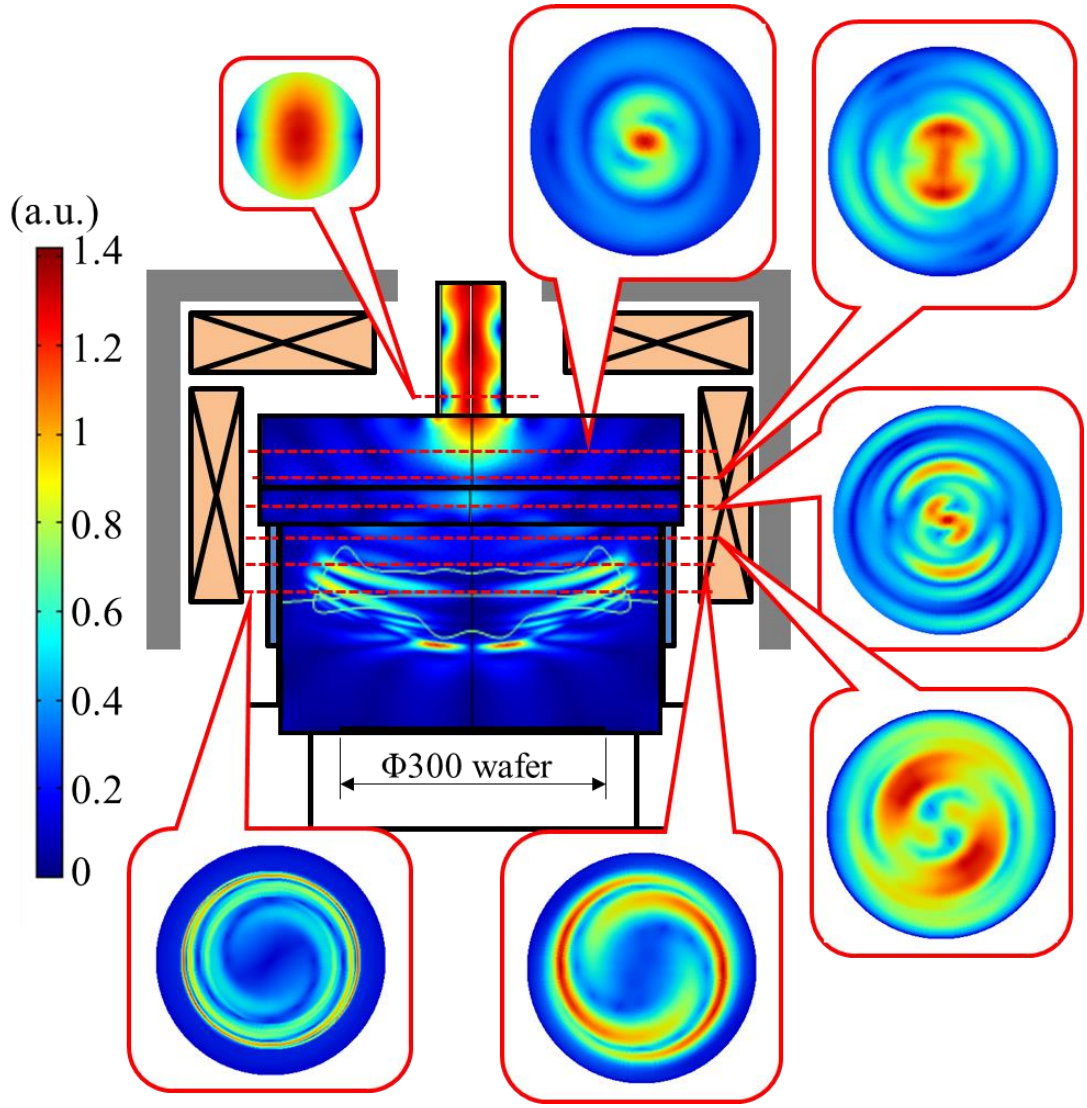

Fig. 4.3. Instantaneous electric field distribution in the (r, z) plane along with the (r, θ) plane as inset [1].

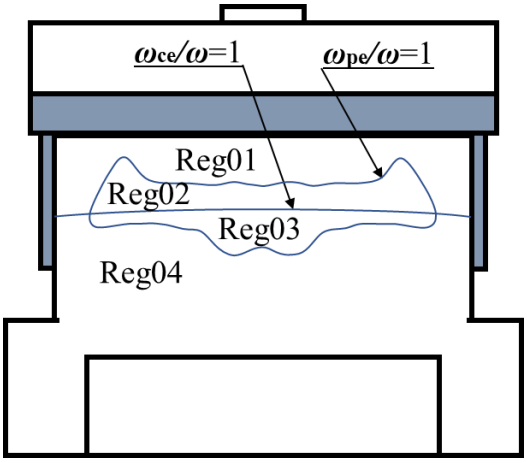

Fig. 4.4. Regions divided by the plasma density and the static magnetic field [1].

Reg01: the region of low-density and strong magnetic field where $\omega_{pe}/\omega < 1$ and $\omega_{ce}/\omega > 1$.

Reg02: the region of high-density and strong magnetic field where $\omega_{pe}/\omega > 1$ and $\omega_{ce}/\omega > 1$.

Reg03: the region of high-density and weak magnetic field where $\omega_{pe}/\omega > 1$ and $\omega_{ce}/\omega < 1$.

Reg04: the region of low-density and weak magnetic field where $\omega_{pe}/\omega < 1$ and $\omega_{ce}/\omega < 1$.

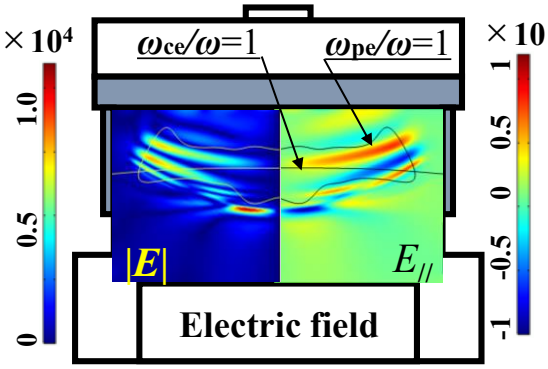

(a) Electric field of absolute value |***E***| and parallel component to the static magnetic field $E_{//}$ whose phase is 0 radian.

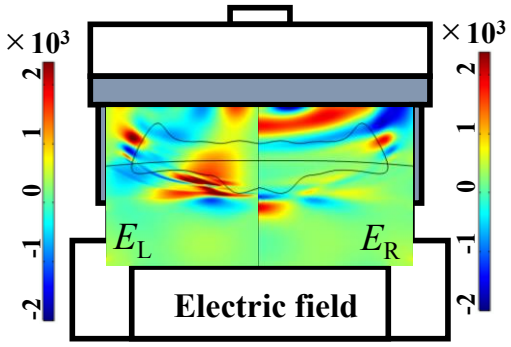

(b) Electric field of left-hand polarized component E_L and right-hand polarized wave E_R whose phase is 0 radian.

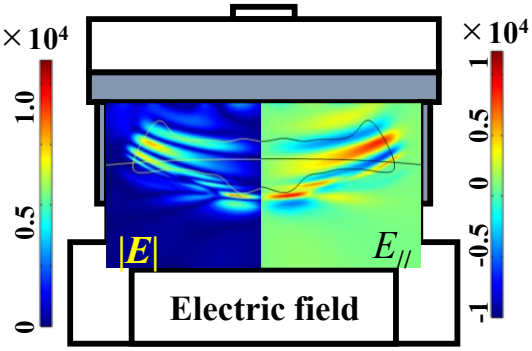

(c) Electric field of absolute value |***E***| and parallel component to the static magnetic field $E_{//}$ whose phase is π/2 radian.

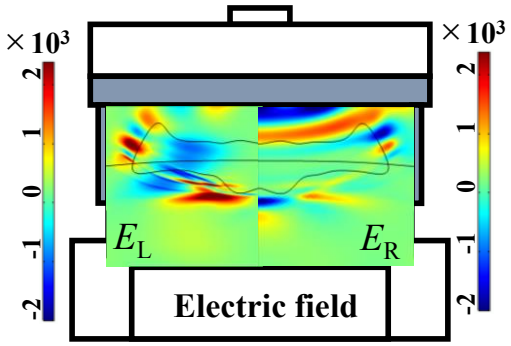

(d) Electric field of left-hand polarized component E_L and right-hand polarized wave E_R whose phase is π/2 radian.

Fig. 4.5. Instantaneous electric field distribution in the reactor by simulation [1].

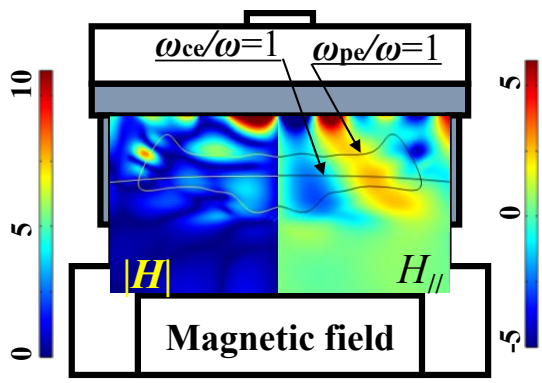

(a) Magnetic field of absolute value $|\boldsymbol{H}|$ and parallel component to the static magnetic field $H_{//}$ whose phase is 0 radian.

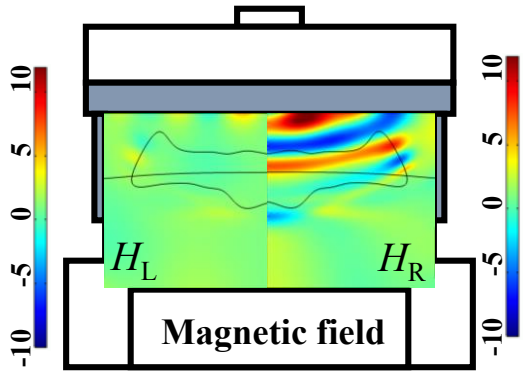

(b) Magnetic field of left-hand polarized component H_L and right-hand polarized wave H_R whose phase is 0 radian.

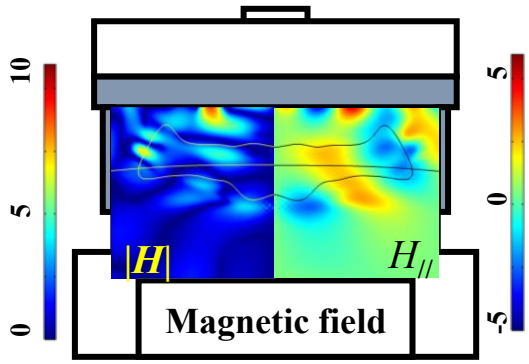

(c) Magnetic field of absolute value $|\boldsymbol{H}|$ and parallel component to the static magnetic field $H_{//}$ whose phase is $\pi/2$ radian.

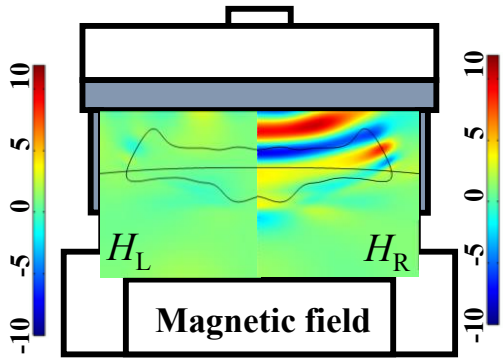

(d) Magnetic field of left-hand polarized component H_L and right-hand polarized wave H_R whose phase is $\pi/2$ radian.

Fig. 4.6. Instantaneous magnetic field distribution in the reactor by simulation [1].

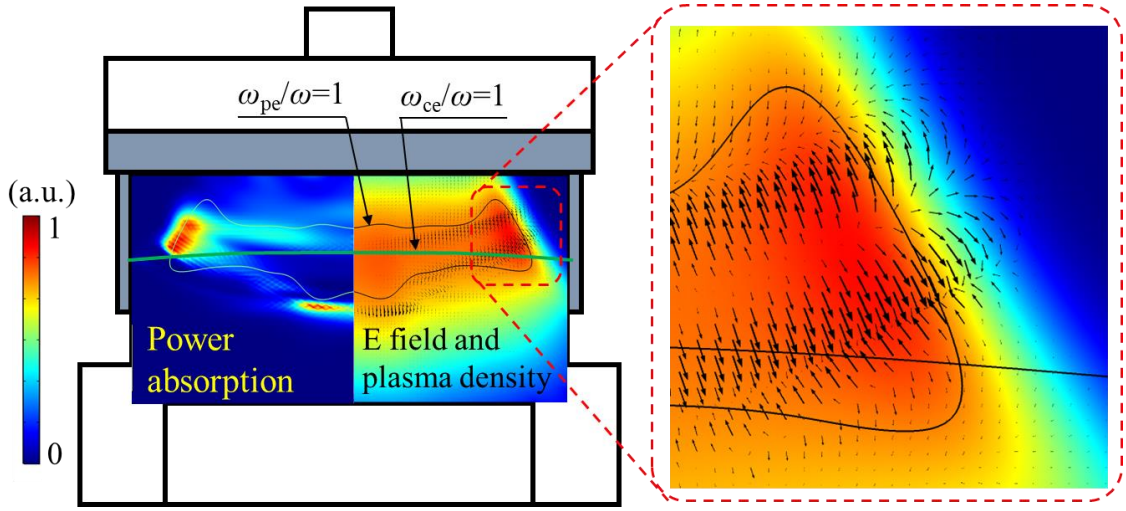

Fig. 4.7. Power absorption (left) and instantaneous electric field vector and plasma density (right) [1].

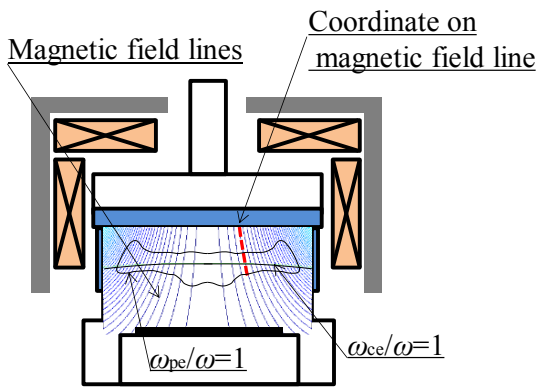

(a) Coordinate on magnetic field line.

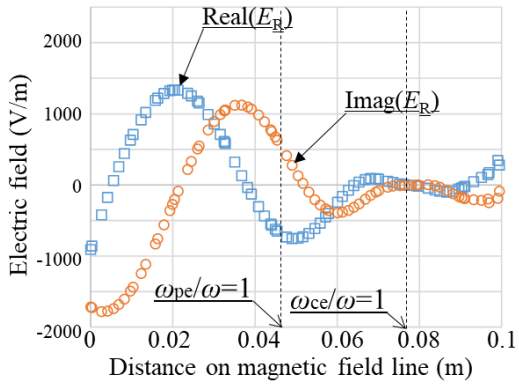

(b) Right-hand polarized component of electric field E_R on magnetic field line.

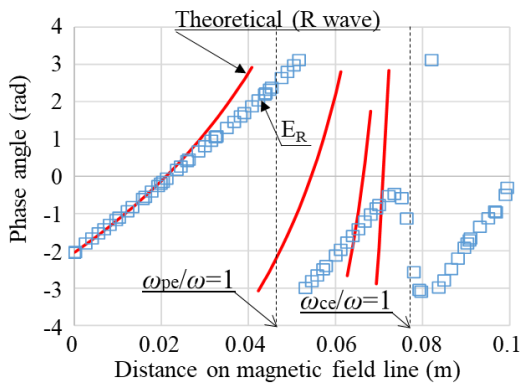

(c) Phase comparison right-hand polarized component of electric field E_R with theoretical R wave.

Fig. 4.8. Comparison right-hand polarized component of electric field E_R with theoretical R wave on magnetic field line [1].

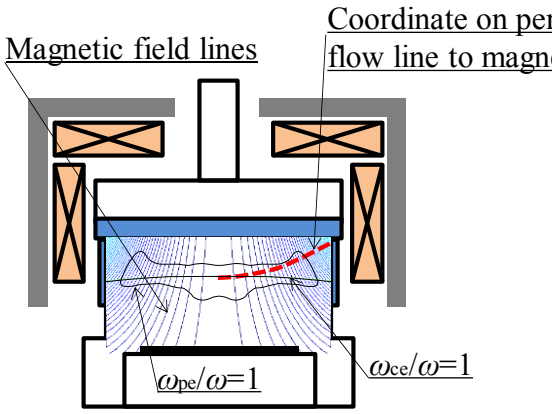

(a) Coordinate on perpendicular flow line to magnetic field.

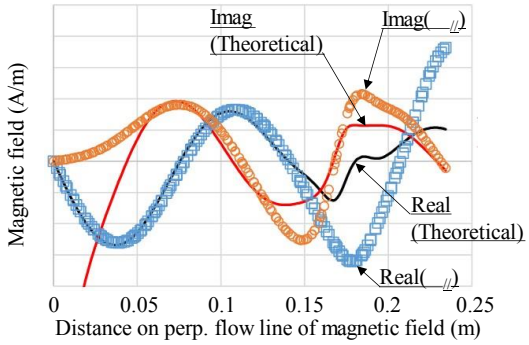

(b) Parallel component of magnetic field $H_{//}$ on perpendicular flow line to magnetic field.

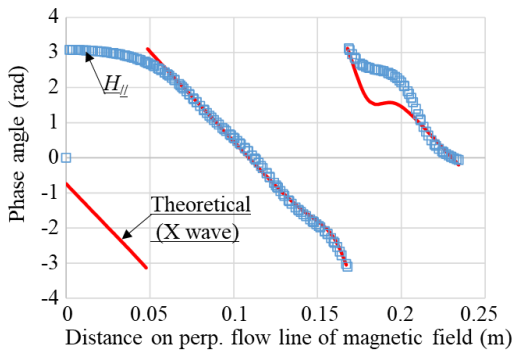

(c) Phase comparison parallel component of magnetic field $H_{//}$ with theoretical X wave.

Fig. 4.9. Comparison parallel component of magnetic field $H_{//}$ with theoretical X wave on perpendicular flow line to magnetic field [1].

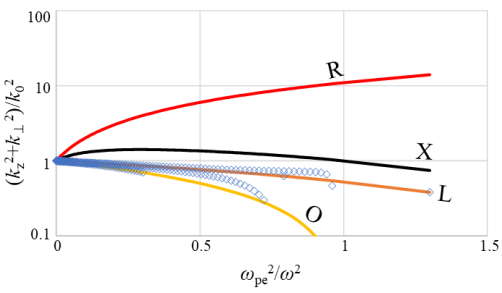

(a) j = 1, strong magnetic field region of ω_{ce}/ω = 1.1.

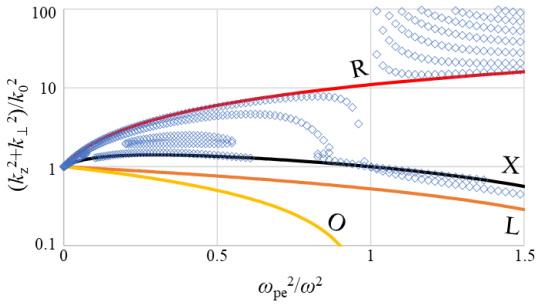

(b) j = 2, strong magnetic field region of ω_{ce}/ω = 1.1.

Fig. 4.10. Wavenumber dependence on plasma density [1].

Plasma radius a = 0.2 m, waveguide radius b = 0.25 m, phase dependence on azimuthal direction m = 1.

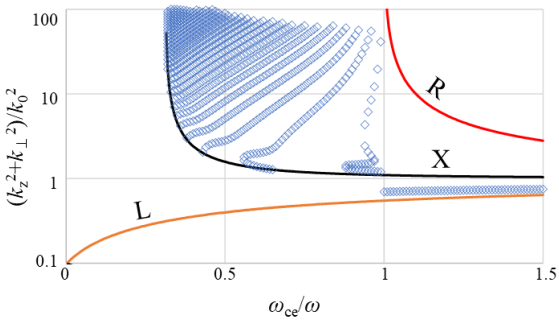

(a) j = 1, low density region of ω_{pe}/ω = 0.95.

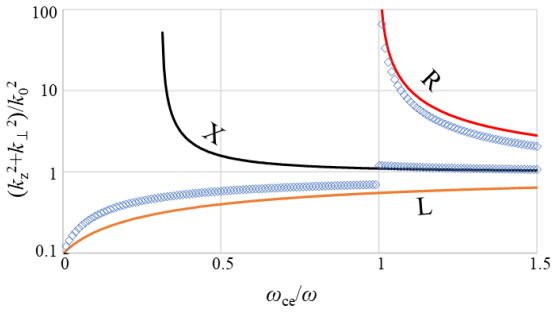

(b) j = 2, low density region of ω_{pe}/ω = 0.95.

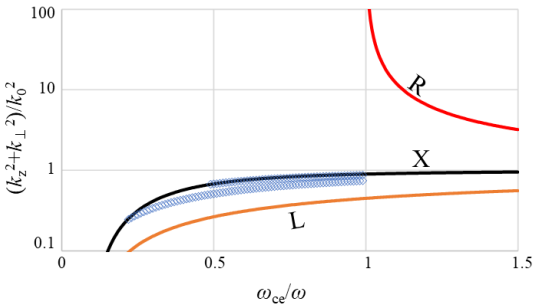

(c) j = 1, high density region of ω_{pe}/ω = 1.05.

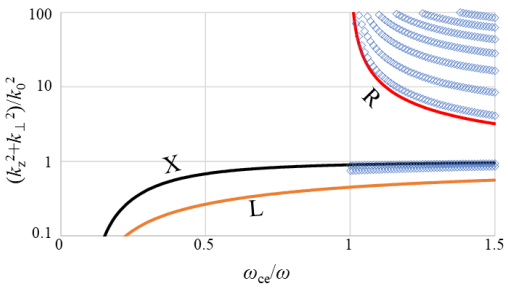

(d) j = 2, high density region of ω_{pe}/ω = 1.05.

Fig. 4.11. Wavenumber dependence on static magnetic field [1].

Plasma radius a = 0.2 m, waveguide radius b = 0.25 m, phase dependence on azimuthal direction m = 1.

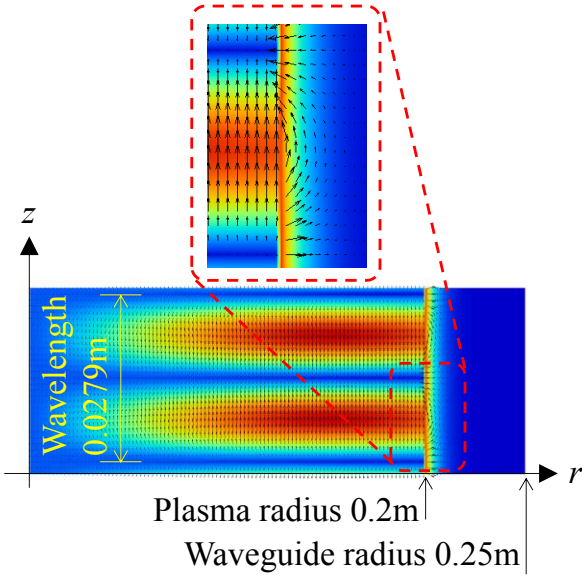

(a) Instantaneous electric field vector and magnitude.

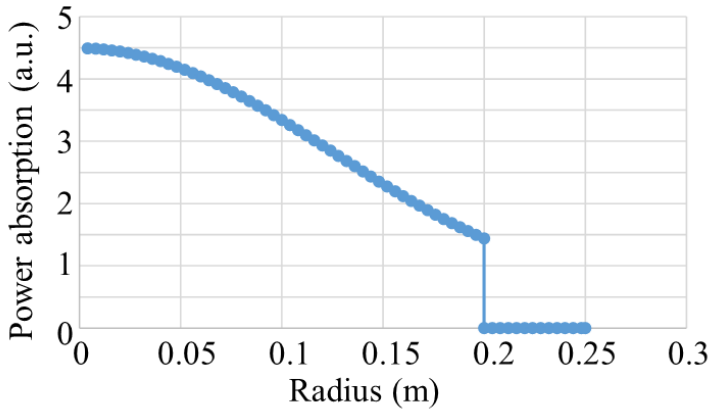

(b) Power absorption distribution.

Fig. 4.12. An example of electric field distribution and power absorption of plasma waveguide with outer vacuum layer [1].

Plasma radius a = 0.2 m, waveguide radius b = 0.25 m, phase dependence on azimuthal direction m = 1, ω_{pe}/ω = 1.02, ω_{ce}/ω = 1.1.

Chapter 5

5. Conclusions and Future Works

ECR plasma etchers have been used for decades in the semiconductor manufacturing industry [1]. One of the reasons is that the ECR plasma source can stably generate high density plasma at low pressure, which is useful to achieve high productivity and fine processing at the same time. Further, since the plasma is mainly generated at the ECR surface, which can be located away from the wall, wall damage due to the plasma can be reduced. In addition, it is verified that uniform plasma processing by uniform plasma generation can be achieved even on large-diameter wafers having a diameter of 300 mm, which is mainly used by the major semiconductor manufacturers. However, it was not clear from what mechanism uniform plasma can be generated by ECR plasma etchers. In the ECR plasma, it is known that the microwave electromagnetic field exhibits a complex behavior in addition to the microwave propagation, since various phenomena such as resonance and cutoff occur [2]. Also, as mentioned in Chapter 1, it is difficult to analyze the microwaves numerically because there is a problem that spurious solutions are mixed in when ordinary FEM is used. Due to these effects, there were few reports of microwave electromagnetic field analysis in ECR plasma etchers [3, 4], but recently, as countermeasures to the spurious problem in FEM analysis [5] gradually become popular, it has become possible to analyze.

In this thesis, following the introduction of Chapter 1, we investigated the microwave analysis of the ECR reactor in Chapter 2. As a result of the electromagnetic field analysis in the ECR reactor using the FEM, we obtained a very complex field distribution. At first, we investigated this complex pattern in detail since this pattern might

be spurious. However, it was confirmed that this pattern is not spurious and that it is generated by TG wave [6], which is a kind of static wave, because of the characteristic field patterns and the conditions that the pattern appears in. In addition, it was also confirmed that the calculation result of the tool we used is valid by comparing the result with the theoretical one. From the above results, we confirmed that the microwave analysis is valid, and TG waves whose distribution is very complicated are generated in the ECR reactor [7].

In Chapter 3, the plasma simulation of the ECR plasma etcher was performed by combining the microwave analysis, which is validated in Chapter 2, with plasma generation region analysis, and plasma diffusion analysis. The results of the simulation were compared with the experimental results of the plasma density distribution on the wafer, and the simulation was quantitatively verified. As a result, it was observed that a plasma column with a very uniform density distribution in the radial direction is formed on the wafer. Note, that a similar plasma column, that is uniform along radial direction, was experimentally observed in the ECR etcher for 450mm diameter wafers by plasma density measurement [8]. As a result of investigating the mechanism, by which a uniform plasma column is formed, we discovered the phenomenon, that the introduced R wave does not enter high density plasma of $\omega_{pe}/\omega > 1$ even in the strong magnetic region of $\omega_{ce}/\omega > 1$. Because of the phenomenon, plasma density saturates at density of $\omega_{pe}/\omega = 1$ and very uniform plasma is generated. Moreover, the plasma generation region becomes ring-shaped, because microwave power does not enter the inner region and is absorbed in the outer region. It is possible that uniform plasma near the wafer might be realized using this uniform plasma, by optimizing the configuration of the reactor or the distribution of the static magnetic field, such as reactor height, which corresponds to the distance from

the quartz plate to the wafer, or ECR position, which corresponds to the distance from ECR surface to the wafer.

However, this phenomenon of R wave propagation in the ECR reactor contradicts the ordinary characteristics of R waves described as the magnetic beach concept (see Sec. 1.3). Generally, in free space without boundary, an R wave does not have a cutoff and propagates in high density plasma of $\omega_{pe}/\omega > 1$ in the strong magnetic field of $\omega_{ce}/\omega > 1$. To clarify this seeming contradiction, we theoretically analyzed microwaves in a plasma waveguide with an axial static magnetic field, while considering reactor walls. As a result, we found that the propagation characteristics in the plasma waveguide are modified in the vicinity of the plasma density of $\omega_{pe}/\omega = 1$, compared to an R wave without boundary. In other words, we found that the phenomenon occurs due to the boundary effect [9].

In Chapter 4, we investigated microwave electromagnetic field and propagation in the ECR reactor in detail. We divided the electromagnetic field in the ECR reactor into the component parallel to the static magnetic field, a right-hand polarized component, and a left-hand polarized component. We compared each component with the fundamental electromagnetic R, L, X, O, and TG waves, and identified X and TG waves in the ECR reactor, besides the introduced R wave. In addition, a surface wave located at the interface of the plasma and the quartz window was also observed. Moreover, we performed theoretical analysis of the plasma waveguide with an outer vacuum layer, which simulates the plasma column on the wafer in the ECR reactor. From this, propagation characteristics were derived by considering the plasma distribution and the effect of the reactor wall. As a result of the theoretical analysis, it was found that the R wave transforms into the X wave and the TG wave at around a plasma density corresponding to $\omega_{pe}/\omega = 1$ in the

strong magnetic field region of $\omega_{ce}/\omega > 1$. We found that this is the key reason, due to which the introduced R waves do not enter the high-density region of $\omega_{pe}/\omega > 1$, and due to which a uniform plasma column along radial direction is generated [10].

As a result of the phenomenon, that the microwave does not enter the high-density region of $\omega_{pe}/\omega > 1$ and it is strongly absorbed at the ECR region of $\omega_{ce}/\omega = 1$, the microwave absorption is strong in the vicinity of the cross point where $\omega_{pe}/\omega = 1$ and $\omega_{ce}/\omega = 1$. This results in a ring-shaped power absorption.

If plasma is uniformly generated in the reactor, the plasma distribution tends to become convex, with a higher density in the center because of the diffusion loss at the reactor wall. Namely, plasma loss near the wall is large compared with the center region. To generate a uniform plasma, ring-shaped plasma generation is essential to compensate the loss at the reactor wall. This ring-shaped plasma generation is realized by ring-shaped power absorption in the vicinity of the region of $\omega_{pe}/\omega > 1$ in the ECR reactor. By using this plasma generation, we believe plasma uniformity near the wafer can be improved.

We investigated and clarified the mechanism of uniform plasma generation in the ECR etcher as stated above. The key phenomenon that the R waves do not enter high density plasma of $\omega_{pe}/\omega > 1$ is important in the mechanism of uniform plasma generation and it seems that this phenomenon in the ECR reactor has been reported for the first time. In early works regarding ECR plasma sources, described in Chapter 1, it seems that the reasons why the phenomenon was not reported are lack of microwave analysis technology preventing spurious solutions or insufficient computational power. Based on our new understanding of this mechanism, we can control the microwave power deposition profile, leading to the improvement of the uniformity in the ECR reactor. Considering each step of the mechanism, we believe hardware improvement can be realized.

The analysis of propagation characteristics considering the wall or boundary effect in the strong magnetic field region of $\omega_{ce}/\omega > 1$ could be clarified to some extent in this thesis, but the analysis of propagation characteristics in the weak magnetic field region of $\omega_{ce}/\omega < 1$ is still insufficient, and it is a problem to be addressed in the future. It is expected that the same procedure used in the strong magnetic field region is useful to understand the propagation characteristics in weak magnetic field. We mainly analyzed the ECR reactor by using simulation technique and theoretical analysis, however, measurement of microwave distribution is also necessary, including high resolution measurement in bulk plasma that can recognize fine electric field patterns of TG waves.

In a plasma etching process, various reactive gases such as chlorine, hydrogen bromide, sulfur hexafluoride are used. They generate negative ions, and therefore the plasma composition is complicated. We used argon in simulation, which hardly generates the negative ions. However, to investigate chemical effects of plasma etching process, plasma analysis containing these reactive gases is essential. In addition, we used a simplified simulation, which does not consider the plasma sheath. Plasma analysis considering these effects are also necessary in the future works.

By applying the knowledge that we obtained from this work, we believe that we can improve the controllability of ECR plasma, and realize more flexible, highly productive plasma processing tools. To realize the improved tools, hardware modifications are needed, that consider the propagation and absorption characteristics of microwaves, such as the microwave introducing method, or the solenoid coil configuration for the static magnetic field. The simulation tool we developed is useful to identify the effectiveness of hardware modifications. By using this simulation tool, and by considering the mechanism of uniform plasma generation and microwave propagation

in the ECR reactor, we believe that hardware improvement of ECR etching tools for next generation ULSIs can be achieved.

References

[1] H. Enami, Y. Ogawa, M. Izawa, and T. Saito, "History and future of Hitachi's plasma etching system," Hitachi Rev., vol. 60, no. 5, pp. 198- 202, Aug. 2011.

[2] F. F. Chen, Introduction to Plasma physics. New York, NY, USA: Plenum Press, 1974.

[3] Y. Yasaka, A. Fukuyama, A. Hatta, and R. Itatani, "Two–dimensional modeling of electron cyclotron resonance plasma production," J. Appl. Phys., vol. 72, no. 7, pp. 2652–2658, 1992.

[4] R. L. Kinder and M. J. Kushner, "Consequences of mode structure on plasma properties in electron cyclotron resonance sources," J. Vac. Sci. Technol. A, Vac. Surf. Films, vol. 17, no. 5, pp. 2421-2430, 1999.

[5] Z. J. Cendes, "Vector finite elements for electromagnetic field computation," IEEE Trans. Magn., vol. 27, no. 5, pp. 3958–3966, 1991.

[6] A. W. Trivelpiece and R. W. Gould, "Space charge waves in cylindrical plasma columns," J. Appl. Phys., vol. 30, no. 11, pp. 1784-1793, 1959.

[7] **H. Tamura**, T. Tetsuka, N. Tamari, D. Kuwahara, and S. Shinohara, "Numerical identification of Trivelpiece–Gould waves in an electron cyclotron resonance etching reactor," IEEE Trans. Plasma Sci., vol. 46, no. 10, pp. 3662–3668, 2018.

[8] K. Maeda, S. Obama, **H. Tamura**, G. Miya, and M. Izawa, "Study on the distribution control of etching rate and critical dimensions in microwave electron cyclotron resonance plasmas for the next generation 450 mm wafer processing," Jpn. J. Appl. Phys., vol. 51, no. 8S1, p. 08HD01, 2012.

[9] **H. Tamura**, T. Tetsuka, D. Kuwahara, S. Shinohara, “Study on uniform plasma generation mechanism of electron cyclotron resonance etching reactor,” IEEE Trans. Plasma Sci., vol. 48, no. 10, pp. 3606-3615, 2020.

[10] **H. Tamura**, T. Tetsuka, T. Sekine, and S. Shinohara, “Boundary effect on mode transformation in an electron cyclotron resonance etching reactor,” Jpn. J. Appl. Phys., accepted.

Appendix

In section 4.2.3, an analytical model of plasma waveguides with outer vacuum layer is described for the outer region of the TM mode. Here, the mode whose outer region is the TE mode is described. In the outer vacuum layer ($a < r < b$), electromagnetic field of the TE mode for $k_{\perp\mathrm{out}}^2 > 0$ is

$$\begin{cases} E_z = 0 \\ E_r = -\frac{\omega}{k_{\perp out}{}^2}\frac{m}{r}\{A_{1B}J_m(k_{\perp out}r) + A_{2B}N_m(k_{\perp out}r)\} \\ E_\varphi = -\frac{i\omega}{k_{\perp out}}\{A_{1B}J_m{}'(k_{\perp out}r) + A_{2B}N_m{}'(k_{\perp out}r)\} \\ B_z = A_{1B}J_m(k_{\perp out}r) + A_{2B}N_m(k_{\perp out}r) \\ B_r = \frac{ik_z}{k_{\perp out}}\{A_{1B}J_m{}'(k_{\perp out}r) + A_{2B}N_m{}'(k_{\perp out}r)\} \\ B_\varphi = -\frac{k_z}{k_{\perp out}{}^2}\frac{m}{r}\{A_{1B}J_m(k_{\perp out}r) + A_{2B}N_m(k_{\perp out}r)\} \end{cases}, \tag{A.1}$$

and for $k_{\perp\mathrm{out}}^2 < 0$ is

$$\begin{cases} E_z = 0 \\ E_r = -\frac{\omega}{k_{\perp out}{}^2}\frac{m}{r}\{A_{1B}I_m(k_{\perp out}r) + A_{2B}K_m(k_{\perp out}r)\} \\ E_\varphi = -\frac{i\omega}{k_{\perp out}}\{A_{1B}I_m{}'(k_{\perp out}r) + A_{2B}K_m{}'(k_{\perp out}r)\} \\ B_z = A_{1B}I_m(k_{\perp out}r) + A_{2B}K_m(k_{\perp out}r) \\ B_r = \frac{ik_z}{k_{\perp out}}\left\{A_{1B}I_m^{\prime(k_{\perp out}r)} + A_{2B}K^{\prime(k_{\perp out}r)}\right\} \\ B_\varphi = -\frac{k_z}{k_{\perp out}{}^2}\frac{m}{r}\{A_{1B}I_m(k_{\perp out}r) + A_{2B}K_m(k_{\perp out}r)\} \end{cases}. \tag{A.2}$$

The boundary condition for $k_{\perp\mathrm{out}}^2 > 0$ is

$$\begin{cases} J_m\left(k_{\perp j}a\right) = 0 \\ A_{2B} = A_{m1}k_{\perp out}\dfrac{\frac{m}{ai\kappa_2}\delta_1\frac{J_m\left(k_{\perp j}a\right)}{{k_{\perp j}}^2}+\frac{J_{m'}\left(k_{\perp j}a\right)}{k_{\perp j}}}{-\frac{N_{m'}(k_{\perp out}b)}{J'_m(k_{\perp out}b)}J_{m'}(k_{\perp out}a)+N_{m'}(k_{\perp out}a)}, \\ A_{1B} = -A_{2B}\dfrac{N_{m'}(k_{\perp out}b)}{J'_m(k_{\perp out}b)} \end{cases} \quad j = 1, 2, \tag{A.3}$$

and for $k_{\perp\mathrm{out}}^2 < 0$ is

$$\begin{cases} J_m\left(k_{\perp j}a\right) = 0 \\ A_{2B} = iA_{m1}k_{\perp out}\dfrac{\frac{m}{ai\kappa_2}\delta_1\frac{J_m\left(k_{\perp j}a\right)}{{k_{\perp j}}^2}+\frac{J_{m'}\left(k_{\perp j}a\right)}{k_{\perp j}}}{-\frac{K_{m'}\left(\frac{k_{\perp out}}{i}b\right)}{I'_m\left(\frac{k_{\perp out}}{i}b\right)}I_{m'}\left(\frac{k_{\perp out}}{i}a\right)+K_{m'}\left(\frac{k_{\perp out}}{i}a\right)}, \\ A_{1B} = -A_{2B}\dfrac{K_{m'}\left(\frac{k_{\perp out}}{i}b\right)}{I'_m\left(\frac{k_{\perp out}}{i}b\right)} \end{cases} \quad j = 1, 2. \tag{A.4}$$

By using Eqs. (A.3) and (A.4) together with (4.2) and (4.5), the wavenumber along z axis k_z can be solved, and propagation characteristics can be derived.